Clouds: How different are they when observed in MODIS and CloudSat-CALIPSO?

Principal Investigator: Tao Wang (329)

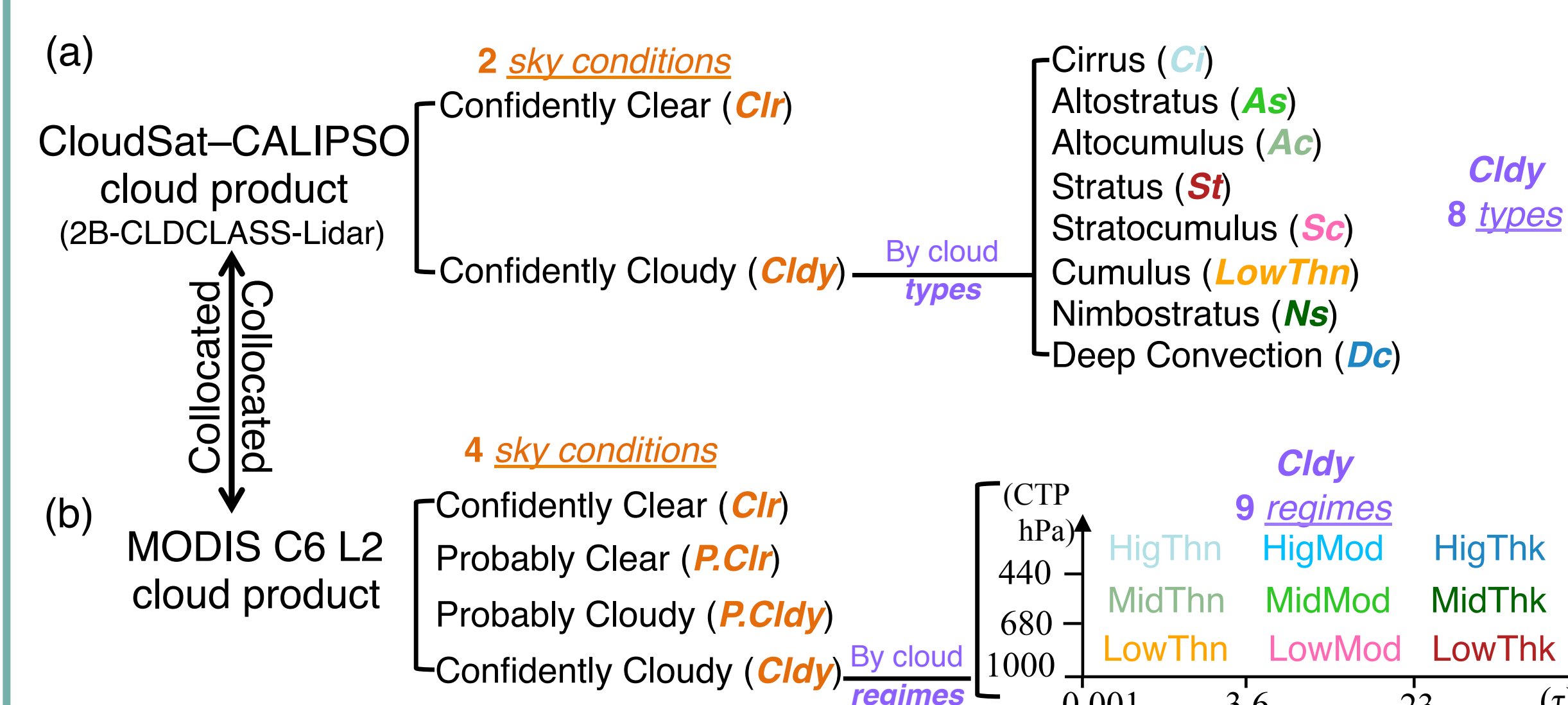Co-Is: Eric J. Fetzer, Sun Wong, Brian H. Kahn, and Qing Yue (329)

1. Objective

Investigate how clouds are observed differently in MODIS (passive instrument) and CloudSat–CALIPSO (active radar–lidar instrument).
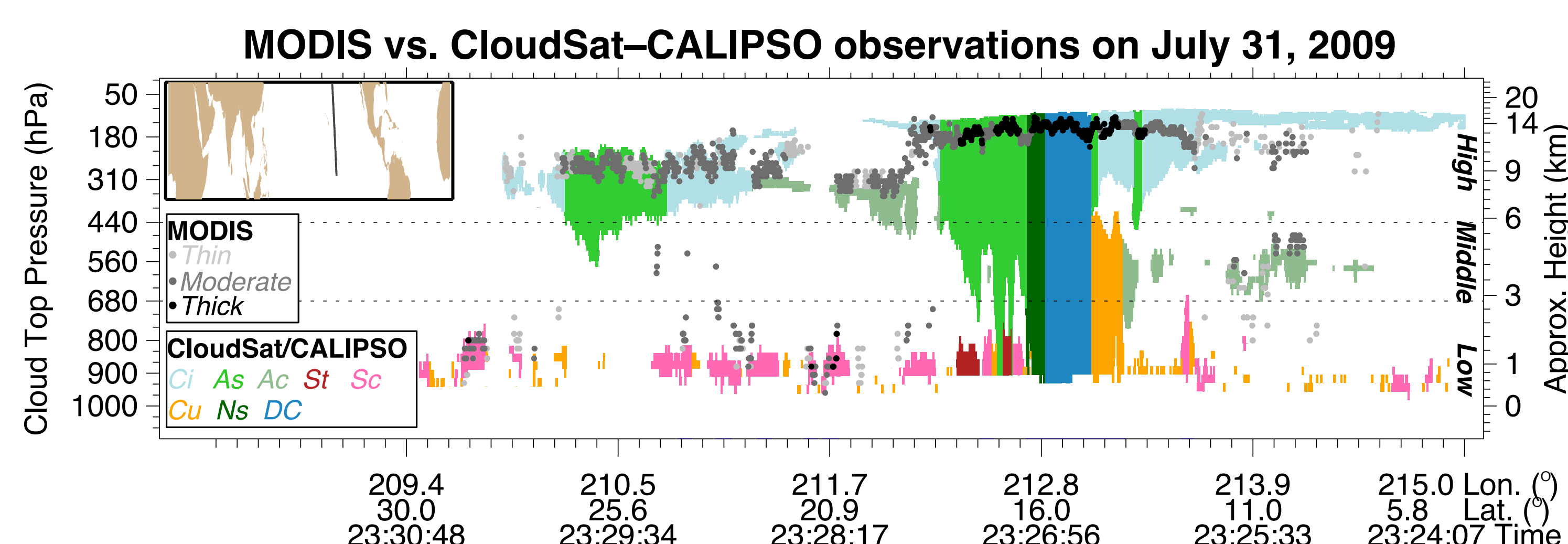
2. Data & Method

- MODIS L2 Collection 6 daytime cloud mask, cloud top pressure (CTP) and cloud optical depth (τ)
- CloudSat-CALIPSO cloud classification product (2B-CLDCLASS-LIDAR)
- For period of **2008-2010**, **>267** million **collocated** pixels

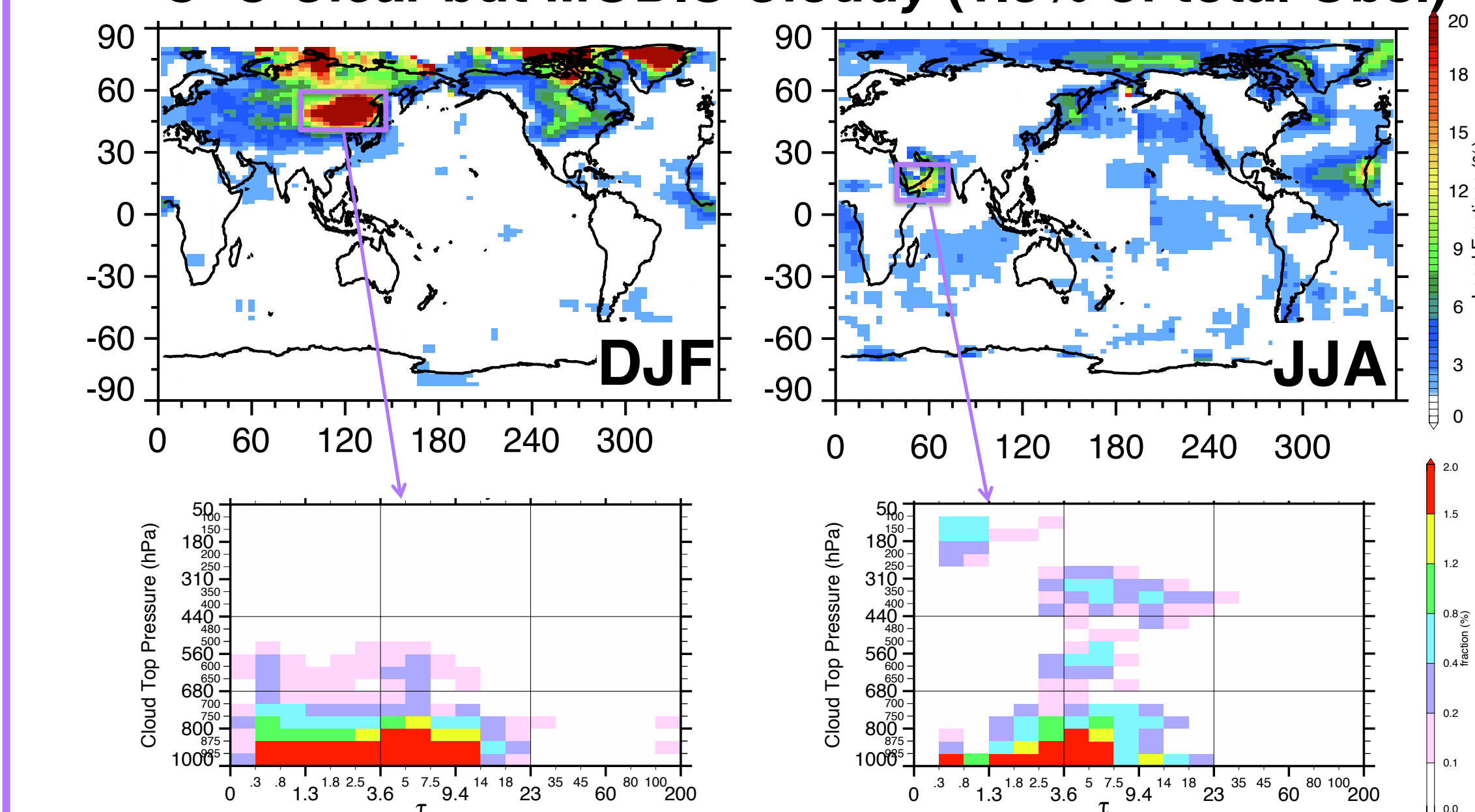**Cloud-Related Structures in CloudSat–CALIPSO and MODIS Product**

(a) CloudSat–CALIPSO cloud product (2B-CLDCLASS-Lidar)

2 *sky conditions*
- Confidently Clear (*Clr*)
- Confidently Cloudy (*Cldy*) — By cloud types

Cldy **8** *types*
- Cirrus (*Ci*)
- Altostratus (*As*)
- Altocumulus (*Ac*)
- Stratus (*St*)
- Stratocumulus (*Sc*)
- Cumulus (*LowThn*)
- Nimbostratus (*Ns*)
- Deep Convection (*Dc*)

Collocated

(b) MODIS C6 L2 cloud product

4 *sky conditions*
- Confidently Clear (*Clr*)
- Probably Clear (*P.Clr*)
- Probably Cloudy (*P.Cldy*)
- Confidently Cloudy (*Cldy*) — By cloud regimes

Cldy **9** *regimes*

(CTP hPa)			
440	HigThn	HigMod	HigThk
680	MidThn	MidMod	MidThk
1000	LowThn	LowMod	LowThk
	0.001	3.6	23 (τ)

3. Results: overview

MODIS vs. CloudSat–CALIPSO observations on July 31, 2009

MODIS: Thin / Moderate / Thick
CloudSat/CALIPSO: Ci As Ac St Sc / Cu Ns DC

Global frequencies of clear/cloudy conditions in MODIS and CloudSat–CALIPSO (2007-2010)

C–C \ MODIS	Clr	P.Clr	P.Cldy	Cldy
Clr	**20.9%**	3.5%	0.9%	*1.8%*
Cldy	*9.1%*	3.6%	3.3%	**56.9%**

4. Disagreement: *Clear/Cloudy* Conditions

C–C *Clear* but MODIS *Cloudy* (1.8% of total Obs.)

DJF / JJA

C–C *Cloudy* but MODIS *Clear* (9.1% of total Obs.)

MAM / SON

CloudSat–CALIPSO Cloud Types
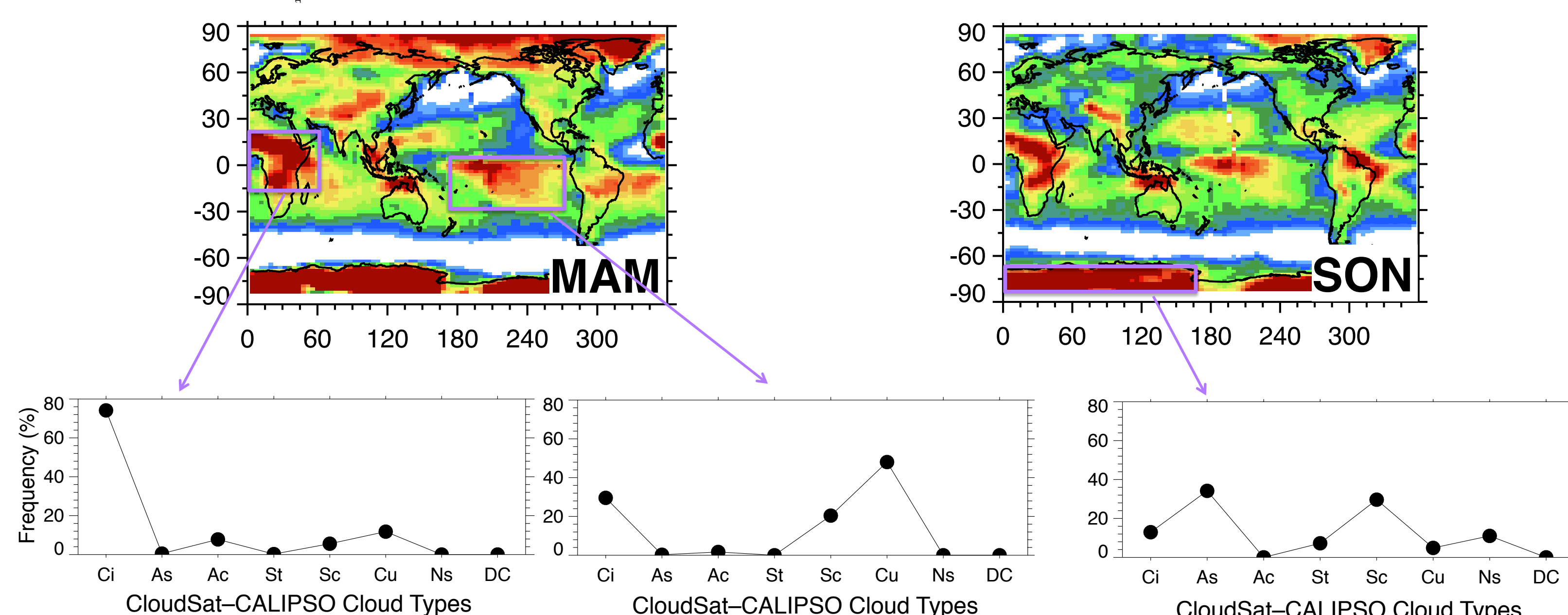
5. Cross-Reference in Cloud Classifications

a) Tropics (30° N–S)

b) Mid-Latitudes (30-60° N–S)

HghThn HghMod HghThk
MidThn MidMod MidThk
LowThn LowMod LowThk
Cldy-NaN

CloudSat–CALIPSO Cloud Types
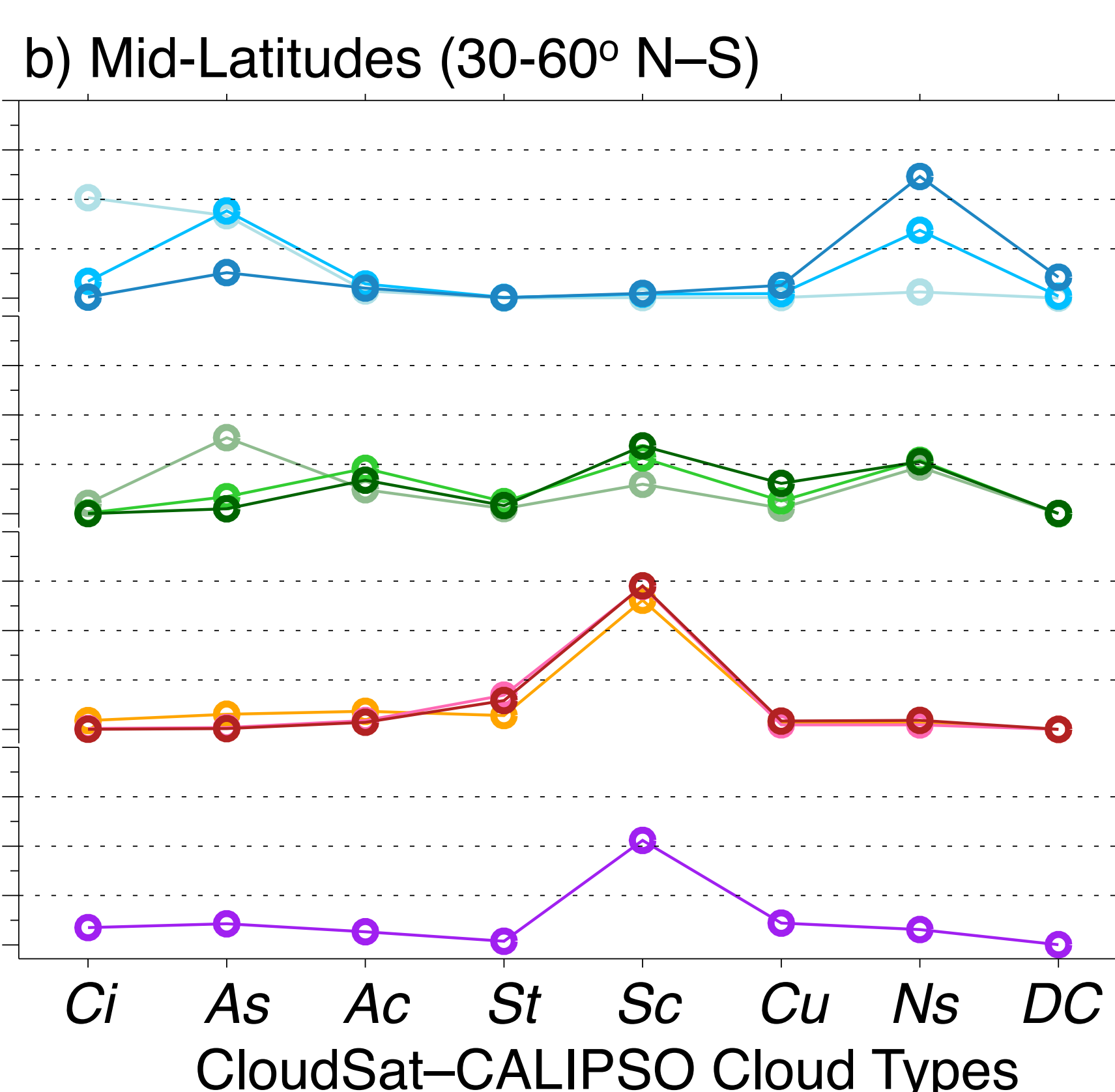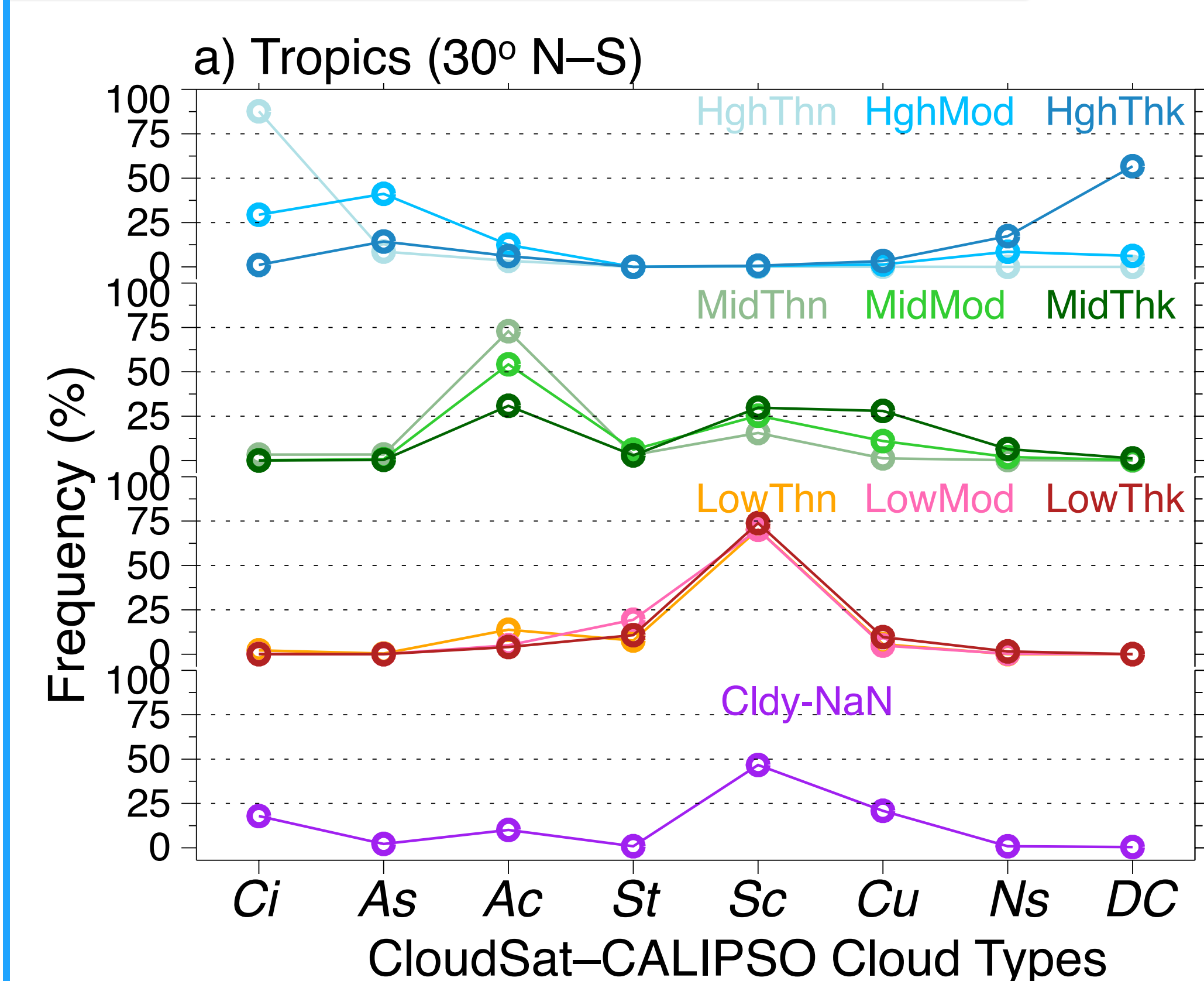
6. Conclusions

- Agreement between MODIS and C–C cloud detection is 77.8%, with 20.9% showing both *Clear* and 56.9% showing both *Cloudy*

- 9.1% of observations are *Clear* in MODIS but *Cloudy* in C-C, indicating clouds missed by MODIS; 1.8% of observations are *Cloudy* in MODIS but *Clear* in C–C, likely due to aerosol/dust or surface snow layers misidentified by MODIS.

- For single-layer clouds, ~70% of MODIS low-level (CTP>680 hPa) clouds are classified as stratocumulus (*Sc*) in C–C, regardless of optical thickness.

Poster No. EB-1

Partial data coverage and changes in surface heat fluxes bias our estimates of climate change

Author: Mark Richardson (329J)

Graeme Stephens (3292)

- We show for first time: climate models and observation-based calculations agree on near-term warming after accounting for data-sparse regions and mix of air and water data.

- Air should warm more than water due to changes in surface energy balance. Next work is how this affects precipitation to guide JPL exploitation of missions like Cloudsat, GPM, TRMM.

Air vs. water warming

- Water temperature is measured over oceans, and sea ice retreat means more water data. We take water temperatures from models to match rather than the typical approach of using global air output.
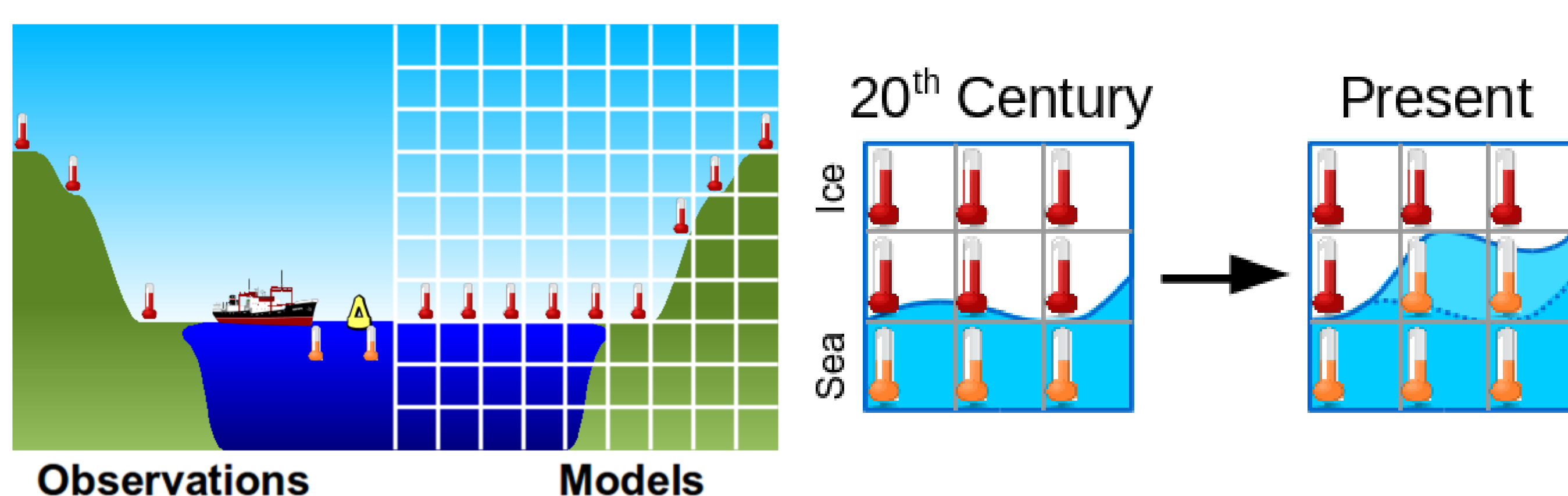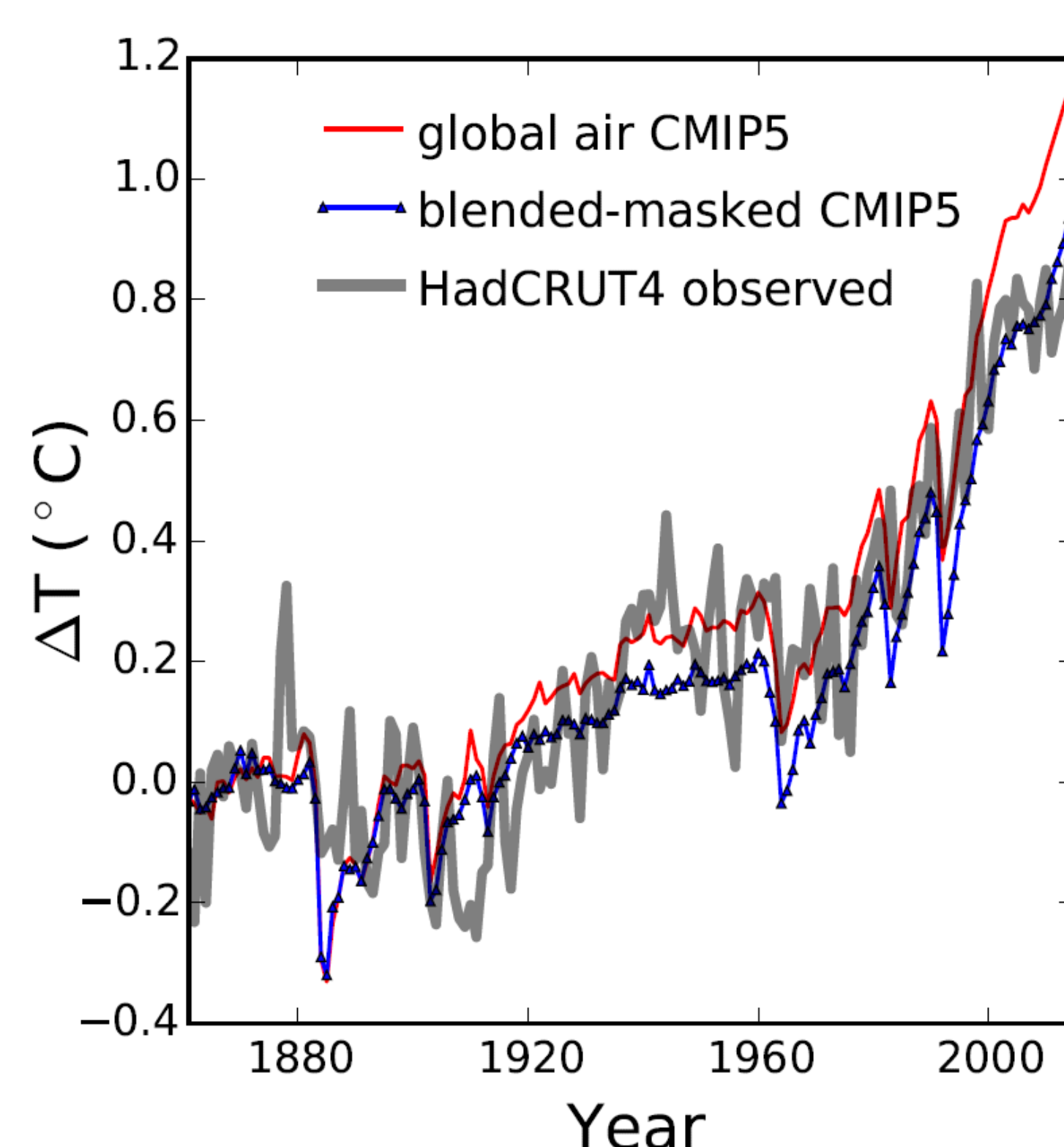

Air warms more than water

Air warms more **because of changing heat flows and not because water has a higher heat capacity**, instead:

1. Stronger greenhouse effect warms air more than the surface

2. More water vapour absorbs more sunlight before it reaches the ground

3. Smaller air-water temperature difference reduces upward flow of air, but it contains more vapour and evaporative cooling dominates.

Modelled versus observed temperatures

- **84 climate-model-median global air ΔT (red)**
- **Climate model ΔT in same way as observations (blue)**
- **Observations (grey)**

- **Modelled global air ΔT over 1861—2009 is 24% more than when model data is matched to observations. 9% from air-water mix, 15% from missing regions.**
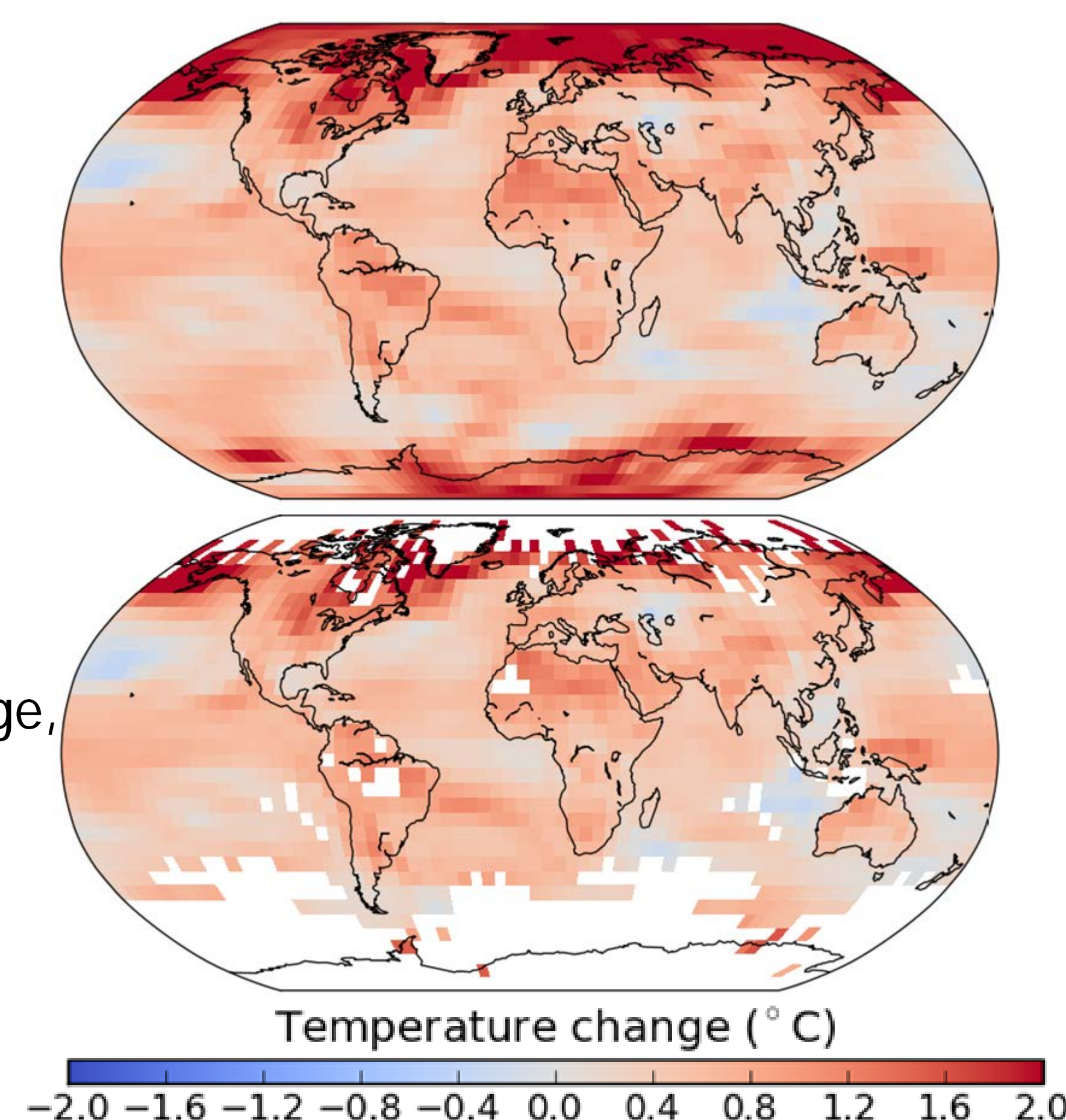
Global vs. non-global warming

$T_{1996-2005} - T_{1861-1870}$ in CSIRO Mk-3-6-0 climate model

Global coverage, reported ΔT:
0.66 °C

1996—2005 coverage, reported ΔT:
0.59°C

Missing data hides warming

Temperature change (°C)

Heat flows control precipitation changes

- **Next step is to relate heat fluxes and precipitation**, using fair model-observation comparisons
- Condensing vapour heats air, other heat flows must change to allow continued moisture flow upward
- Model responses of precipitation to CO_2-caused warming are below.

Poster No. EB-2
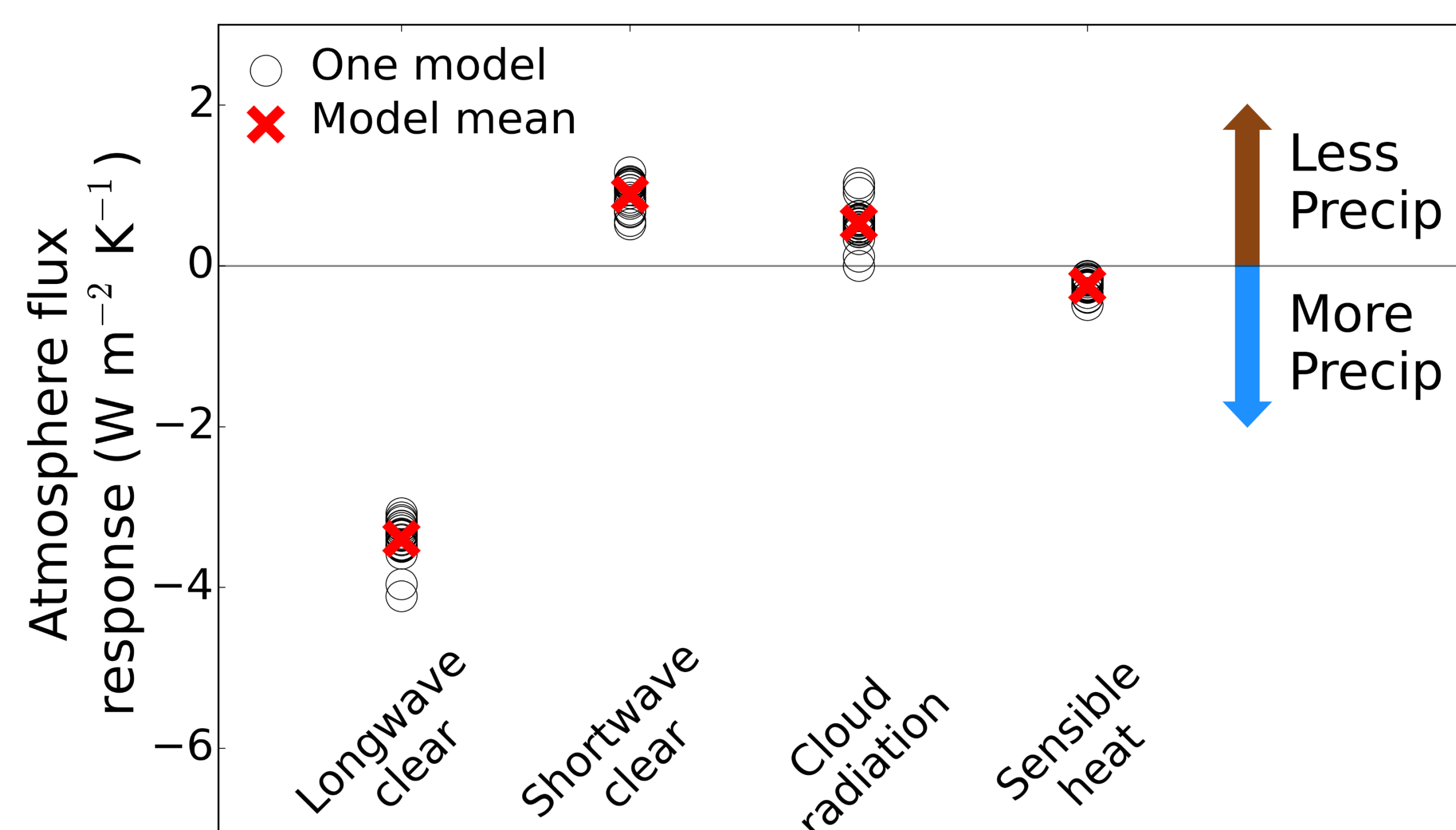
Improvements to the CloudSat–MODIS Cloud Liquid Water Retrieval Algorithm

Author: Jussi Leinonen (329J)
Matthew D. Lebsock (329J), Graeme L. Stephens (3292)

Background and motivation

- Clouds are important modulators of the Earth climate system and a significant uncertainty in climate models.
- Unlike passive sensors, CloudSat can provide a 3D view of cloud structure, better constraining climate model physics models.
- Cloud water content is a fundamental cloud property and a required quantity for many CloudSat data products.
- The CloudSat cloud liquid water product has been shown to be inconsistent with AMSR-E and microwave attenuation-based products.
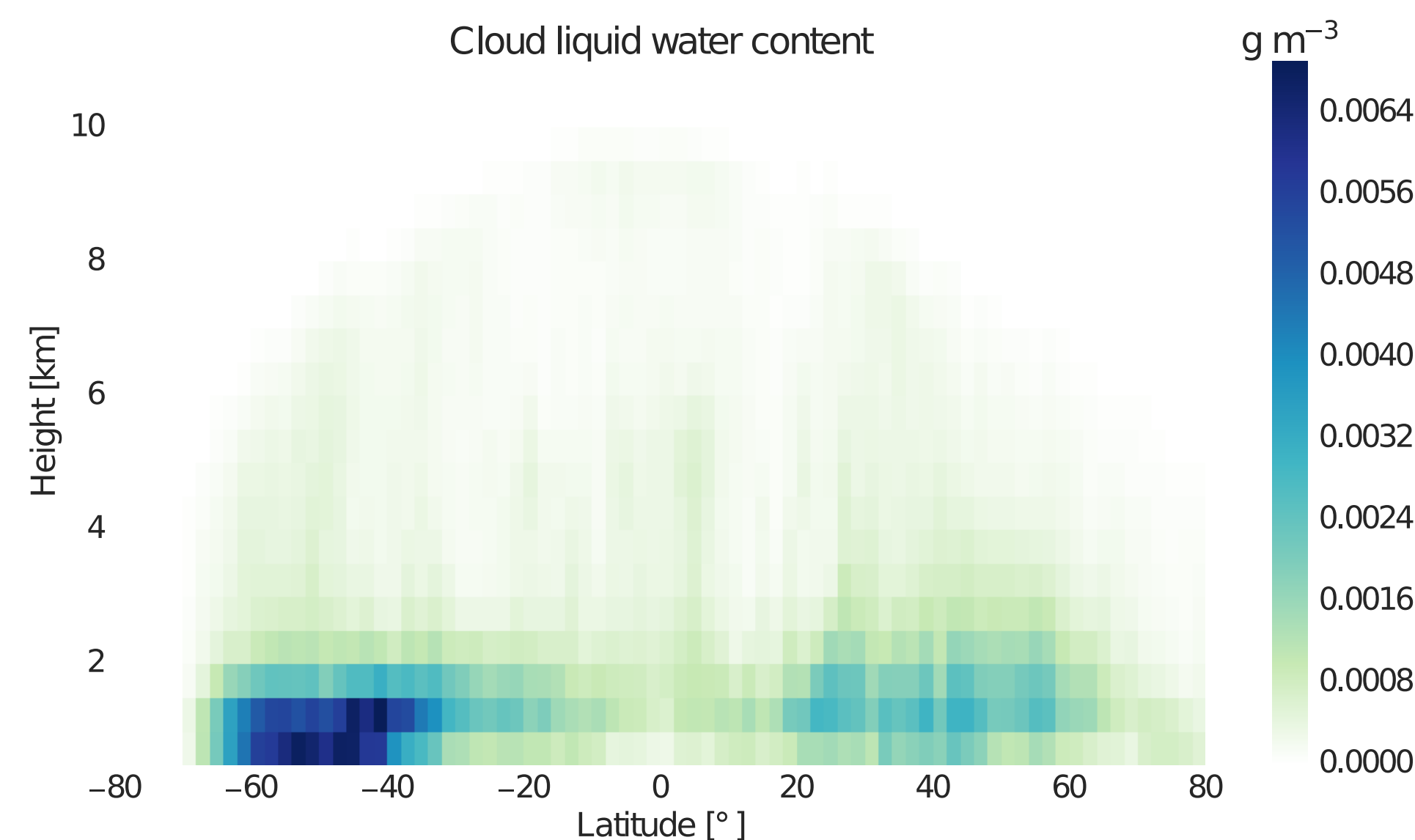

Global average cloud liquid water content (April 2007) by latitude and height, as given by the new algorithm.

Summary

- We improved the CloudSat–MODIS combined cloud liquid water retrieval algorithm.
- A comparison of modeled and measured radar signal attenuation shows that the algorithm gives the correct amount of cloud water, on average.
- The new algorithm reduces the number of free variables and makes the algorithm less dependent on prior assumptions.
- Ongoing development is focused on making the algorithm usable when precipitation, ice clouds or mixed-phase clouds are present.

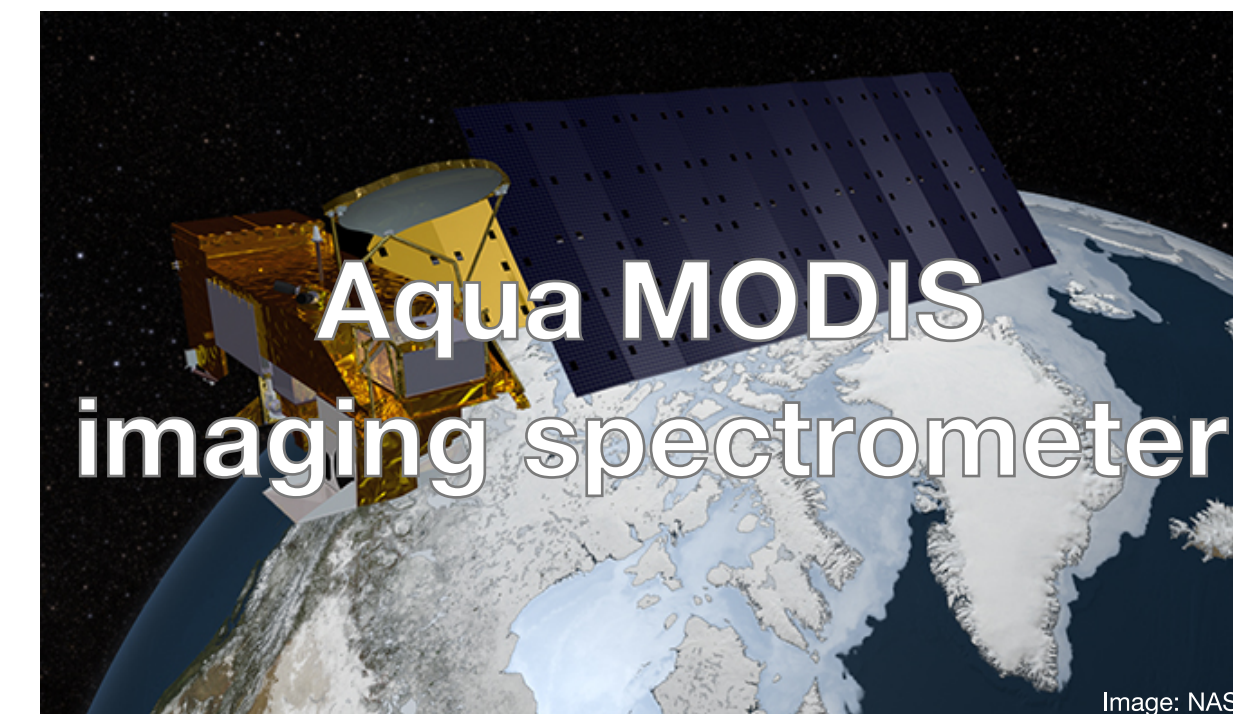## Strategy: combine the strengths of different measurements
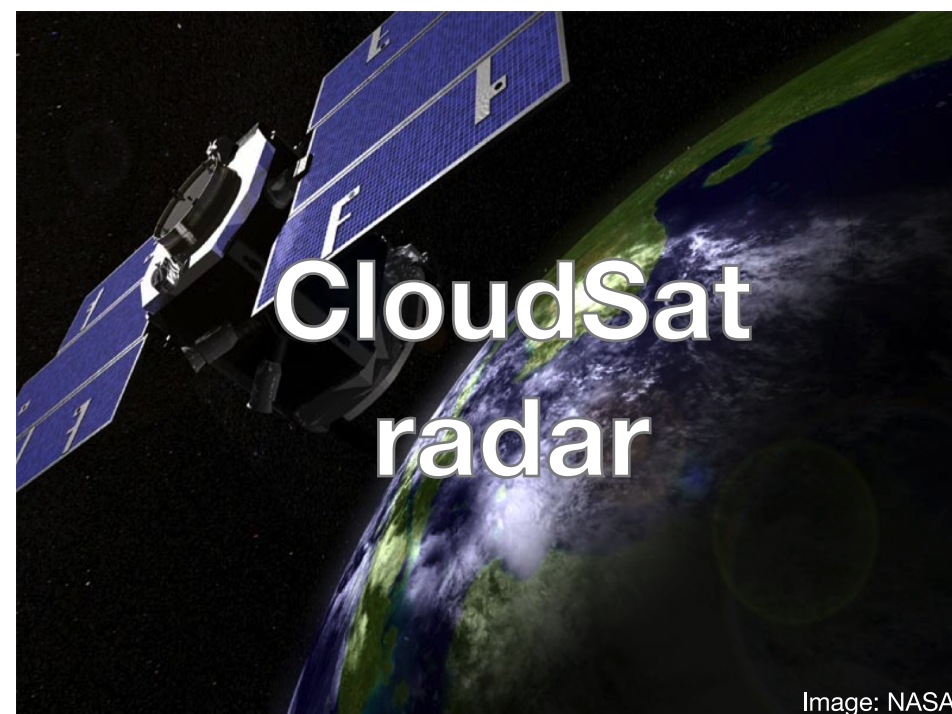
Radar reflectivity

+ Range resolved
+ Very sensitive to large
− droplets (precipitation)
− Susceptible to attenuation

Path-integrated attenuation

+ Near-linearly related to liquid water content
− Single value per column
− Low signal/noise ratio
− Over ocean only

Cloud optical depth

+ Sensitive to small droplets (cloud water)
− Single value per column
− Daytime only

### Lidar backscattering

+ Range resolved
+ More sensitive than radar (good for ice clouds)
+ Polarization: cloud phase
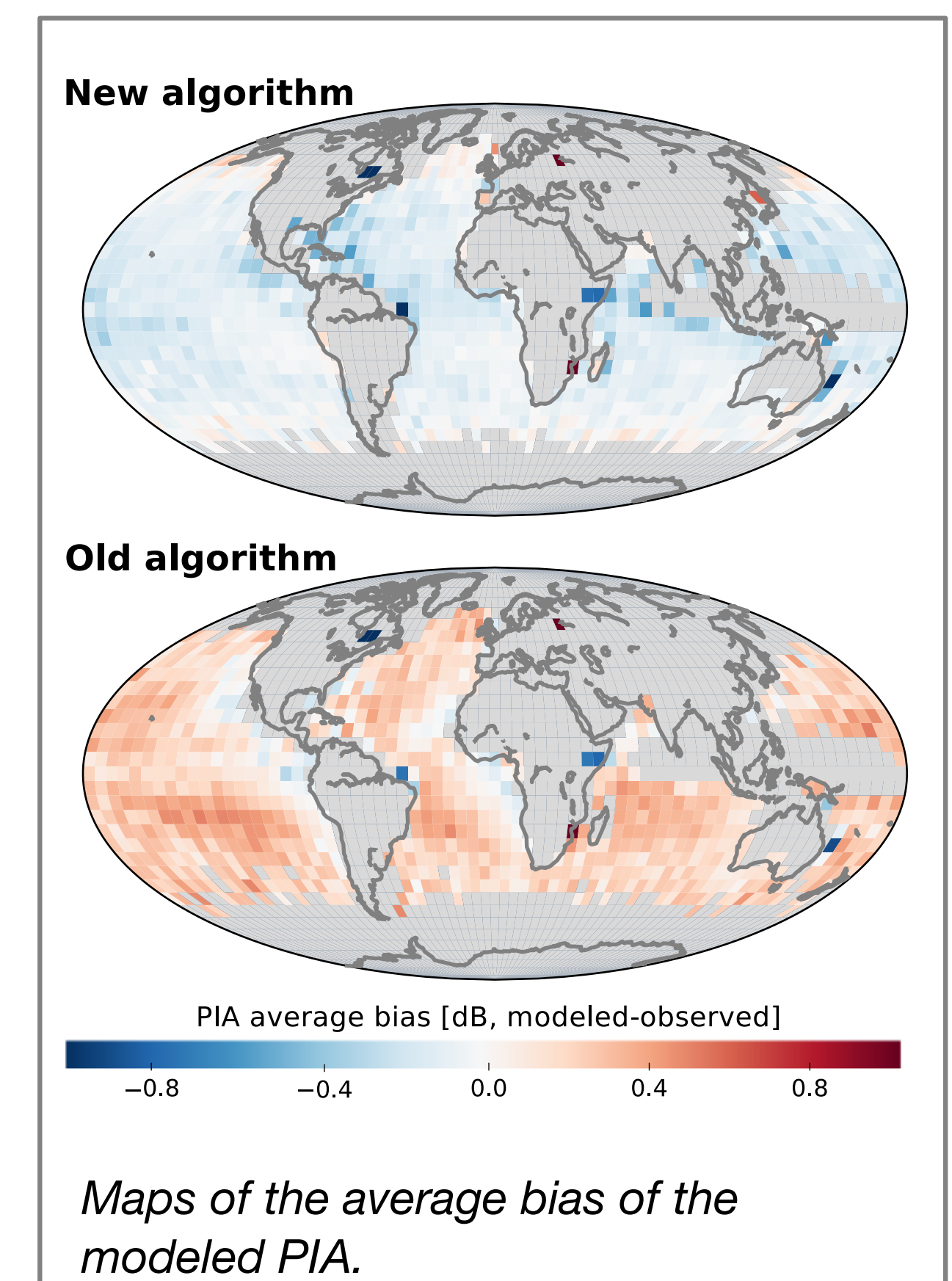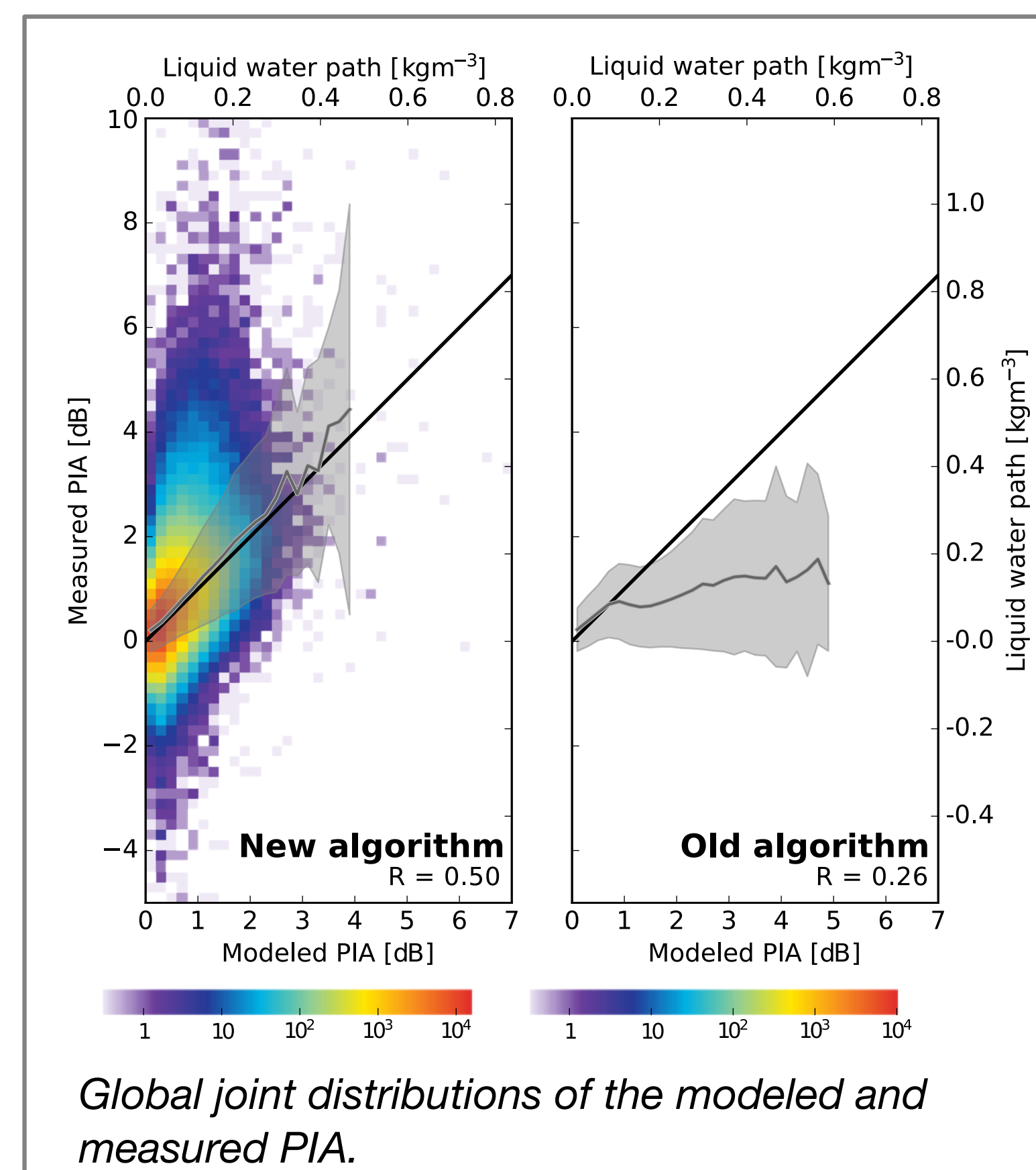− Very susceptible to attenuation

The new algorithm allows a wider range of values

The new algorithm retrieves, using optimal estimation, the cloud droplet geometric mean radius for each radar bin and a number concentration for the whole column. This reduces the number of unknown variables compared to the old version. A comparison of these values shows that the new algorithm permits a much wider range of retrieved values, while the old algorithm is very restrictive.

Global joint distributions of the retrieved cloud microphysical parameters.
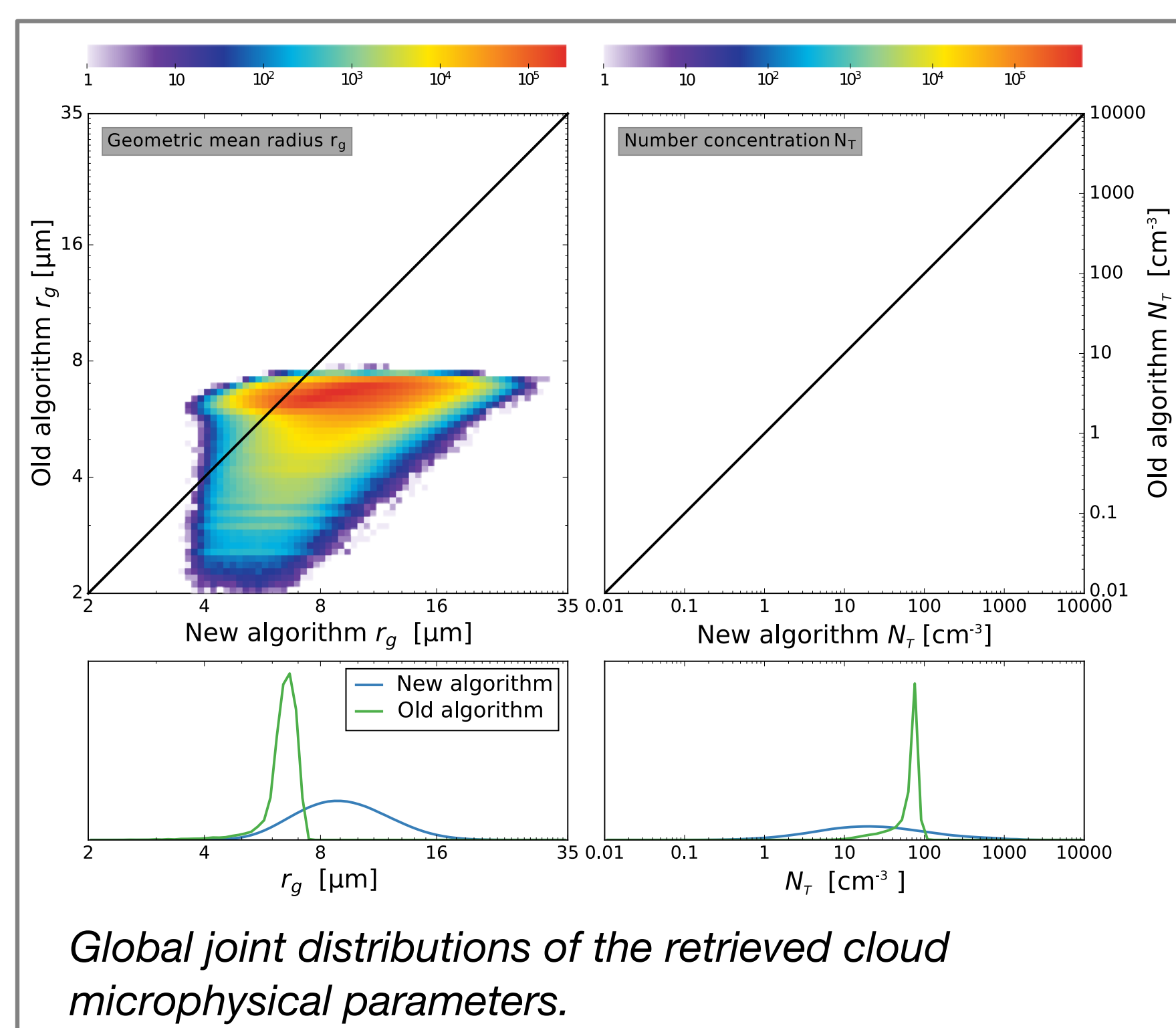
Cloud liquid water path is better reproduced by the new algorithm

Comparing the path-integrated attenuation (PIA) modeled by the algorithm to that obtained from surface-reference measurements, we can verify that the algorithm produces the correct liquid water path on average.


Global joint distributions of the modeled and measured PIA.

Maps of the average bias of the modeled PIA.

Hemispheric energy balance from an ocean perspective

Author: Maria Z. Hakuba (329J-Affiliate)
Graeme L. Stephens (3292)

Introduction

- Earth's energy balance and its radiative components have been studied for decades, but large uncertainties still exist, in particular at the **surface**
- Imbalance is a measure of climate change, but uncertainty ≥ imbalance
- Global mean has little to say about processes, e.g., meridional **heat transport** → regionalization is the key
- **Hemispheric energy** contrasts indicate how much heat must be moved (or stored) between hemispheres to reach energetic equilibrium

Stephens et al., 2012
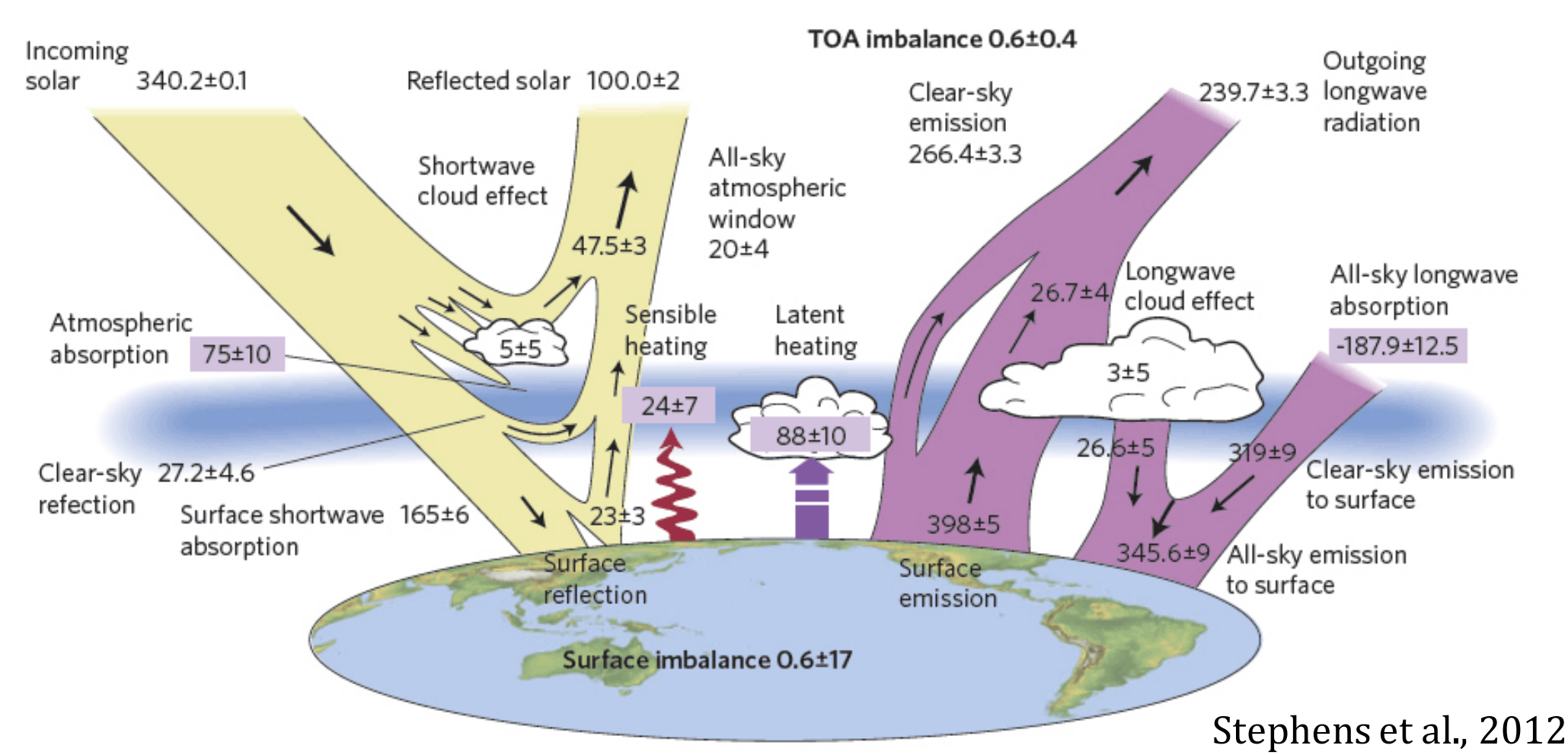
Objectives

1. Novel approach: Derive hemispheric surface heat budget (imbalance) from ocean heat data: storage + transport

2. Use surface heat budget to constrain and construct hemispheric energy balance and associated heat transports in combination with satellite-based radiation fluxes

Methods

- Hemispheric ocean heat storage (**OHS**) from in-situ ocean temperature profiles
- Oceanic cross-equatorial heat transport (**COHT**) from ocean reanalysis
- Surface heat budget: $F_s = OHS - COHT$ for each hemisphere
- CERES EBAF provides radiative fluxes at TOA:
  From F_s and **TOA** heat budget, we derive the atmospheric heat budget as residual
- CERES EBAF provides radiative fluxes at the surface:
  Together with F_s we estimate hemispheric **turbulent** fluxes

Results

Ocean heat storage (OHS)

Ocean heat content (OHC) derived from temperature profiles down to 2000 meters depth. Change in OHC over 20005-2015 = **OHS**
- **Global mean OHS: 0.5 Wm^{-2}**
- **Northern Hemisphere: 0.1 Wm^{-2}**
- **Southern Hemisphere: 0.9 Wm^{-2}**
- SH oceans dominate the OHS during the last decade.

OHS (ocean, Wm^{-2}): glo:0.7, nh:0.15, sh:1.1
OHS (global, Wm^{-2}): glo:0.5, nh: 0.1 , sh:0.9
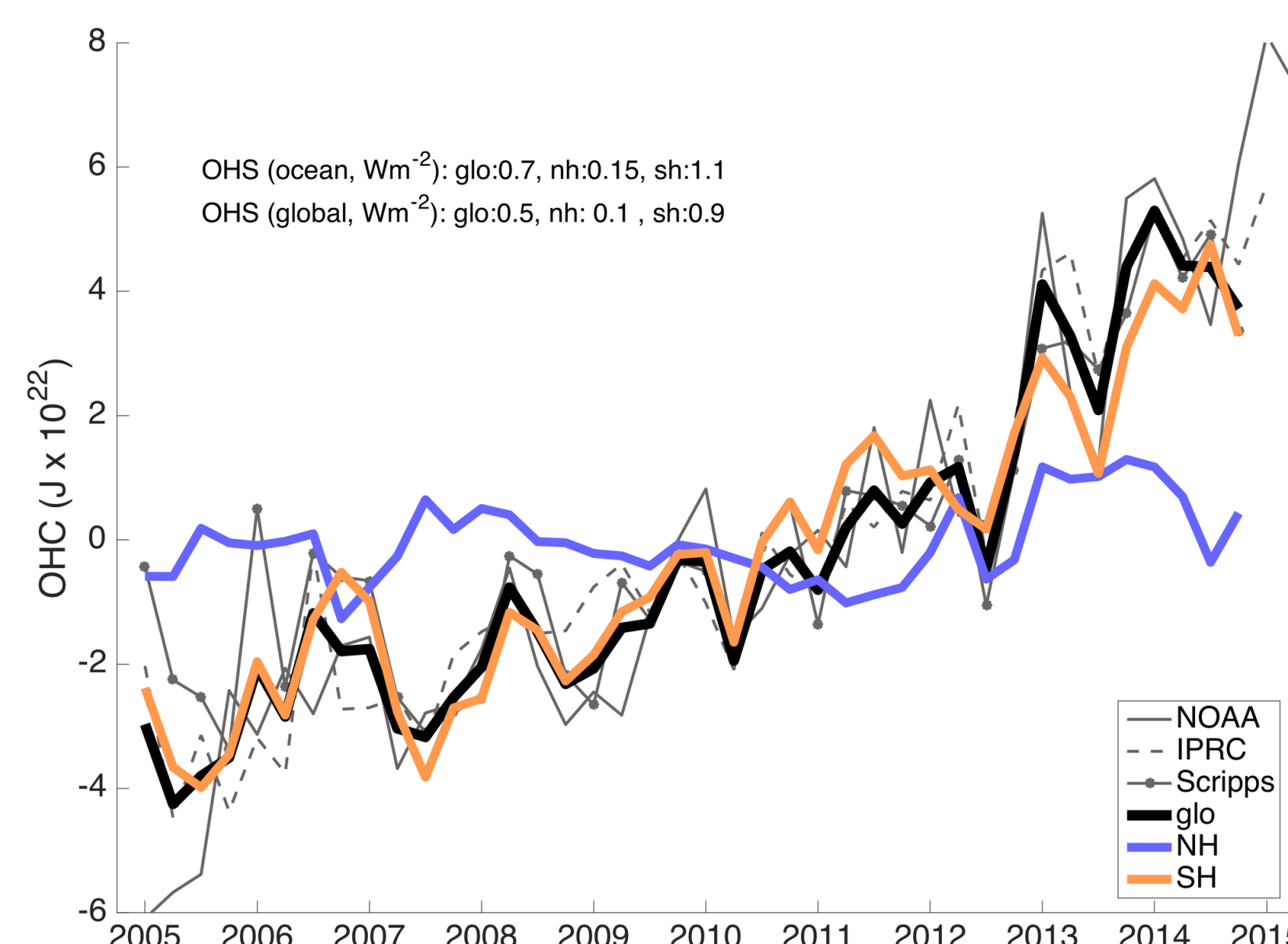
### Cross-equatorial heat transport (COHT)
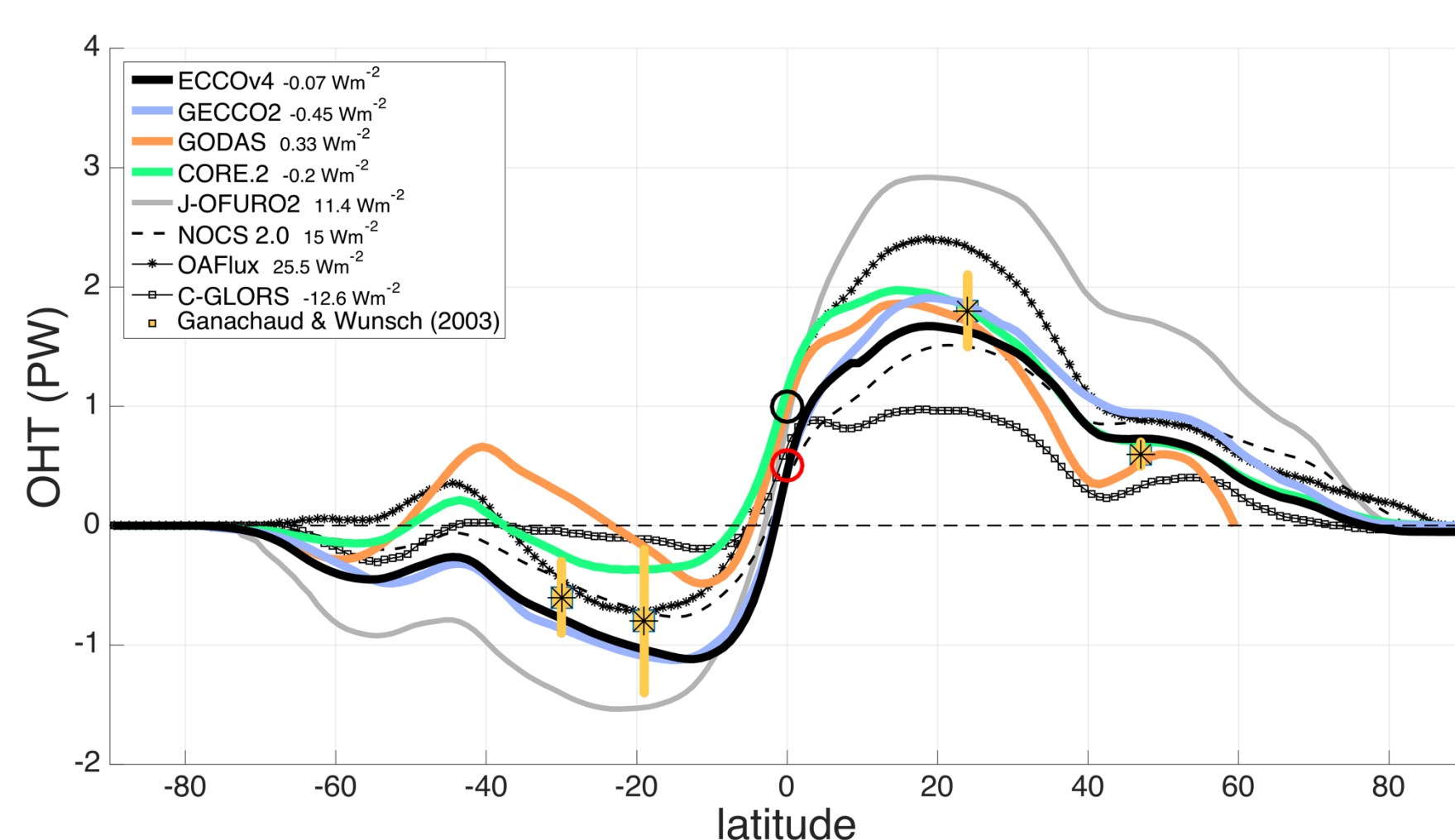
Oceanic meridional heat transport (OHT), derived from eight ocean reanalysis and observation-based datasets.
- Best estimate of cross-equatorial heat transport (**COHT**, red circle): 0.46 PW (1.8 Wm^{-2}) from the SH to NH.
- Derived from the four datasets that agree best with hydrographic estimates (asterisks).

Conclusions

- The hemispheric OHS and COHT are presented below and yield hemispheric $F_s = OHS - COHT$
- Positive heat flux into SH ocean, NH oceans release heat
- Together with CERES EBAF surface net radiation, we estimate the hemispheric turbulent fluxes (red)
- CERES EBAF at TOA implies a northward transport of heat, while atmospheric heat budget (residual of TOA and surface budget) requires a southward transport that partly compensates for the northward COHT.
- Previous studies suggest that this setup requires the ITCZ to be displaced slightly North of the equator in order to move heat in the atmosphere towards the SH
- Associated dynamics and their causes are subject of future research
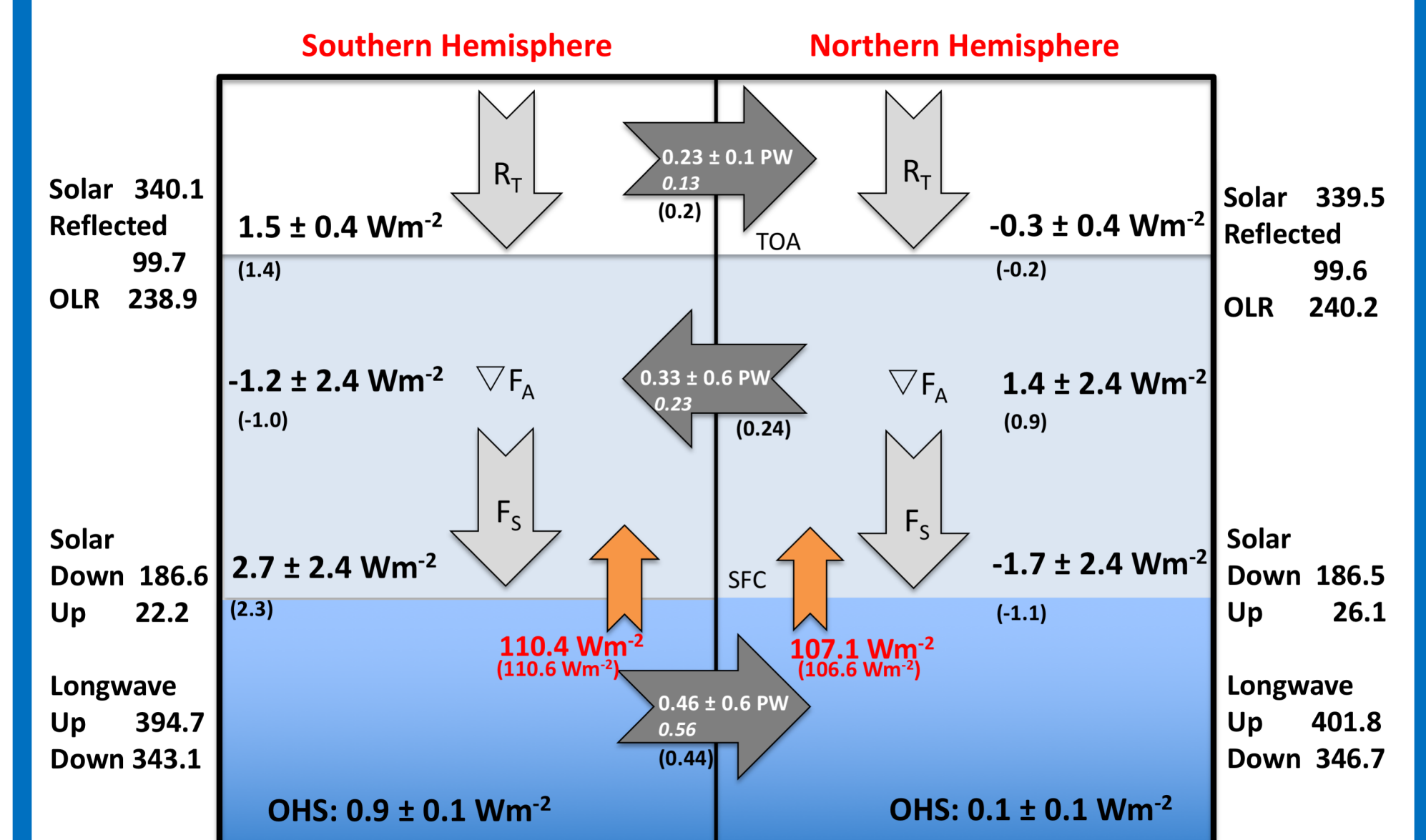
Acknowledgments

Poster No. EB-5

How Clouds Affect The Vertical Structure Of Radiative Heating Rates: A Multi-model Evaluation Using A-train Observations

Principal Investigator: Gregory Cesana (329J)
Co-Investigators: D. E. Waliser (8000), T. L'Ecuyer (Univ. of Wisconsin), X. Jiang (329J), J-L Li (329J)

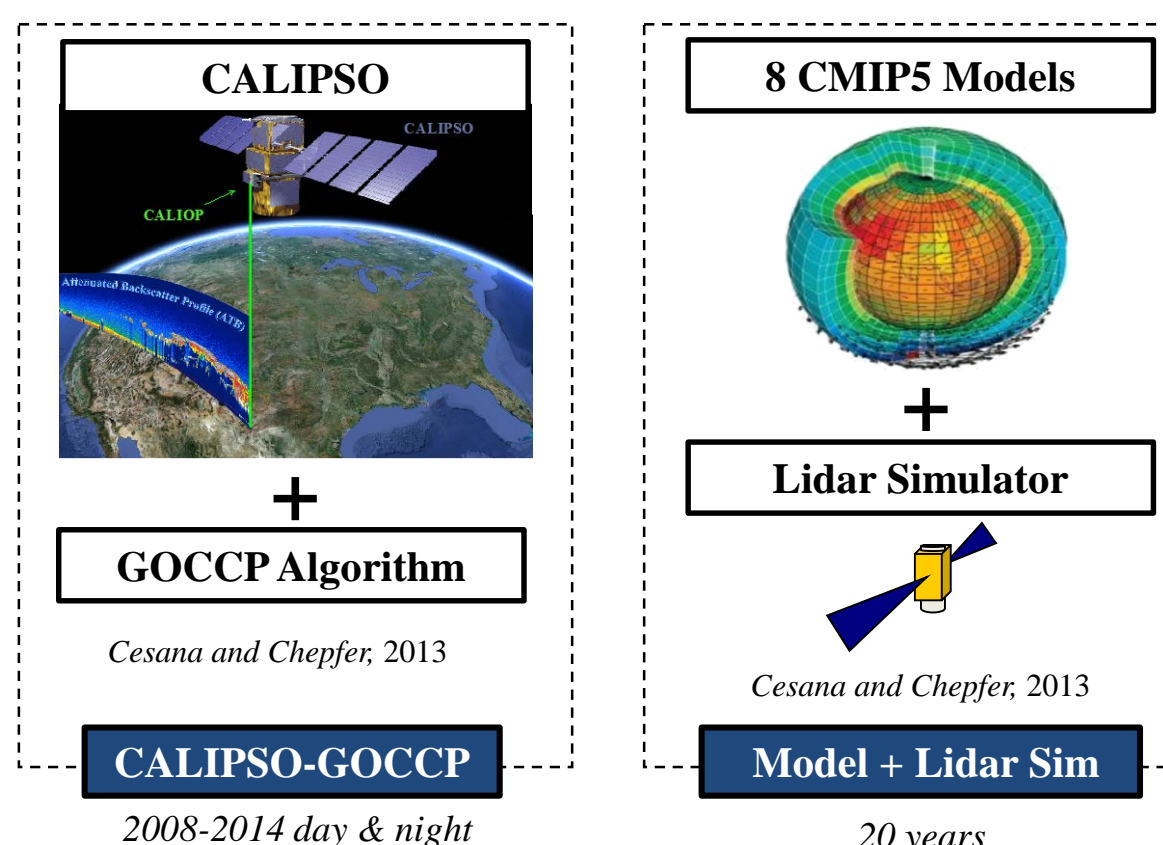## Context and Objectives

1. Context
Clouds strongly interact with radiation and modulate the amount of energy reflected, emitted and absorbed by the Earth system. The redistribution of energy within the troposphere has implications for climate prediction, as it impacts the large-scale circulation, the convection and precipitation. While passive sensor satellites have been monitoring outgoing and incoming radiative fluxes at the top of the atmosphere for years (CERES, TRMM), the vertical dimension is still missing and affects our ability to better understand the present climate and the climate response to a global warming as well.

2. Objectives
In this study, we take advantage of two modeling experiments (CMIP5 and GASS-YoTC) and A-train satellite observations (CloudSat/CALIPSO) to assess and characterize the vertical distribution of clouds in eight GCMs and their link with the radiative heating rate profiles.

Method

Simulator for Cloud Evaluation

CALIPSO
+
GOCCP Algorithm
Cesana and Chepfer, 2013
CALIPSO-GOCCP
2008-2014 day & night

8 CMIP5 Models
+
Lidar Simulator
Cesana and Chepfer, 2013
Model + Lidar Sim

Direct Comparison of Heating Rates

CloudSat/CALIPSO
+
Post-Process
L'Ecuyer et al., 2008
Cesana et al., (in prep)
Observed Heating Rate
2007-2010 day & night

8 GASS-YoTC Models
+
Post-Process
Jiang et al., 2015
Cesana et al., (in prep)
Simulated Heating Rate
20 years

Using the lidar simulator allows:
- Taking into account the instrument limitations
- Using the same cloud definition (threshold, grid, sampling)
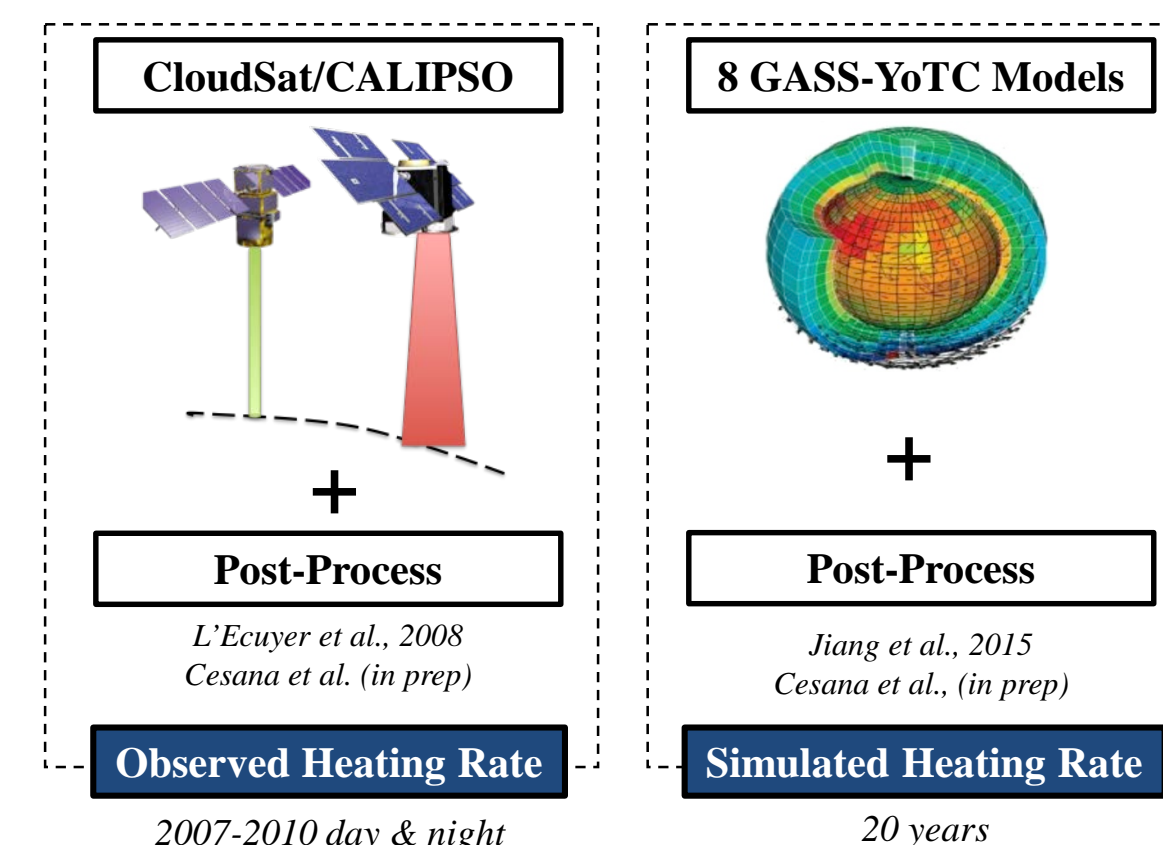
- All observations / simulations are projected onto the same grid
- SW heating rate are normalized by SW_{toa} fluxes to reduce uncertainties due to observation time sampling.

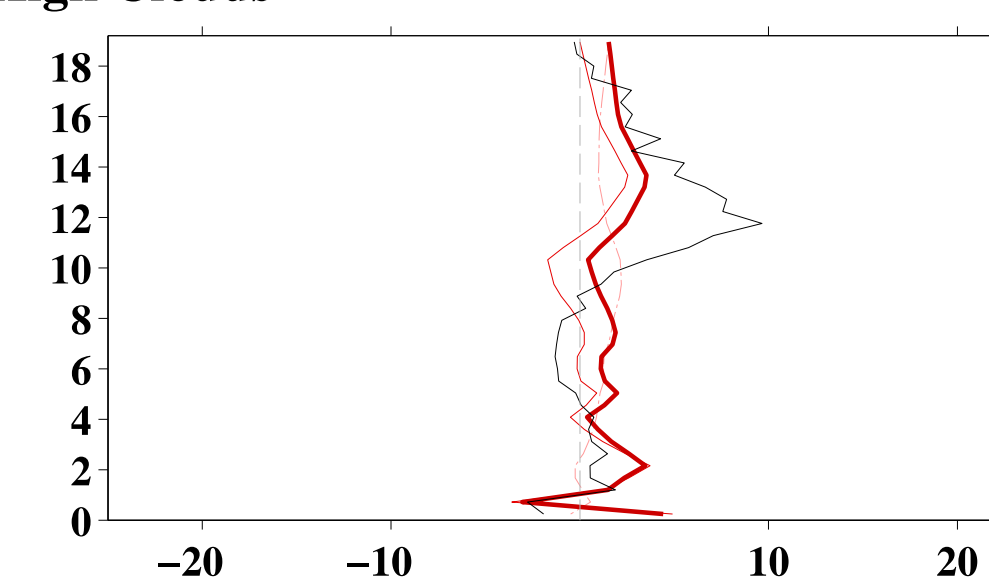## Zonal Mean Cloud Profile

Multi−Model Bias

- Overall pattern of clouds is well simulated (r=0.92 for multimodel mean)
- **too many high-level clouds** particularly in the tropics (*up to +15*)
- **too few low- and mid-level clouds** (*up to -15%*).
- Boundary layer height is too low

Latitude (°N)

Heating Rate Profile: Case Study

ITCZ High Clouds

Excess of high-level clouds (**black line**):
➔ Reduction of LW cooling above 11km (red thin line)
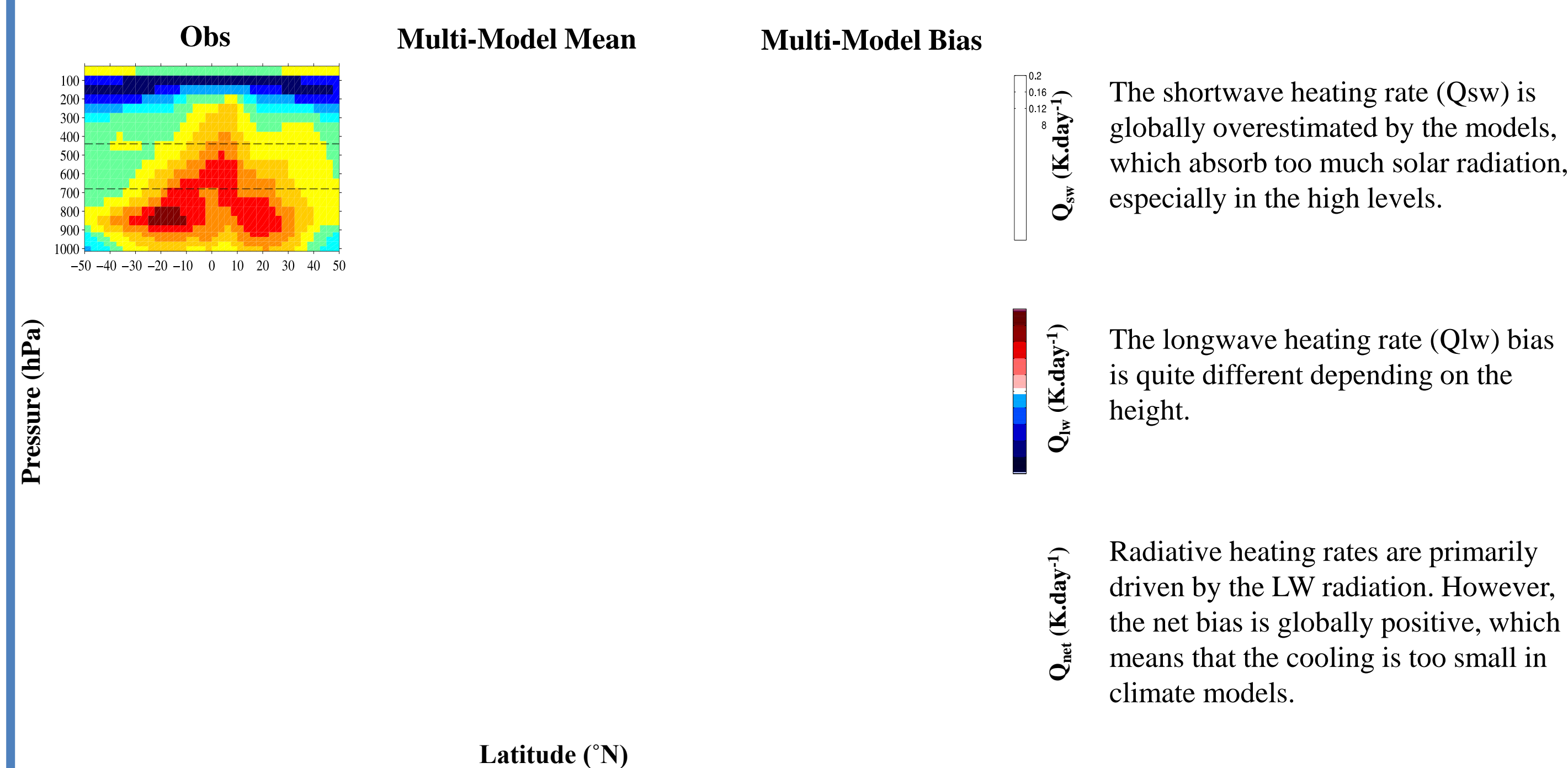➔ Increase of LW cooling below 11km

➔ Increase of the SW heating (absorption) toward the cloud base (red dashed-line)
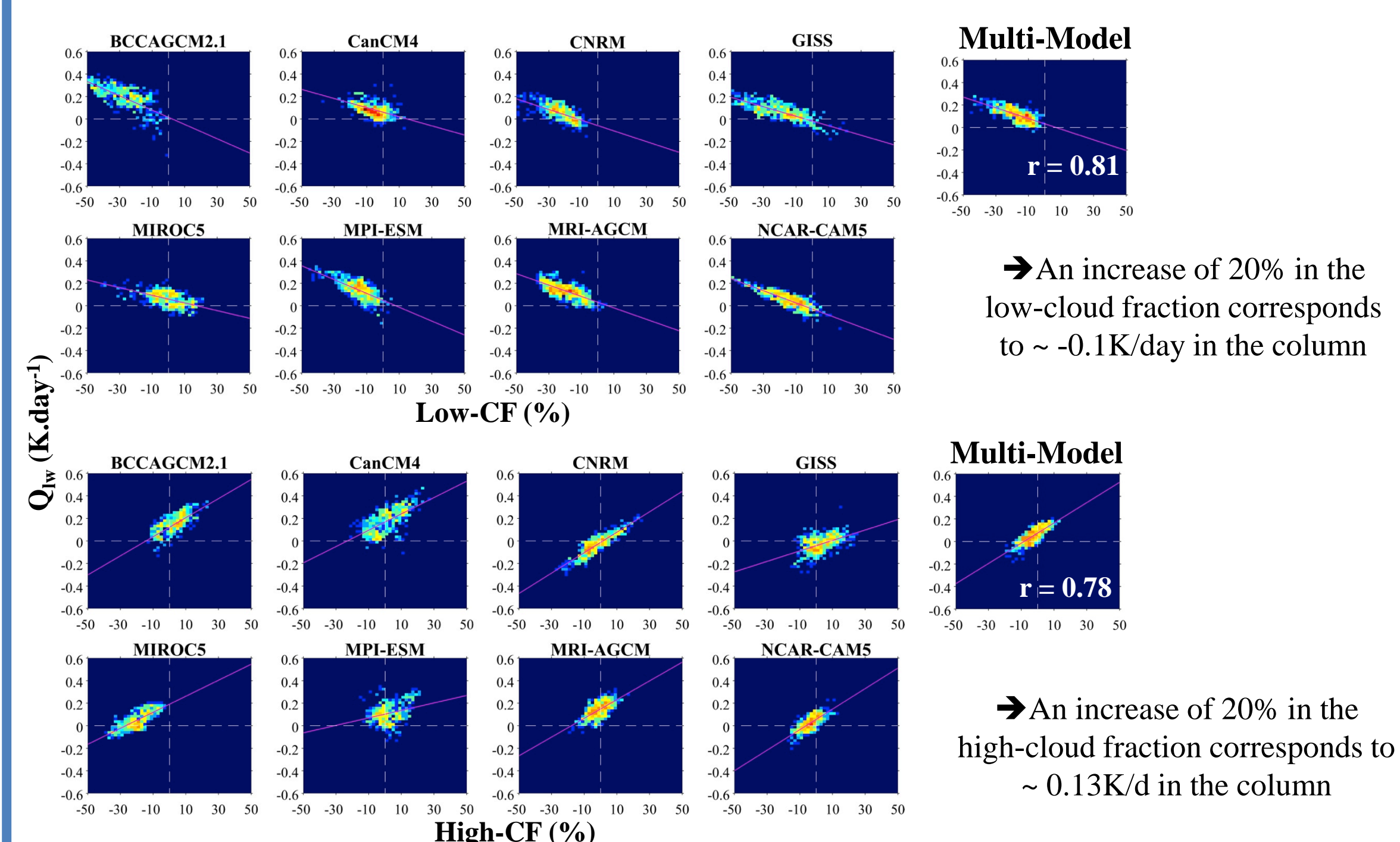
Stratocumulus Region

Qsw
Qlw
Qnet
CF

he LW cooling

Slight excess of high-level clouds:
➔ Similar biases than the previous case.

Significant deficit of low-level clouds (up to 20%):
➔ Large underestimation of the LW cooling (up to 2.5 K/d)
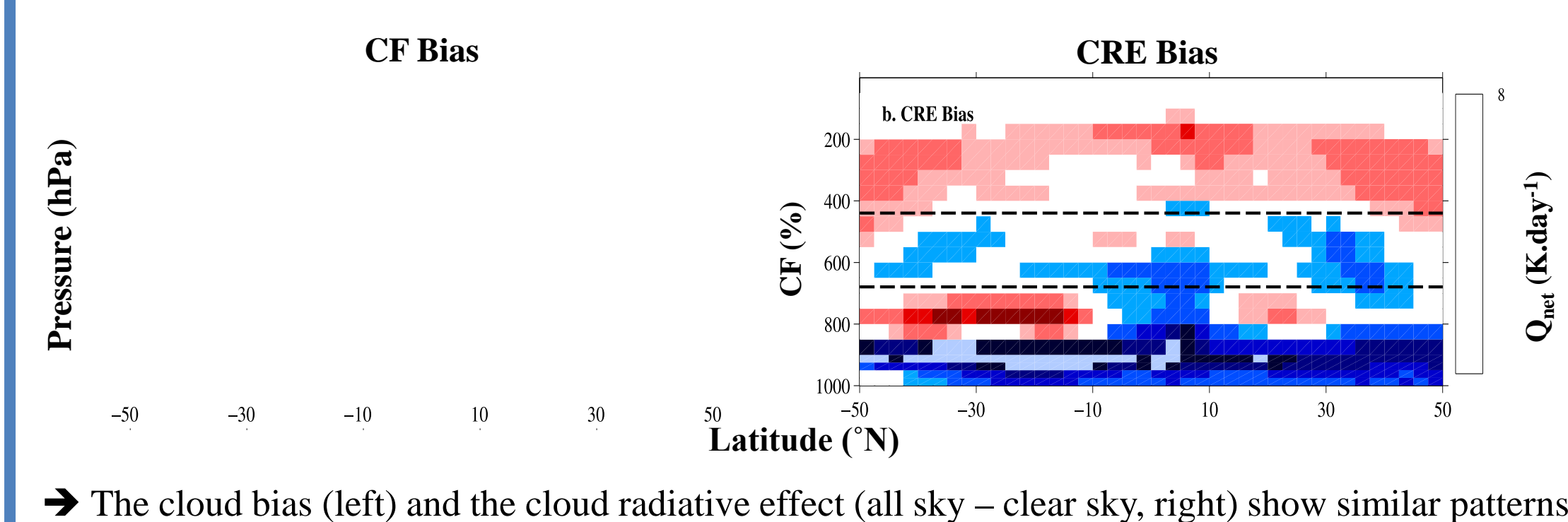➔ Partly compensated by more LW radiation trapped in the lowest layers

Zonal Mean Heating Rate Profile

Obs   **Multi-Model Mean**   **Multi-Model Bias**

Pressure (hPa)

Q_{sw} (K.day^{-1})

The shortwave heating rate (Qsw) is globally overestimated by the models, which absorb too much solar radiation, especially in the high levels.

Q_{lw} (K.day^{-1})

The longwave heating rate (Qlw) bias is quite different depending on the height.

Q_{net} (K.day^{-1})

Radiative heating rates are primarily driven by the LW radiation. However, the net bias is globally positive, which means that the cooling is too small in climate models.

Latitude (°N)

Correlation Between Cloud And Heating Rate Bias

BCCAGCM2.1   CanCM4   CNRM   GISS   **Multi-Model**

Q_{lw} (K.day^{-1})

MIROC5   MPI-ESM   MRI-AGCM   NCAR-CAM5

Low-CF (%)

r = 0.81

➔An increase of 20% in the low-cloud fraction corresponds to ~ -0.1K/day in the column

BCCAGCM2.1   CanCM4   CNRM   GISS   **Multi-Model**

MIROC5   MPI-ESM   MRI-AGCM   NCAR-CAM5

High-CF (%)

r = 0.78

➔An increase of 20% in the high-cloud fraction corresponds to ~ 0.13K/d in the column

Cloud Radiative Effect

CF Bias   **CRE Bias**

a. CF Bias   b. CRE Bias

Pressure (hPa)   CF (%) Q_{net} (K.day^{-1})

Latitude (°N)

➔ The cloud bias (left) and the cloud radiative effect (all sky – clear sky, right) show similar patterns

Summary

We addressed systematic biases in the representation of cloud profiles and their effects on heating rate profiles in recent climate models, using vertically-resolved satellite measurements.

Obs ━━   Model ━━
Shortwave Longwave   Shortwave Longwave

Qnet (K.d^{-1})   CF(%)
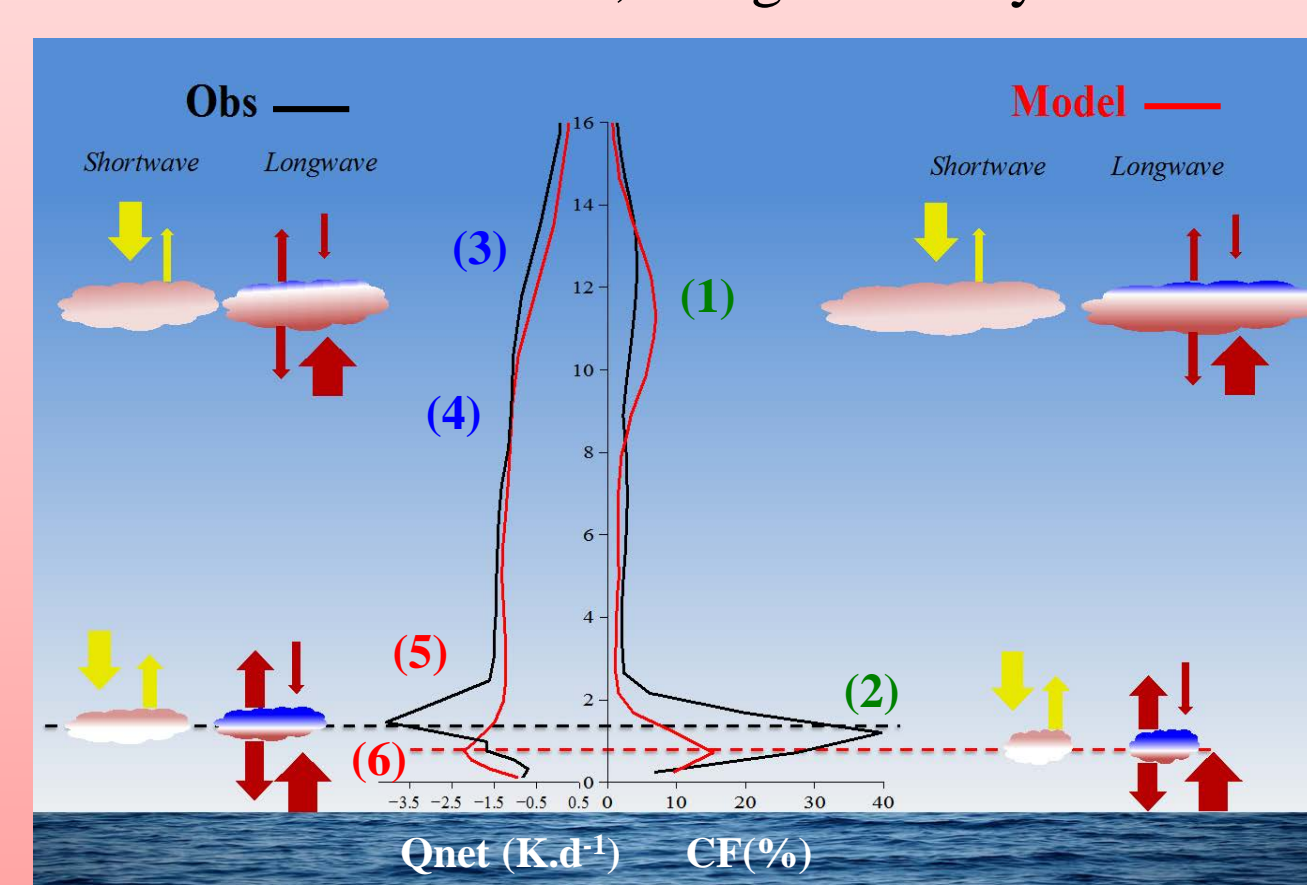
- Most climate models simulate too many high-level clouds **(1)** and too few low-level clouds **(2)**

- The excess of high-cloud increases the solar absorption (heating) and may either trap too much LW radiation (>11km **(3)**) or generate too much LW cooling (<11km **(4)**) depending on the height.

- The lack of low-cloud causes a strong reduction of the LW cooling in the vicinity of the cloud **(5)** and an increase of the LW cooling and the solar absorption close to the surface **(6)**.

The role of winter mean moisture in climate model simulations of the Madden-Julian oscillation

Author: Alex O. Gonzalez (329)
Co-Author: Xianan Jiang (329)

Introduction

The Madden-Julian oscillation (MJO) is a multi-scale storm system initiating in the tropical Indian Ocean and propagating eastward at 5–10 m s^{-1} on 30–90 day timescales, mainly during boreal winter. It is the dominant mode of intraseasonal variability in Earth's climate system, impacting many atmospheric phenomena such as extreme rainfall/droughts, monsoons, hurricanes, El Niño Southern Oscillation, and extratropical weather systems.

Problem

- The majority of Global Climate Models (GCMs) struggle to simulate the MJO, especially its observed eastward propagation [3], as demonstrated in Fig. 1.

- Improving the MJO in atmospheric models is vital to medium- and long-range weather forecasting [2].

- Deficiencies in MJO propagation have been attributed primarily to either horizontal or vertical moisture advection, depending on the individual event [4].

- Recent analyses suggest the horizontal advection of the winter mean moisture by the MJO circulation plays a critical role in the observed eastward propagation of the MJO, e.g., [1].
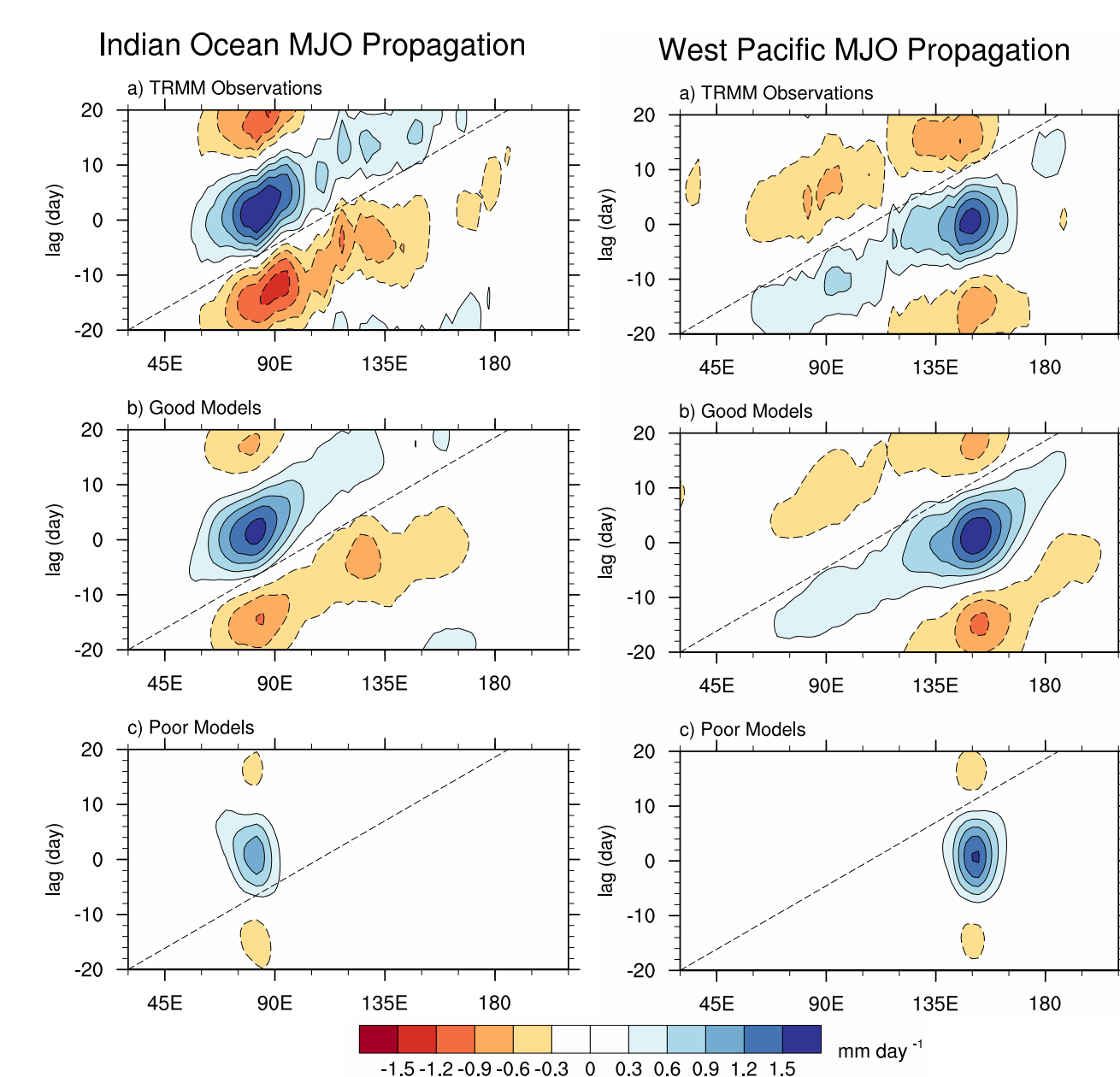
Figure 1: MJO propagation via 15°S–15°N averaged 20–100 day filtered rainfall anomalies regressed against themselves in the Indian Ocean (West Pacific) base region on left (right). Adapted from [3].

Main objectives

1. Investigate the relationship between the winter mean moisture field and the propagation of the MJO using a suite of 23 GCM simulations and TRMM (Tropical Rainfall Measuring Mission, 3B42v7) satellite observations and ERA-Interim (European Centre for Medium-Range Weather Forecasts Interim Re-Analysis).
2. Determine in what region(s) the winter mean moisture is most important to the observed MJO propagation in the Indian Ocean and West Pacific.
3. Formulate a diagnostic metric to be used by weather and climate prediction models.
4. Explain the physical mechanisms linking winter mean moisture to MJO propagation.

Winter mean low-level moisture

- The top (bottom) six GCM simulations in MJO propagation skill are categorized as good (poor) MJO models.

- The low-level (650–900 hPa) moisture pattern and amplitude in good MJO models are in much better agreement with ERA-Interim than poor MJO models.

- Poor MJO models are especially dry in the deep tropics and in the region surrounding the Maritime Continent.

- Winter mean horizontal moisture gradients are significantly larger in good MJO models, allowing for horizontal advection to be a viable mechanism for MJO propagation.
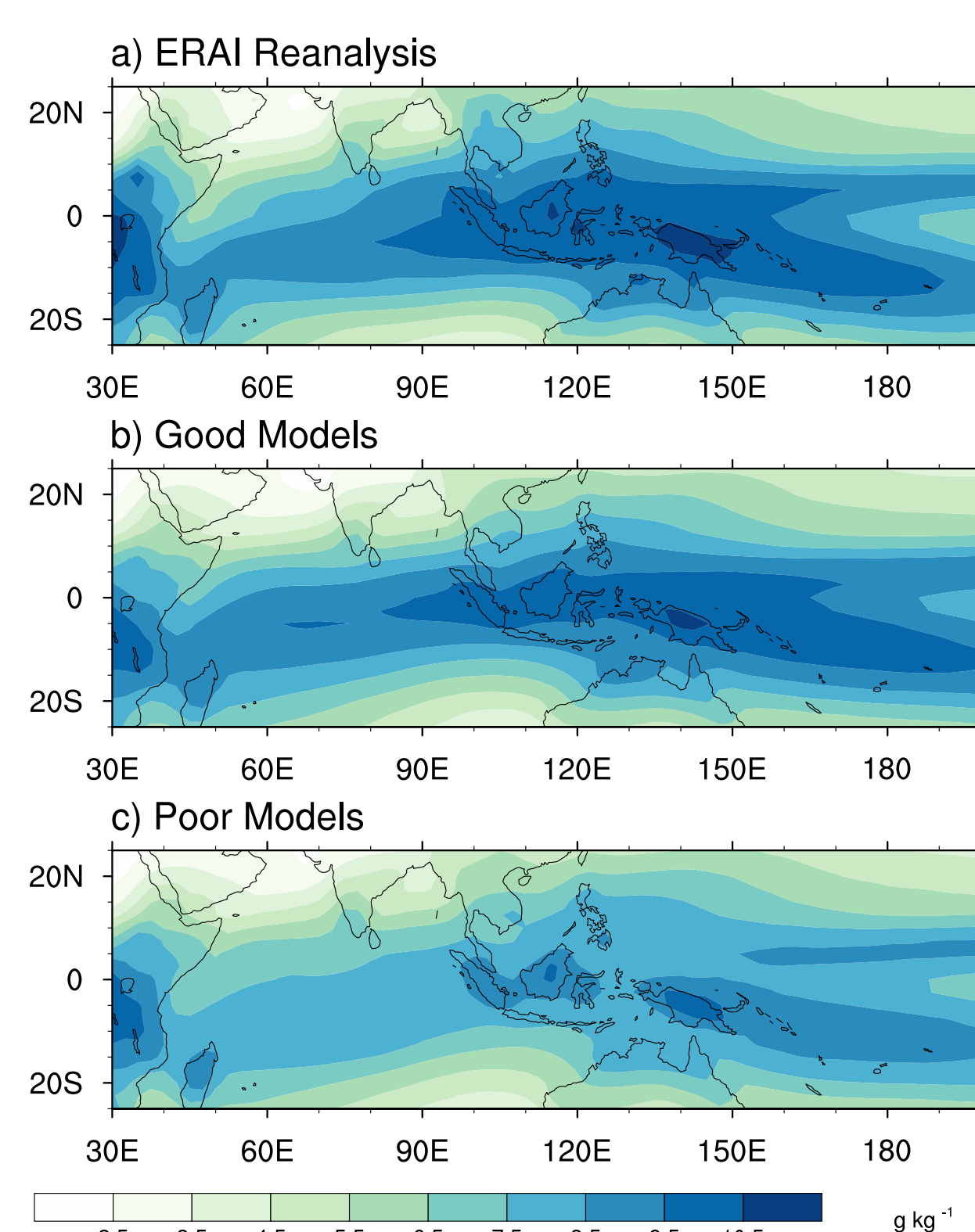
Figure 2: Winter mean specific humidity averaged over 650–900 hPa for a) ERA-Interim, b) good MJO models, and c) poor MJO models.

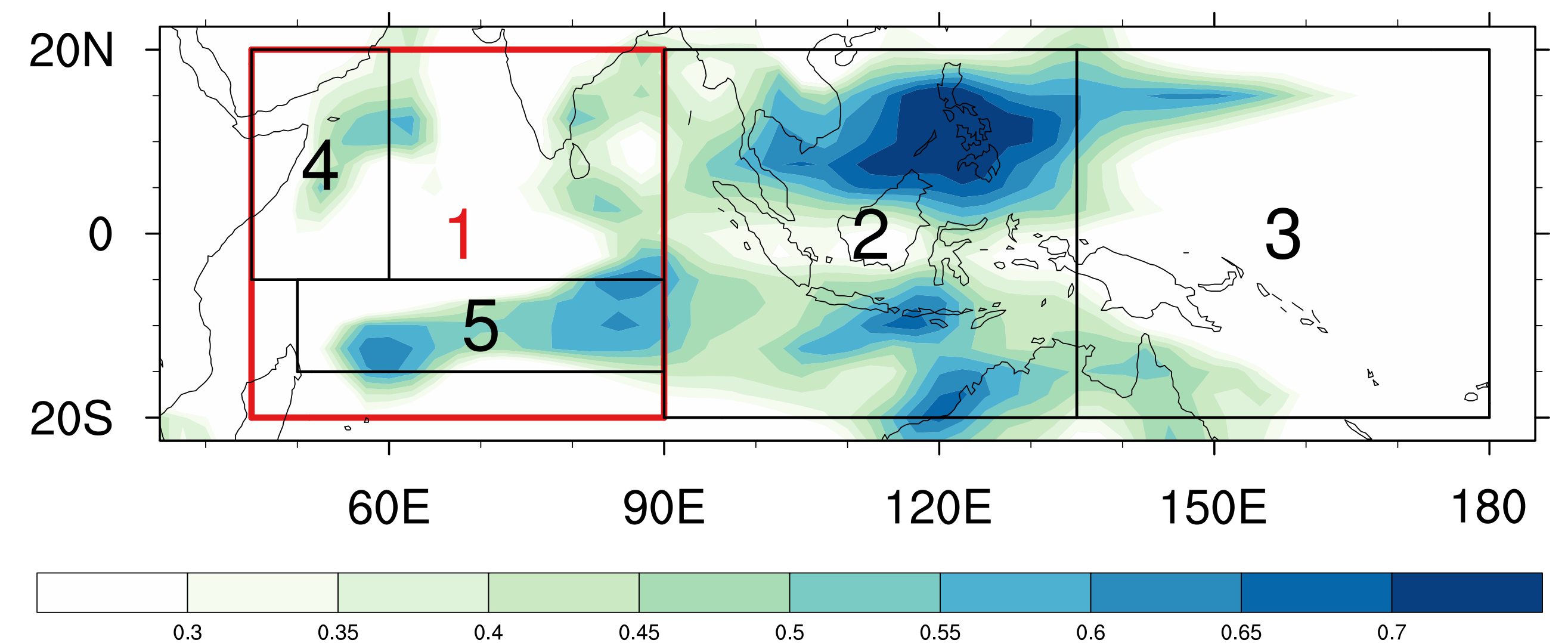## Correlations between winter moisture and MJO propagation

Figure 3: Correlation between the low-level averaged winter mean specific humidity pattern correlation (15° × 15° boxes centered at each grid point) and mean MJO propagation skill. Black boxes denote subregions for calculations in Table 1.

- The winter mean moisture pattern in the region surrounding the Maritime Continent has the most robust relationship with MJO propagation.
- This relationship likely involves large scale physical processes and is not isolated to processes occurring over the land masses in the Maritime Continent.

Specific Humidity Region	Specific Humidity Location	IO MJO Propagation	WP MJO Propagation	Mean MJO Propagation
1) Indian Ocean	(60°–90°E, 20°S–20°N)	0.48	0.51	0.54
2) Maritime Continent	(90°–135°E, 20°S–20°N)	**0.77**	**0.72**	**0.80**
3) Western Pacific	(135°–180°E, 20°S–20°N)	0.11	0.31	0.23
4) Western Indian Ocean	(45°–60°E, 5°S–20°N)	**0.63**	0.34	0.52
5) Indian Ocean ITCZ	(50°–90°E, 15°S–5°S)	**0.64**	**0.67**	**0.71**
6) Indo-Pacific	(45°–180°E, 20°S–20°N)	0.44	0.53	0.53

Table 1: Correlations between specific humidity pattern correlation and MJO propagation skill.
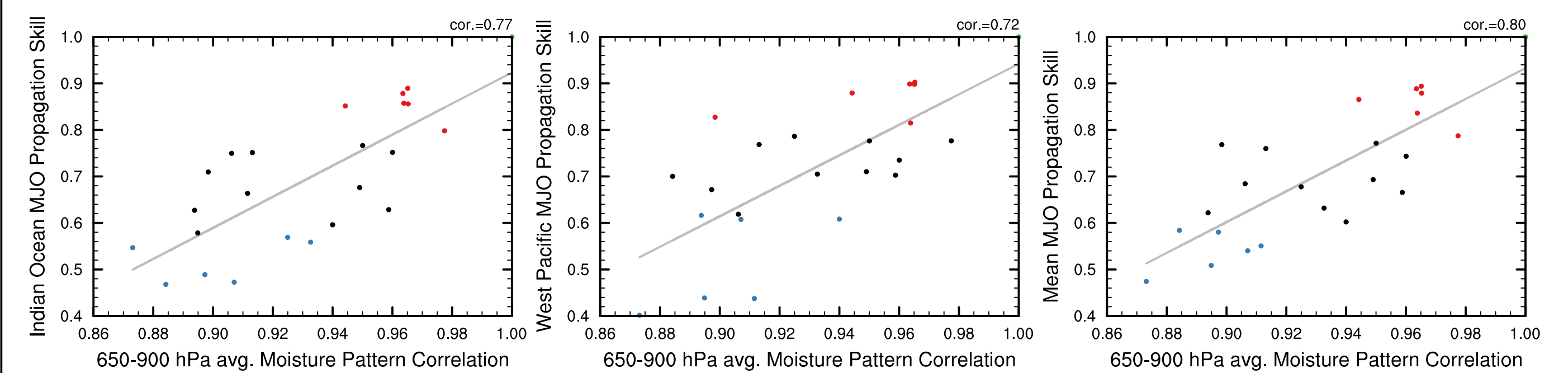
Figure 4: Scatterplot of the Maritime Continent low-level winter mean specific humidity pattern correlation and MJO propagation skill. Red, blue, black, and green dots represent good, poor, other MJO models, and observations respectively.

Conclusions

- MJO eastward propagation is well correlated with the winter mean specific humidity pattern, particularly over the Maritime Continent and the Indian Ocean ITCZ.
- Horizontal advection of the winter mean moisture by the intraseasonal wind anomalies is significantly larger in good MJO models, implying more accurate MJO propagation.
- The winter mean specific humidity pattern, with emphasis over the Maritime Continent, can be used as a simple diagnostic metric to assess the accuracy of the MJO in GCMs.

References

[1] Á. F. Adames and J. M. Wallace. Three-dimensional structure and evolution of the moisture field in the MJO. *J. Atmos. Sci.*, 72(10):3733–3754, 2015.

[2] L. Ferranti, T. N. Palmer, F. Molteni, and E. Klinker. Tropical-extratropical interaction associated with the 30–60 day oscillation and its impact on medium and extended range prediction. *J. Atmos. Sci.*, 47(18):2177–2199, 1990.

[3] X. Jiang and Coauthors. Vertical structure and physical processes of the Madden-Julian oscillation: Exploring key model physics in climate simulations. *J. Geophys. Res. Atmos.*, 120(10):4718–4748, 2015.

[4] A. Sobel, S. Wang, and D. Kim. Moist Static Energy Budget of the MJO during DYNAMO. *J. Atmos. Sci.*, 71(11):4276–4291, 2014.

Acknowledgements

Poster No. EB-8

Application of 3D MoM/CBFM Technique to the Problem of Electromagnetic Scattering by Complex-Shaped Precipitation Particles

**Ines Fenni *, Ziad S. Haddad *, Hélène Roussel ****

* Radar Science (334H), Jet Propulsion Laboratory, USA
** UPMC Univ Paris 06, UR2, L2E, F-75005, Paris, France

I – Introduction :

Earth-Science missions aimed at the observation of clouds and precipitation require the development of a coherent EM scattering model to accurately calculate the absorption and scattering properties of inhomogeneous dielectric particles with complex geometries representing snowflakes of various sizes and shapes. In this work, we apply a powerful domain decomposition technique known as the Characteristic Basis Function Method (CBFM), to the problem of EM scattering by complex-shaped particles, and this, in the context of a 3D full-wave model based on the volume-integral equation formulation of the electric fields (EFIE) . Our main goal is to take advantage of the high computational efficiency of the CBFM and its associated good level of accuracy when modeling the problem of EM scattering by complex-shaped precipitation particles.

II – Application of the CBFM to the problem of scattering by complex particles :
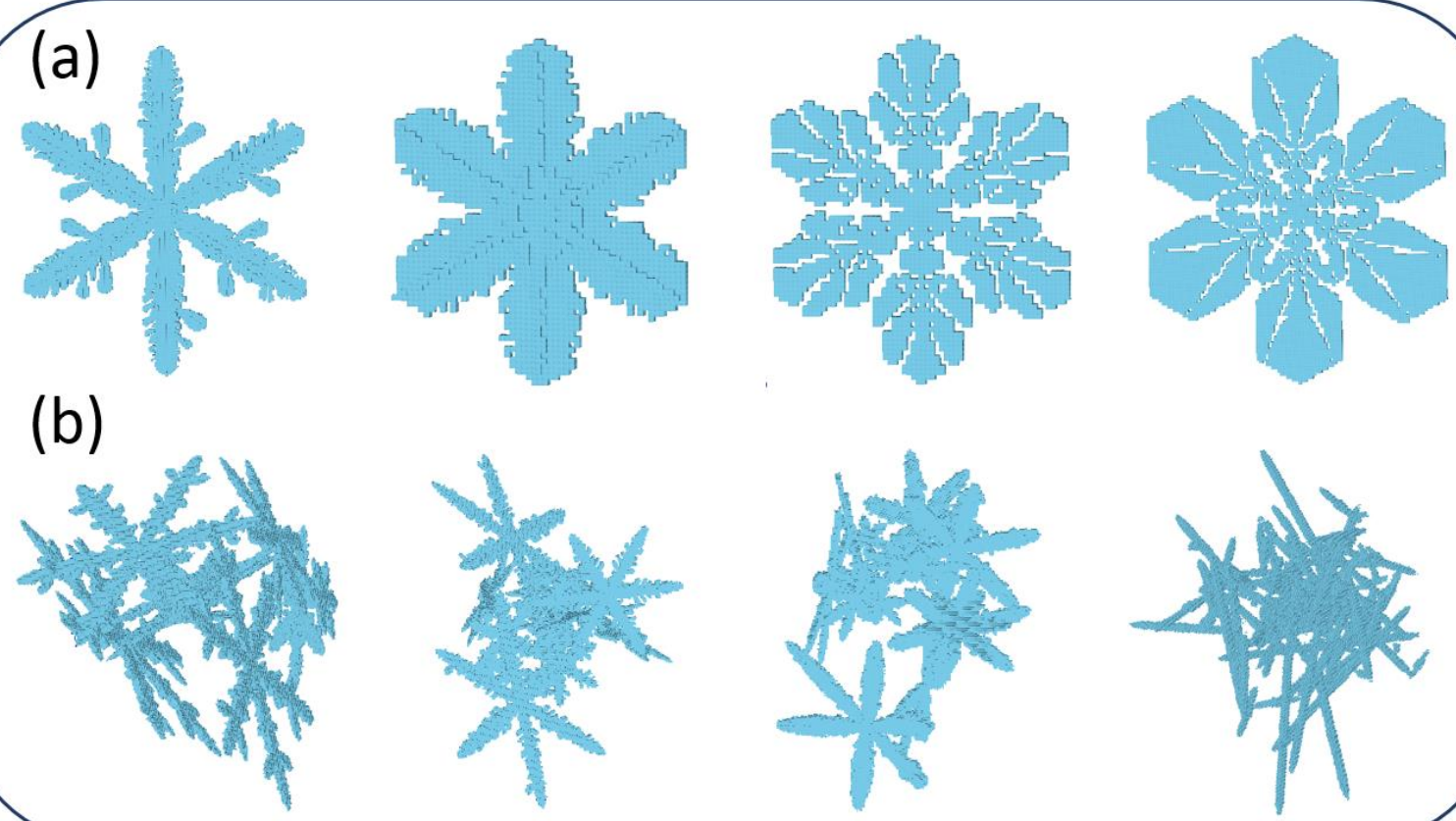
Pristine crystals **(a)** simulated using the snowflake algorithm [1] and aggregate snow particles **(b)**

Frequencies of interest :
(35 - 180 GHz)

3D full-wave model based on the integral representation of the electric field

Method of Moments (MoM)

$$T_c = \frac{\lambda_s}{10} \quad ; \quad \lambda_s = \frac{\lambda_0}{\sqrt{Re(\varepsilon_r)}}$$

### Integral representation of the total electric field (EFIE) :

$$\overline{E}(\overline{r}) = \overline{E}^{ref}(\overline{r}) + (k_0^2 + \nabla\nabla.)\int_\Omega \chi(\overline{r}') \overline{\overline{G}}(\overline{r},\overline{r}') \overline{E}(\overline{r}') d\overline{r}'$$

where $\chi(\overline{r}')$ is the dielectric contrast at the location r', k_0 is the wavenumber in air and $\overline{\overline{G}}(\overline{r},\overline{r}')$ is the free space dyadic Green's function.

Application of the Characteristic Basis Function Method :

After dividing the 3D complex geometry of the precipitation particle of **N** cells into **M** blocks, the **CBFM** procedure [2] consists in generating S_i Characteristic Basis Functions (CBFs) for each block **i** in order to generate a final reduced matrix of size **K x K** where **K = Sum ($S_1, S_2, … S_M$)**

Generation of the CBFs

N_{IPWs}
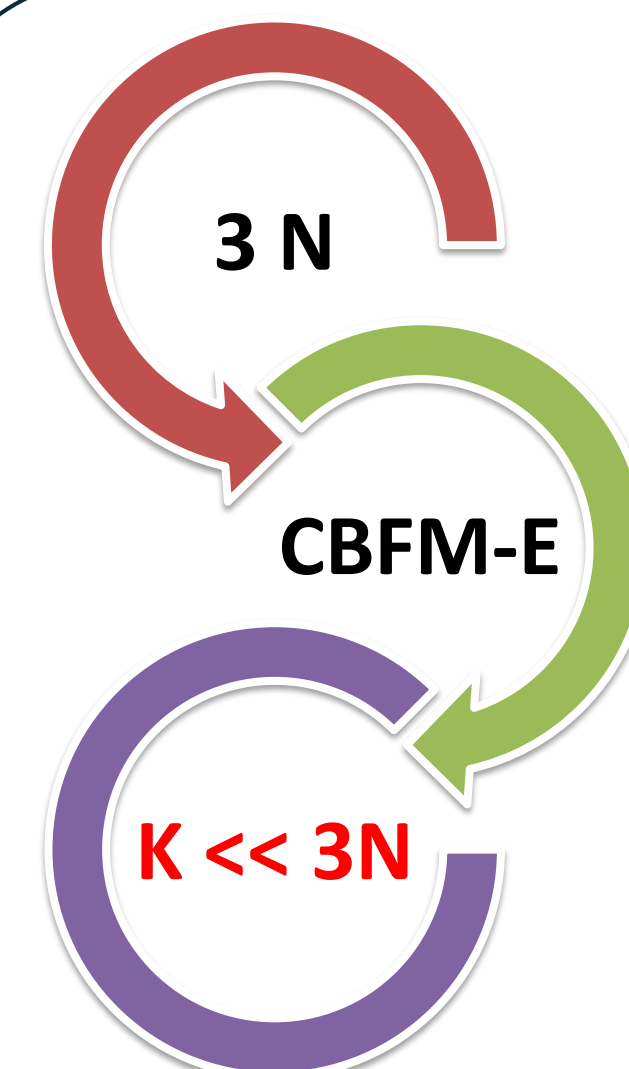

Block i
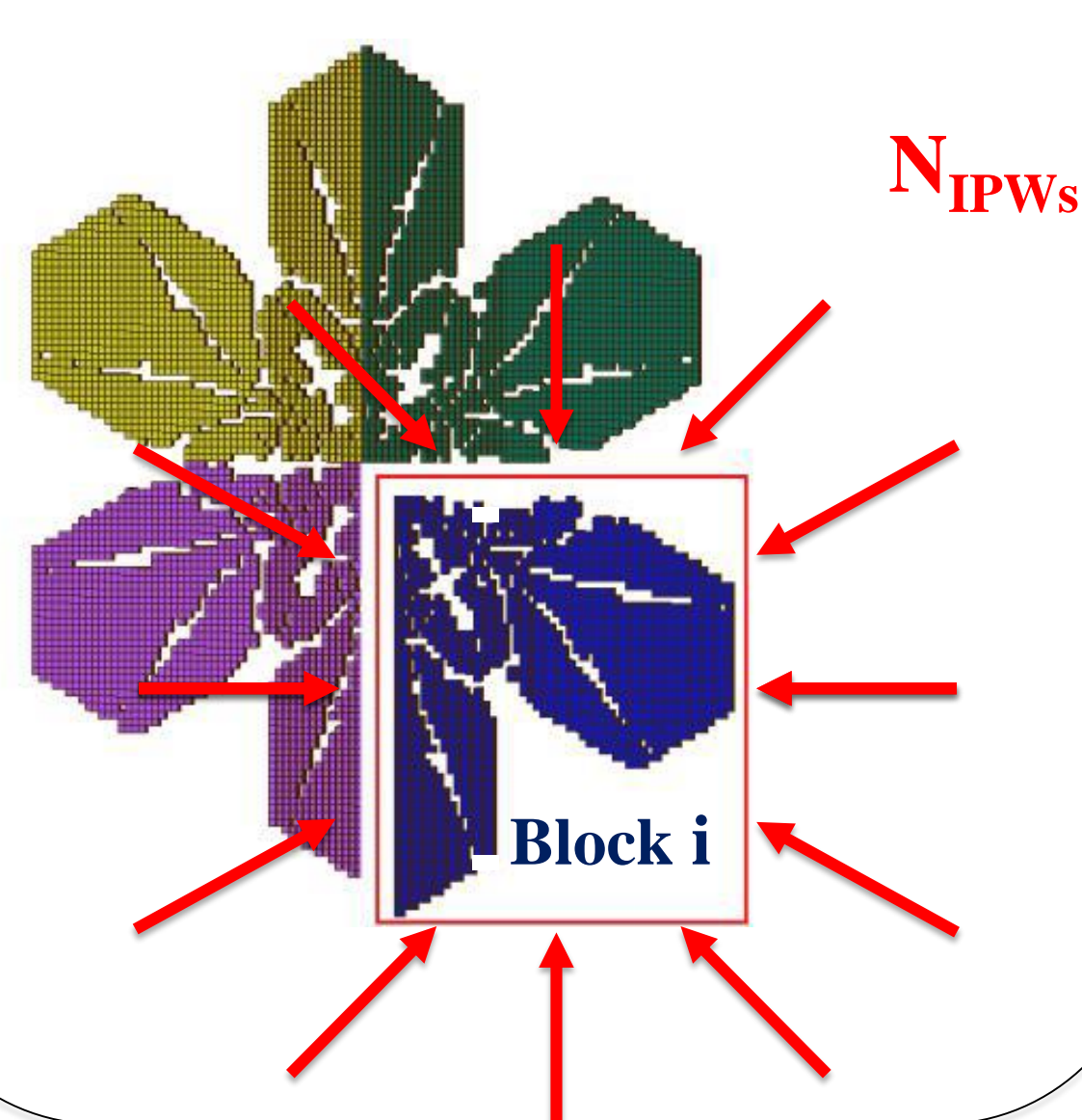
Computation of Z^c

Example : M = 4

$$Z^c = \begin{pmatrix} C^{(1)t} Z_{11} C^{(1)} & \cdots & C^{(1)t} Z_{14} C^{(4)} \\ C^{(2)t} Z_{21} C^{(1)} & \cdots & C^{(2)t} Z_{24} C^{(4)} \\ \vdots & \ddots & \vdots \\ C^{(4)t} Z_{41} C^{(1)} & \cdots & C^{(4)t} Z_{44} C^{(4)} \end{pmatrix}$$
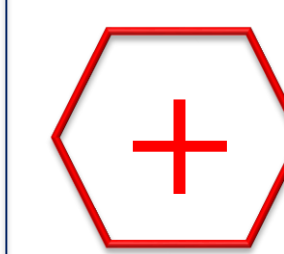
K = $S_1 + S_2 + S_3 + S_4$ << 3*N

Compression Rate

$$ICR\ (\%) = 100 \times \frac{size\ of\ Z^c}{size\ of\ Z^{MoM}}$$

By storing and solving the resulting reduced system of equations, instead of the original one, we are able to achieve a significant gain both in terms of CPU time and required memory.

3 N

CBFM-E

K << 3N

Enhancement techniques are employed to substantially reduce the CPU time required to compute the CBFs and to generate the reduced matrix.

1. Diagonal representation of the MBFs

$(3N_i)^3$

$$E_i^{(\theta,\varphi)} = Z_{ii}^{-1} E_i^{ref,(\theta,\varphi)}$$

$3N_i$

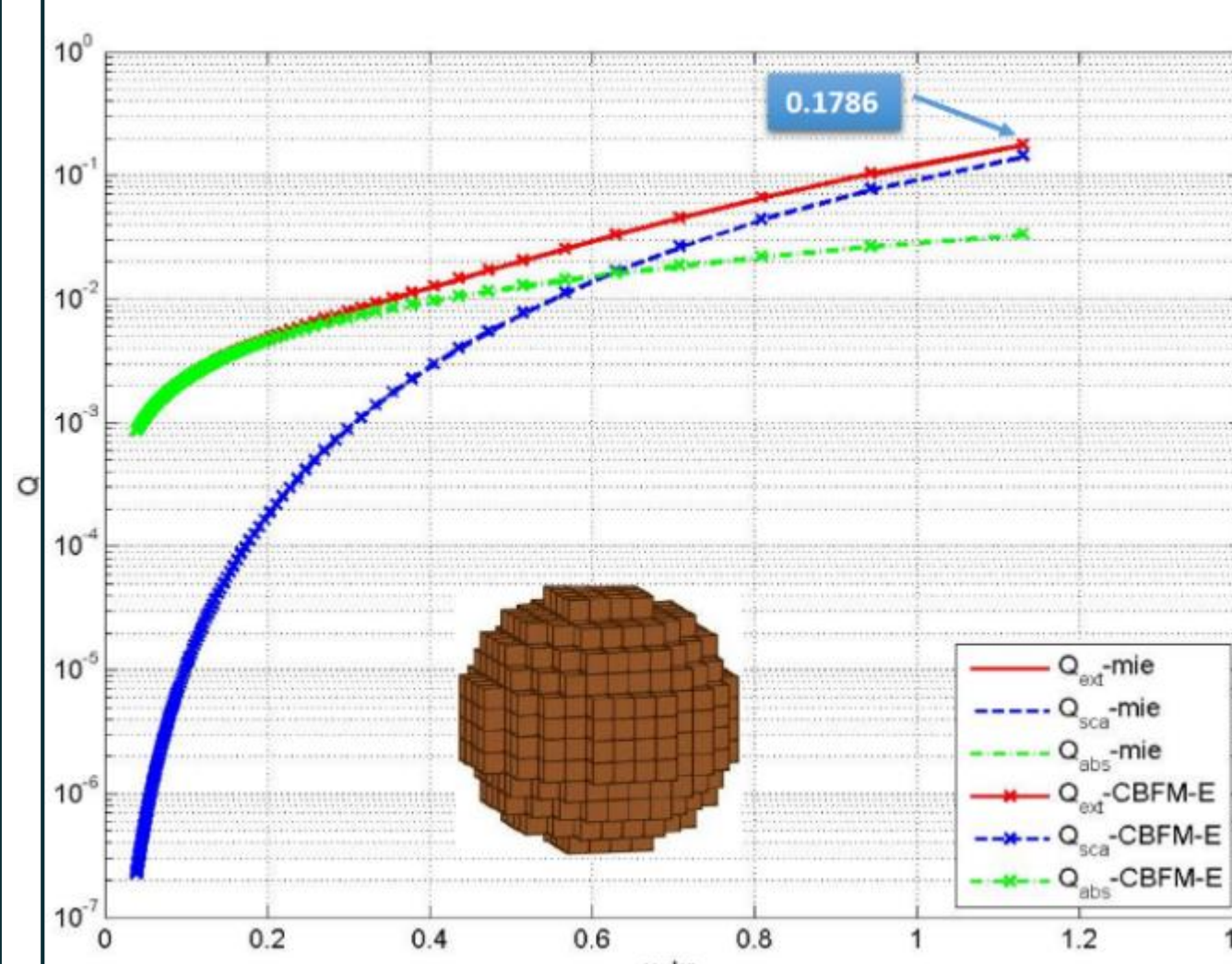$$\widetilde{E}_i^{(\theta,\varphi)} = \frac{E_i^{ref,(\theta,\varphi)}}{Z_{ii}}$$

2. Use of the ACA to speed-up the generation of Z^c

$$Z_{i,j}^c \approx \langle C^{(i)t}, \widetilde{Z}_{i,j}^{MoM} C^{(j)} \rangle$$

where $\quad \widetilde{Z}_{i,j}^{MoM} = U_i^{3N_i \times r} V_j^{r \times 3N_j}$

and **r** (effective rank of $Z_{i,j}^{MoM}$) **<< 3 N_i and 3 N_j**

III – Numerical results :

We compute the **extinction, absorption, scattering and back-scattering efficiency factors $Q_{ext} = C_{ext}/\pi a^2$, $Q_{abs} = C_{abs}/\pi a^2$, $Q_{scat}=C_{scat}/\pi a^2$** and **$Q_{bks}=C_{bks}/\pi a^2$** as functions of x = ka=2πa/λ, and compares the results with those derived from the Mie series (spherical particle) and with those calculated using Discrete Dipole Approximation as coded in DDSCAT 7.1.
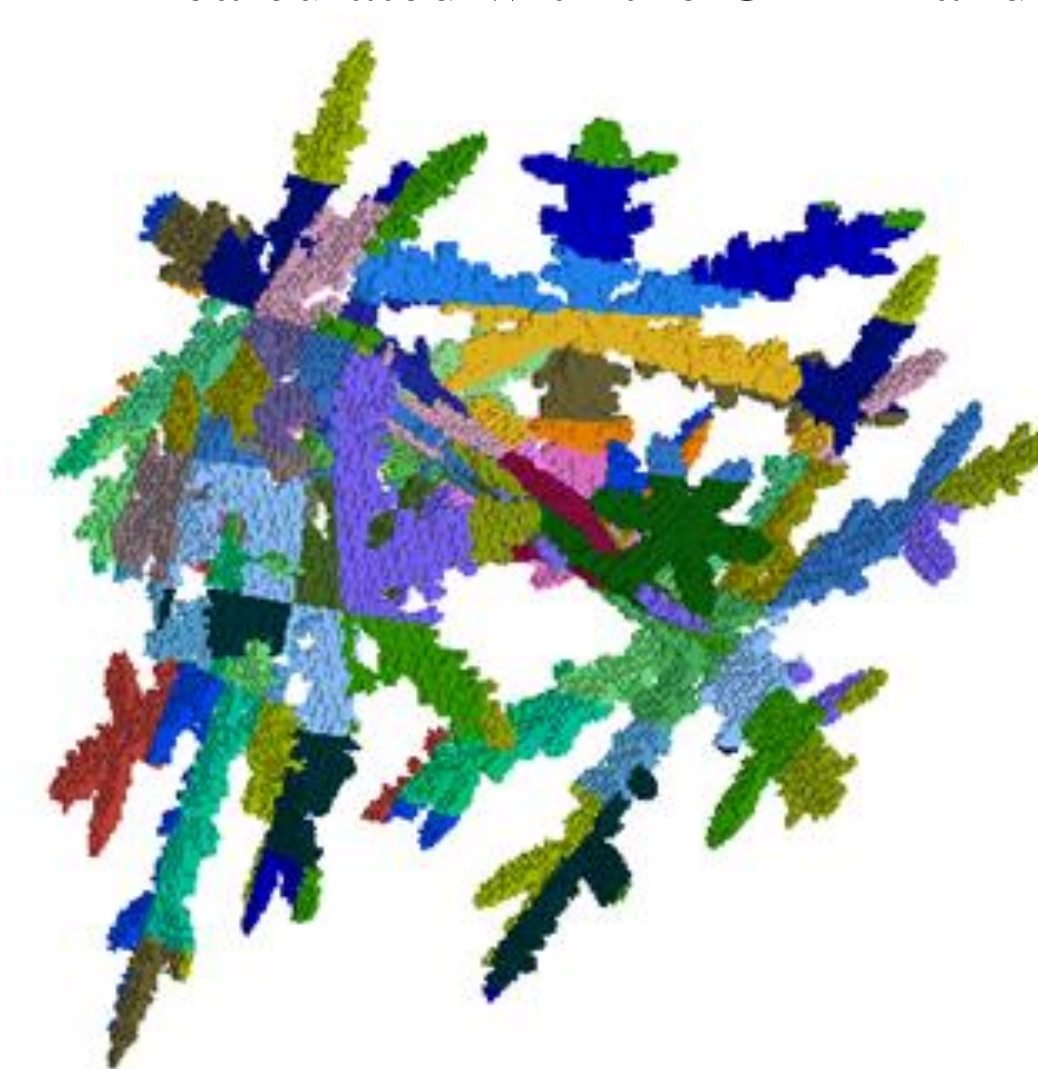
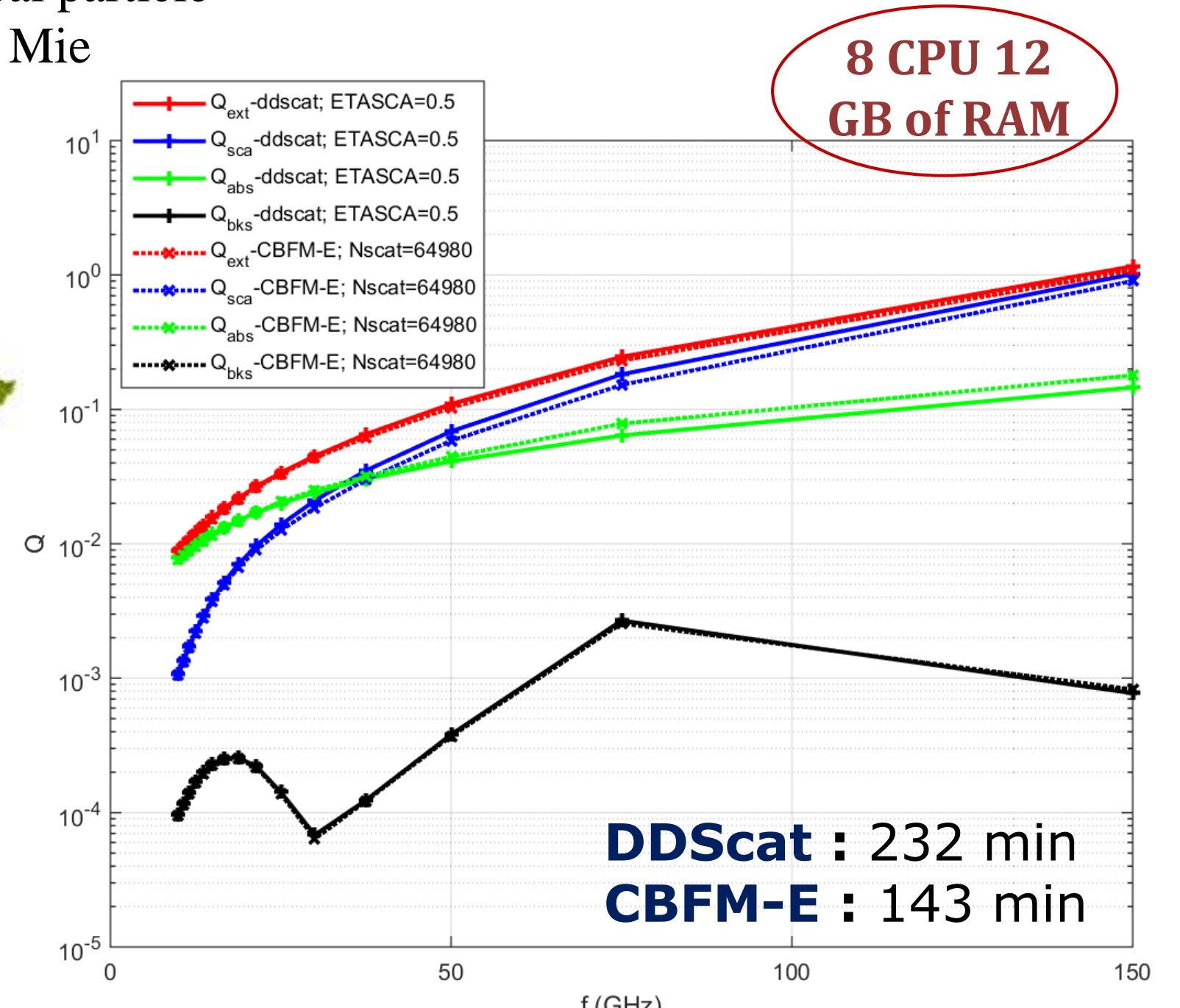C_{ext}, C_{scat} and C_{bks} are derived from the **scattering matrix S** :

$$C_{ext} = \frac{4\pi}{k^2} Re\{S(0)\}; \quad C_{bks} = \frac{4\pi}{k^2} |S(N_\theta)|^2$$

$$C_{scat} = \int_0^{2\pi}\int_0^{\pi} \frac{S(\theta,\phi)}{k^2}\sin(\theta)\,d\theta\,d\phi$$

$$C_{abs} = C_{ext} - C_{scat}$$

The scattering properties of a spherical particle calculated with the CBFM and Mie

8 CPU 12 GB of RAM

Nb$_c$ = 140896 cells

DDScat : 232 min
CBFM-E : 143 min

The scattering properties of a complex-shaped particle of effective radius a_p=1.614 mm (max. dim. = 11.45 mm) calculated using the MoM/CBFM-E and DDScat

References : [1] Kuo, K. S., Olson, W. S., Johnson, B. T., Grecu, M., Tian, L., Clune, T. L., … & Meneghini, R. (2016). The Microwave Radiative Properties of Falling Snow Derived from Nonspherical Ice Particle Models. Part I: An Extensive Database of Simulated Pristine Crystals and Aggregate Particles, and Their Scattering Properties. Journal of Applied Meteorology and Climatology, 55(3), 691-708. [2] E. Lucente, G. Tiberi, A. Monorchio, and R. Mittra, "An iteration-free MoM Approach Based on Excitation Independent Characteristic Basis Functions for Solving Large Multiscale Electromagnetic Scattering Problems", IEEE Trans. Antennas Propag., Vol. 56, no. 4, pp.999-1007, Apr. 2008.

EB-9

Connecting Observed Trends in Ozone Precursor Emissions to Methane and Ozone Radiative Forcing

Thomas W. Walker (JPL, 329G), Kevin W. Bowman (JPL, 329G), Kazuyuki Miyazaki (Japan Agency for Marine-Earth Science and Technology)
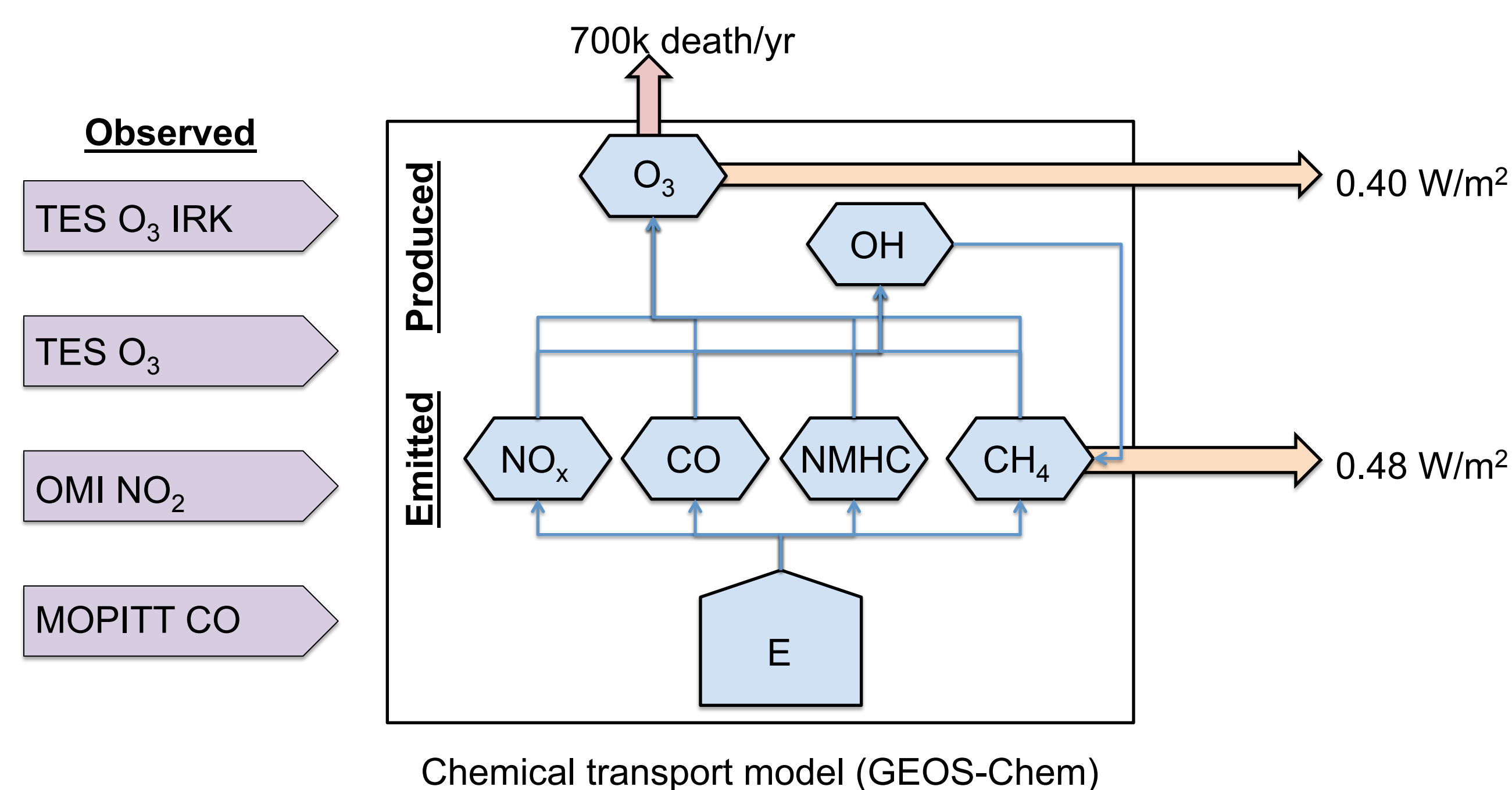
- We have established a spatially explicit relationship attributing methane radiative forcing (RF) to changes in precursor emissions.
- Top 10% of locations with positive (negative) net methane RF contribute 50% (60%) of the total positive (negative) RF under RCP 6.0.
- Preliminary validation of mass balance inversion of decadal NO_x emissions trend from OMI NO_2 shows no global trend from 2005-2015.

MOTIVATION

- Methane (CH_4) and ozone (O_3) are second and third most significant gases in terms of radiative forcing (RF).
- Atmospheric abundance and lifetime of CH_4 and O_3 depend critically on local chemical environment.
- Local chemical environment is modified by short-lived precursor gases (e.g., NO_2, CO), whose emission controls are primarily driven by air quality concerns.
- Decadal satellite records of precursor observations enable the calculation of trends.

METHOD

- We leverage A-Train observations of key short-lived gases (OMI NO_2, MOPITT CO, and TES O_3) between 2005-2015 to calculate decadal emissions trends of NO_x and CO.
- We use adjoint sensitivity analysis and TES instantaneous radiative kernels (IRKs) to determine the relationship between RF and precursor emissions changes.
- We employ a chemical transport model and data assimilation to attribute RF to emissions at regional scales (2^ox2.5^o).

700k death/yr

Observed

TES O_3 IRK

TES O_3

OMI NO_2

MOPITT CO

Produced: O_3 , OH — 0.40 W/m^2

Emitted: NO_x , CO , $NMHC$, CH_4 — 0.48 W/m^2

E

Chemical transport model (GEOS-Chem)

PROJECT STATUS

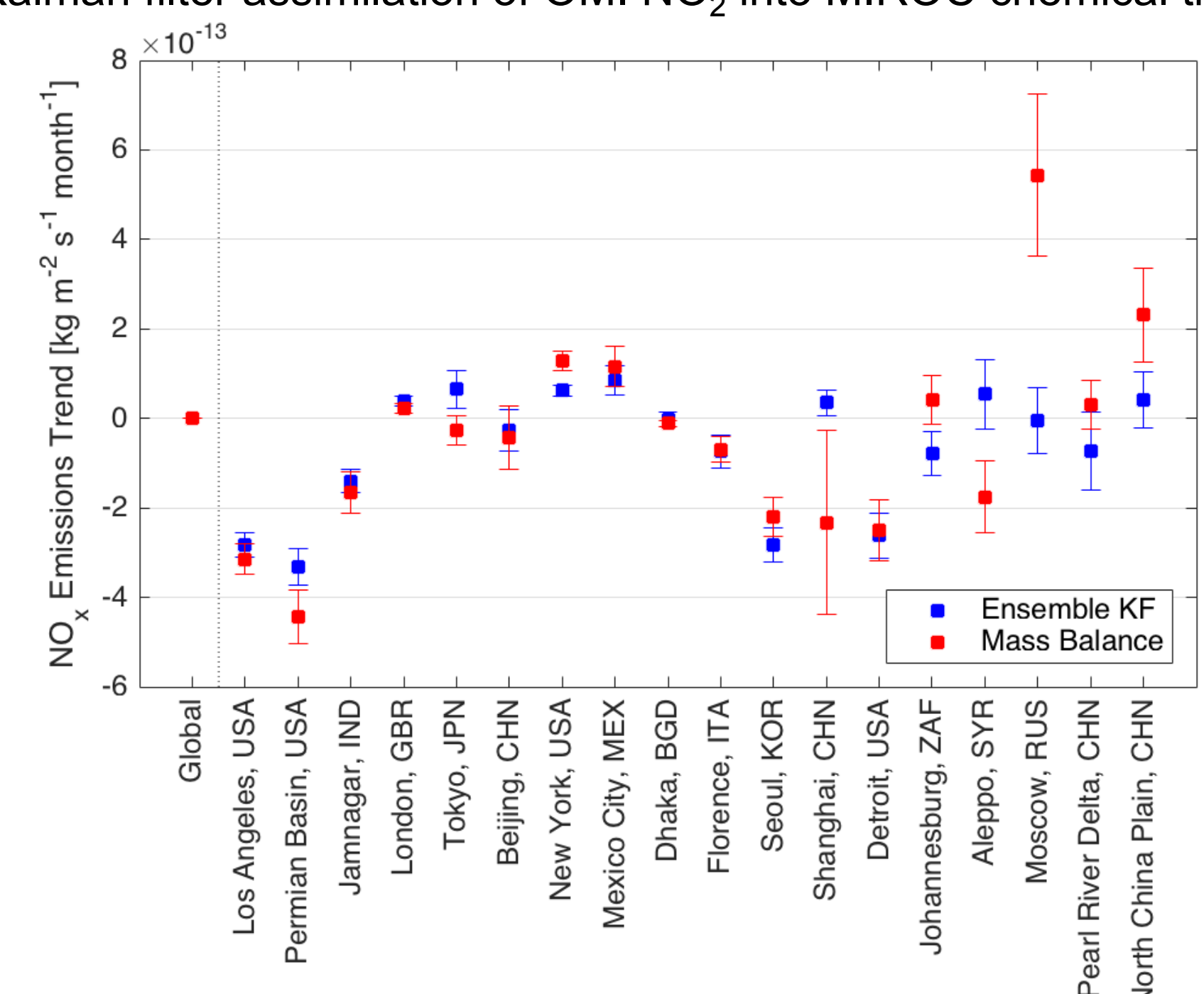| Relationship	Data	Method	Status
Sensitivity of CH_4 RF to precursor emissions	GEOS-Chem adjoint	Adjoint sensitivity calculation	Complete
Sensitivity of O_3 RF to precursor emissions	TES O_3 IRK	Adjoint sensitivity calculation	In Progress
Trend in NO_x emissions	OMI NO_2	Mass balance inversion	Validation
Trend in CO emissions	MOPITT CO	4D-Var inversion	In Progress
Constraint on background chemical state	TES O_3	3D-Var inversion	Validation

RESULTS: ATTRIBUTION OF CH_4 RF

- Adjoint sensitivity of CH_4 loss rates defines relationship between CH_4 RF and grid scale changes in emissions.
- Apply Representative Concentration Pathway (RCP) 6.0 to examine potential impact of future emissions on CH_4 RF.
- Spatially heterogeneous RF depends on emissions magnitude and location.
- Top 10% of locations with positive (negative) RF account for 50% (60%) of positive (negative) RF.

RF from NOx

RF from CO + NMHC

RF from CH4

RF total
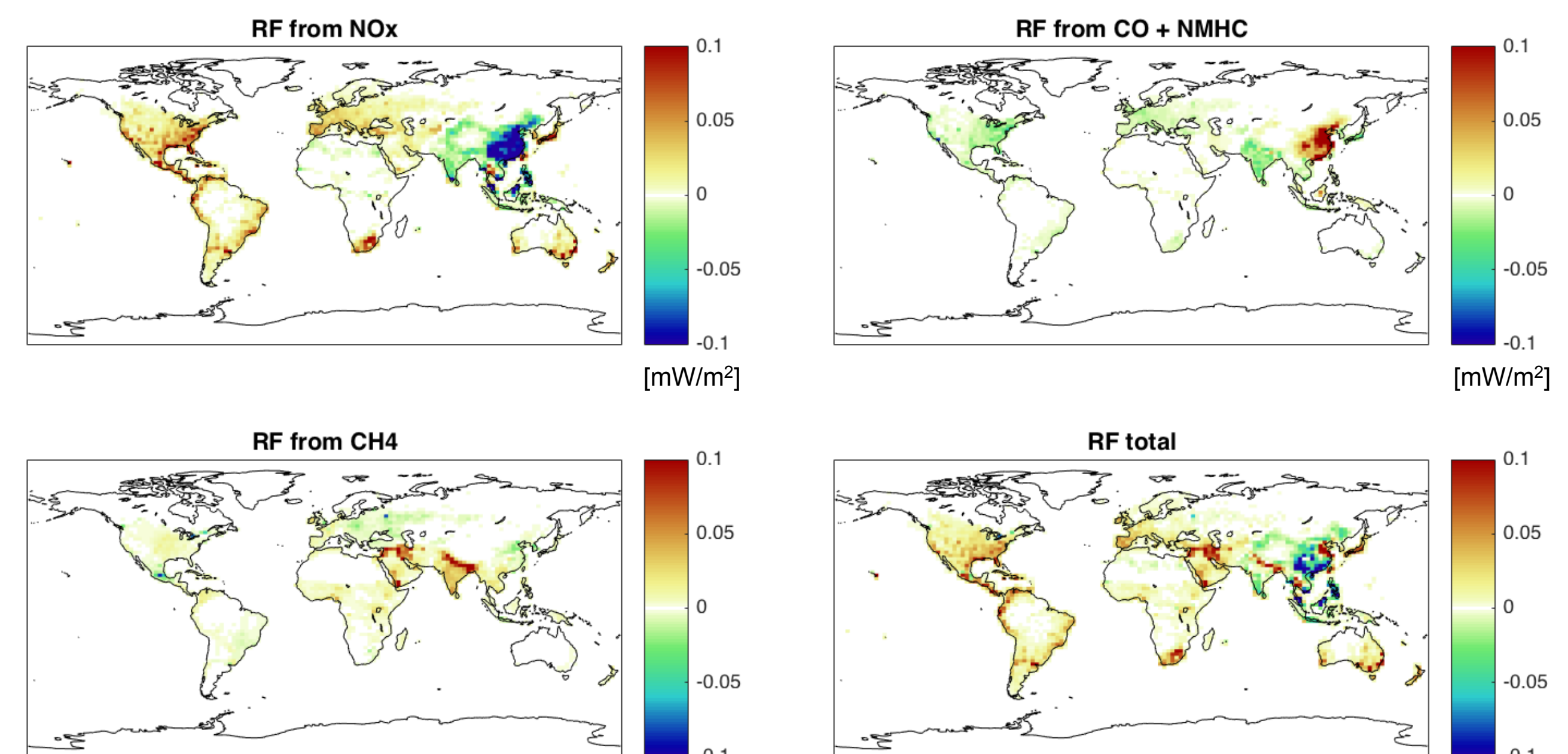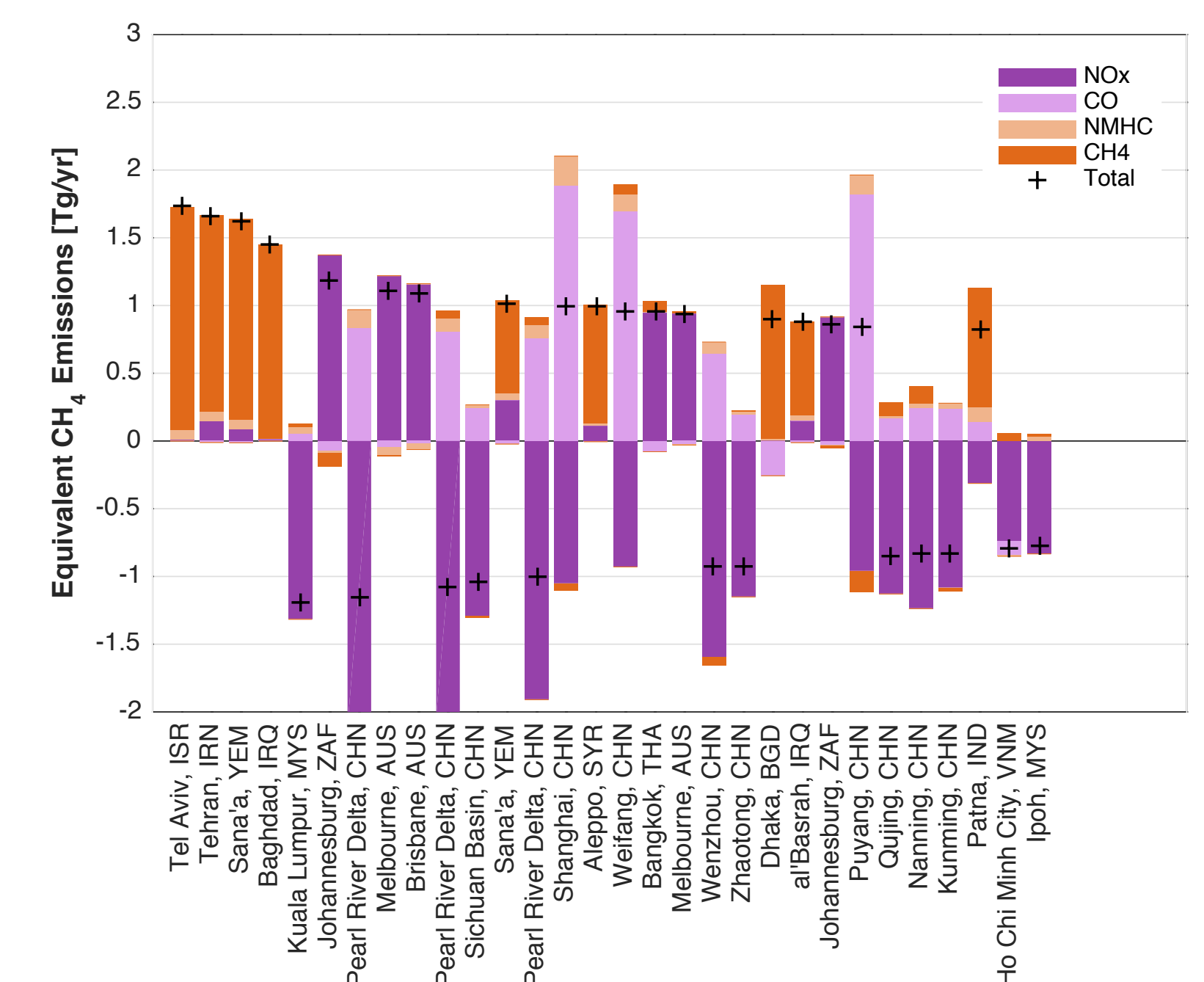
RESULTS: INVERSION OF NO_X EMISSIONS

- Mass balance inversion of NO_x emissions from OMI NO_2 to get decadal trend from 2005-2015.
- Global mean trend not significantly different from zero.
- Spatial pattern of trends gives reasonable agreement with independent estimate using ensemble Kalman filter assimilation of OMI NO_2 into MIROC chemical transport model.

National Aeronautics and Space Administration

Jet Propulsion Laboratory
California Institute of Technology
Pasadena, California

www.nasa.gov

Copyright 2016. All rights reserved.

Poster No. EB-10

Analysis of Tropospheric Ozone Long-term Lidar and Surface Measurements at JPL-Table Mountain Facility site, CA

Author: Maria Jose Granados-Muñoz (329H)
Thierry Leblanc (329H)

INTRODUCTION

Tropospheric ozone (O_3) is a greenhouse gas and air pollutant that affects climate, tropospheric chemistry and air quality. O_3 is affected by large spatial and temporal variability, due to large heterogeneity and variability of the sources, different chemical processes affecting the formation and depletion of O_3 and its variable lifetime in the troposphere (Cooper et al., 2014). Global and long-term monitoring systems and synergetic approaches combining observations and models are crucial to fully understand this variability and O_3 trends in the troposphere (Cooper et al., 2015; Lin et al., 2015).

At Table Mountain Facility (TMF, 34.4° N, 117.7° W, 2285 m), routine tropospheric O_3 measurements have been performed with a DIAL system (McDermid et al., 2002) from 2000 up to date as part of NDACC and TOLNet networks. A comprehensive analysis of the 16-year dataset together with the 2.5-year surface data is presented here to contribute to the understanding of tropospheric O_3 in the Southwestern US.
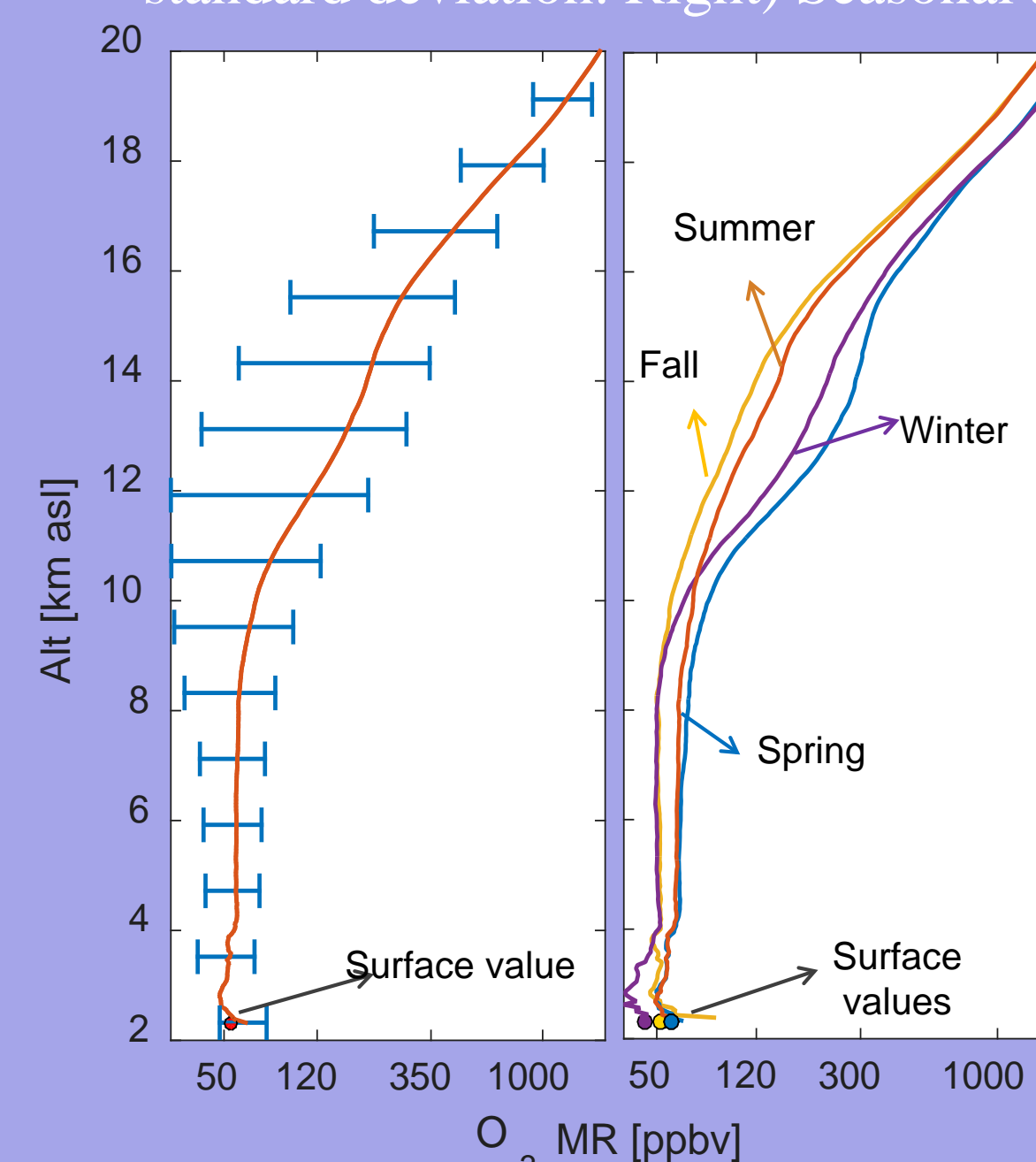
SURFACE DATA
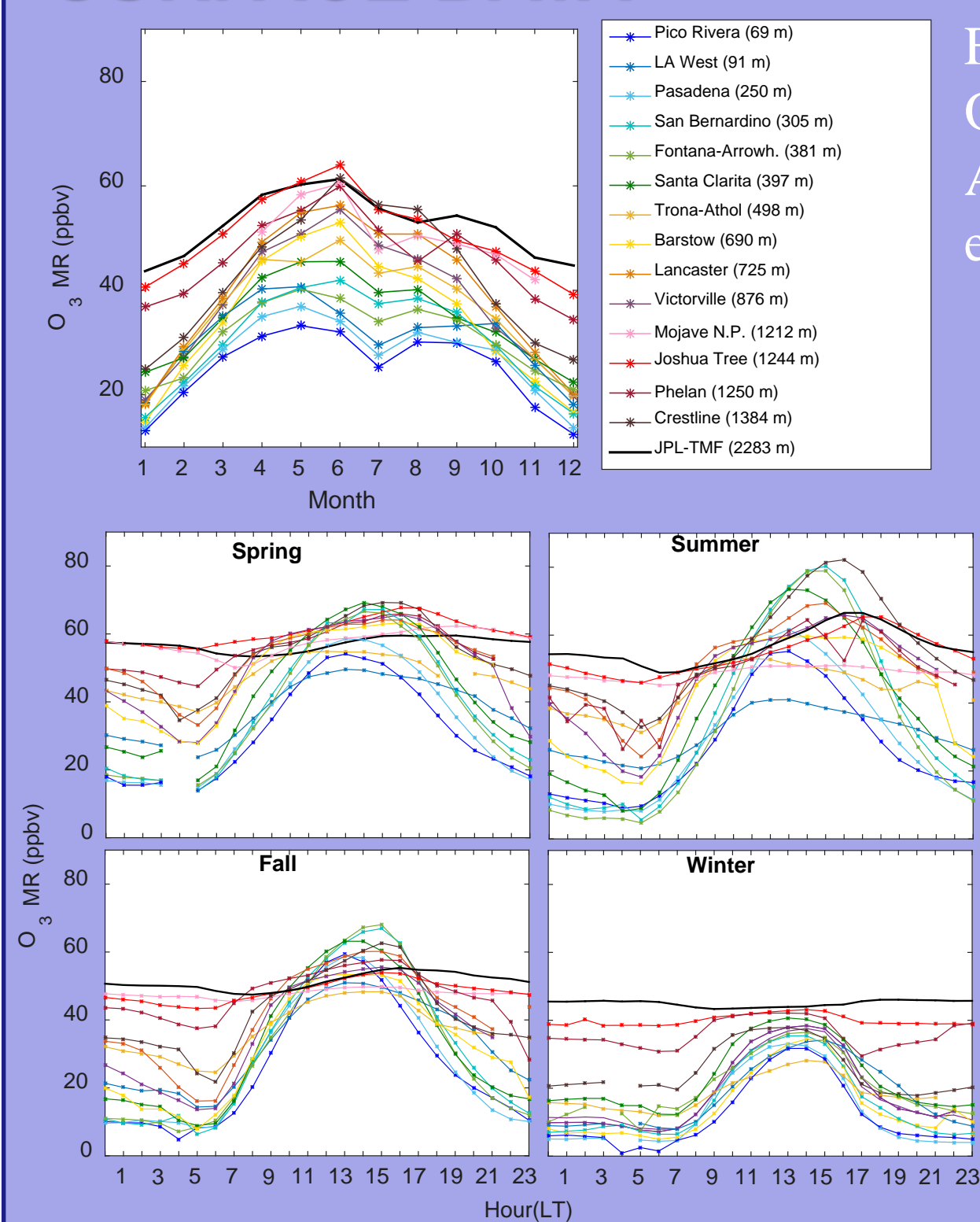
Fig.: top) Surface O_3 seasonal cycle and bottom) surface O_3 daily cycle for the four seasons at TMF and nearby ARB stations. The numbers in parentheses are the sites elevations.

- Surface O_3 annual cycle: minima in winter and maxima in spring-summer.
- Frequent NAAQS exceedance days (8hMDA >70 ppbv) in spring and summer.
- Second local maximum in Fall.
- Daily and annual surface O_3 cycles at TMF present very low variability and high average values (55 ppbv), typical of high-elevation remote sites with no urban influence (TMF elevation: 2285 m)
- O_3 increases with altitude and distance to urban sources → up to 30 ppbv difference between Pico Rivera and TMF sites.

LIDAR DATA

Fig: Left) Average O_3 MR profile at TMF for 2000-2015. Horizontal bars are the standard deviation. Right) Seasonal average O_3 MR profiles

- Same seasonal cycle observed in the troposphere with the lidar and the surface.
- Average tropospheric O_3 mixing ratio (MR) is 55 ppbv at the surface and between 4 and 8 km, indicating free tropospheric O_3 is measured at the surface at TMF.
- O_3 MR increase with altitude, with strong gradients in the UTLS region (10-16 km) and near the surface.
- O_3 large variability in the UTLS region, with mixing of stratospheric and tropospheric O_3, associated to variability of the tropopause height.
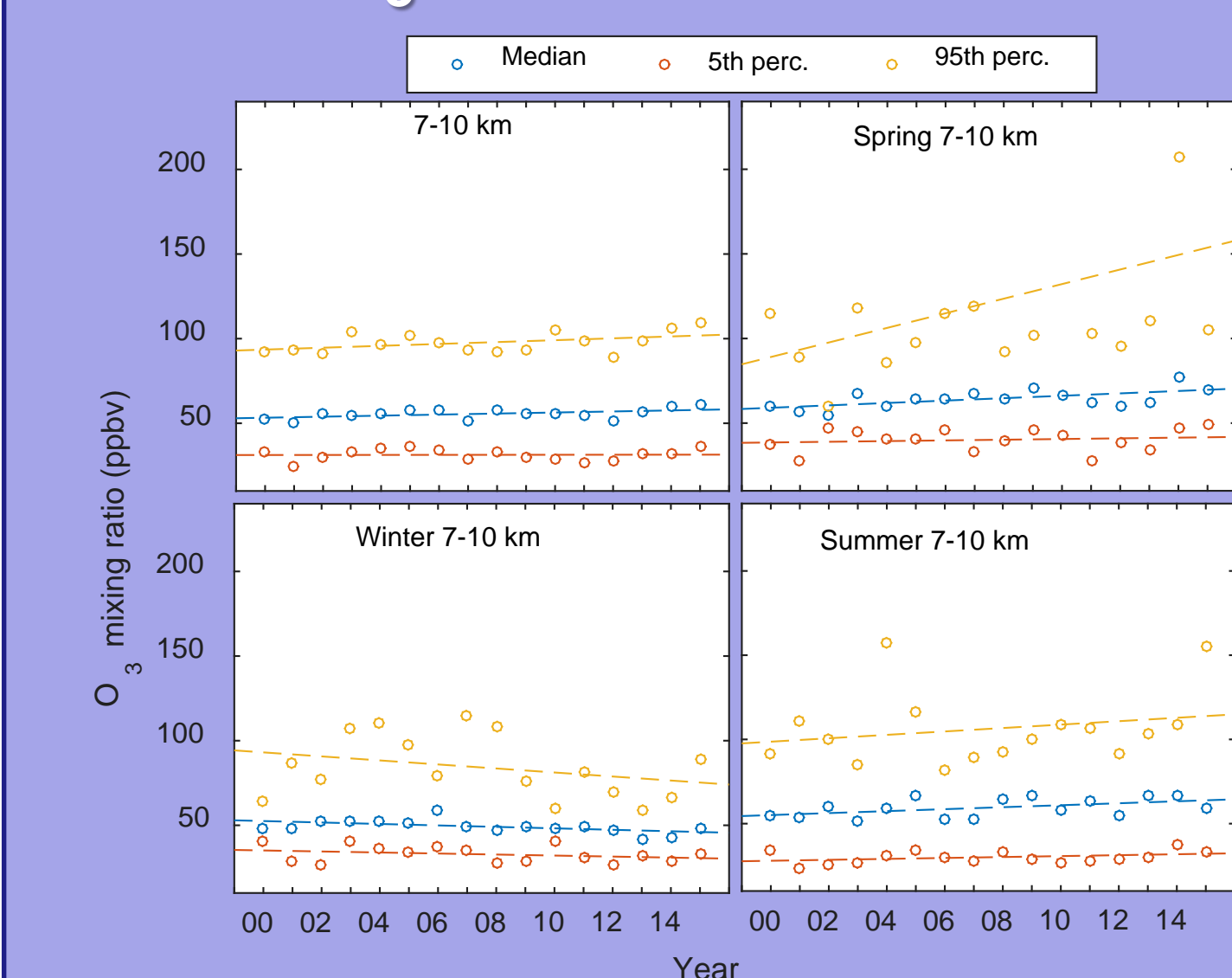
TROP. O_3 TRENDS

Fig: Left) Median, 5th, and 95th percentile values per year and for different seasons and altitudes. Dotted lines represent the linear fit for each dataset. Slopes of the fit were used to retrieve the trends.

Significant trends observed at TMF in 2000-2015 in the troposphere (7-10 km)

↑ Overall increasing trend (0.31±0.15 ppbv/year, p-Value = 0.06)

↑ Increasing O_3 in spring (0.71±0.25, p-Value = 0.01) and summer (0.58±0.28, p-Value = 0.05)

↓ Decreasing O_3 in winter -0.43±0.18 ppbv/year (p-Value = 0.03)

12-day back trajectories retrieved with HYSPLIT model reveal five "ozone source regions" reaching TMF:

1-Stratosphere (Strat)

2- Asian Boundary Layer (ABL)

3- Asian Free Troposphere (AFT)

4- Pacific Ocean (Pac)

5- Central America (Cen Am)

Large O_3 values for AFT air masses, especially in summer. Most frequent Asian influence observed in spring.

Enhanced values in summer for Cen Am air masses (related to lightning-induced O_3 local production during the North American monsoon)
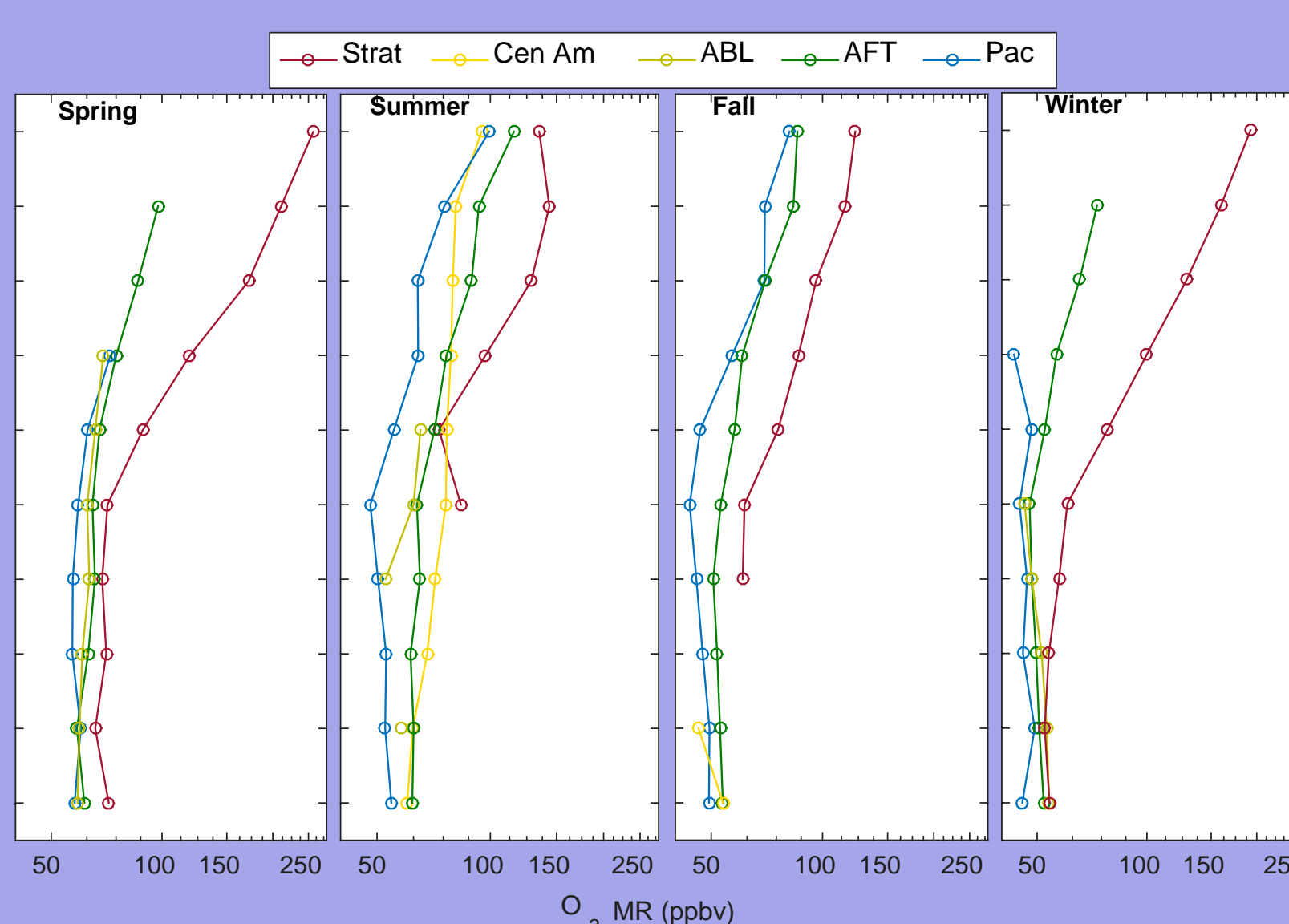
Lowest O_3 values associated to Pacific or "background region"

Largest O_3 values associated to Strat air masses. Most frequent Strat influence in winter/spring, reaching down to 5 km

Fig: 2000-2015 Composite profiles of O_3 MR median values associated to the different origin regions for the four seasons.

Table: Frequency of the air masses (in %) arriving at different altitudes above TMF from the source regions

	Strat	Cent Am	ABL	AFT	Pac
10 km	18 %	6 %	6 %	40 %	21 %
8 km	8 %	7 %	9 %	39 %	22 %
6 km	5 %	9 %	9 %	34 %	23 %

O_3 SOURCES

Fig.: Average O_3 MR profile for cases of tropopause folds (DT) and non-folds (ST) above TMF in spring and winter.

- Trop. folds entrain stratospheric O_3 into the troposphere
- 1-km vertical resolution MERRA Temperature profiles used to identify tropopause folds
- Frequent trop. folds above TMF, affecting 27% of the analyzed lidar data
- O_3 dual vertical structure in the UTLS region:
  - < lower-than-averaged values in the top half of the fold (~14-18 km).
  - >higher-than-averaged values in the bottom half (~12-14 km)
- Impact on lower troposphere, with higher ozone (+2 ppbv) at 4-6 km, influencing air quality.
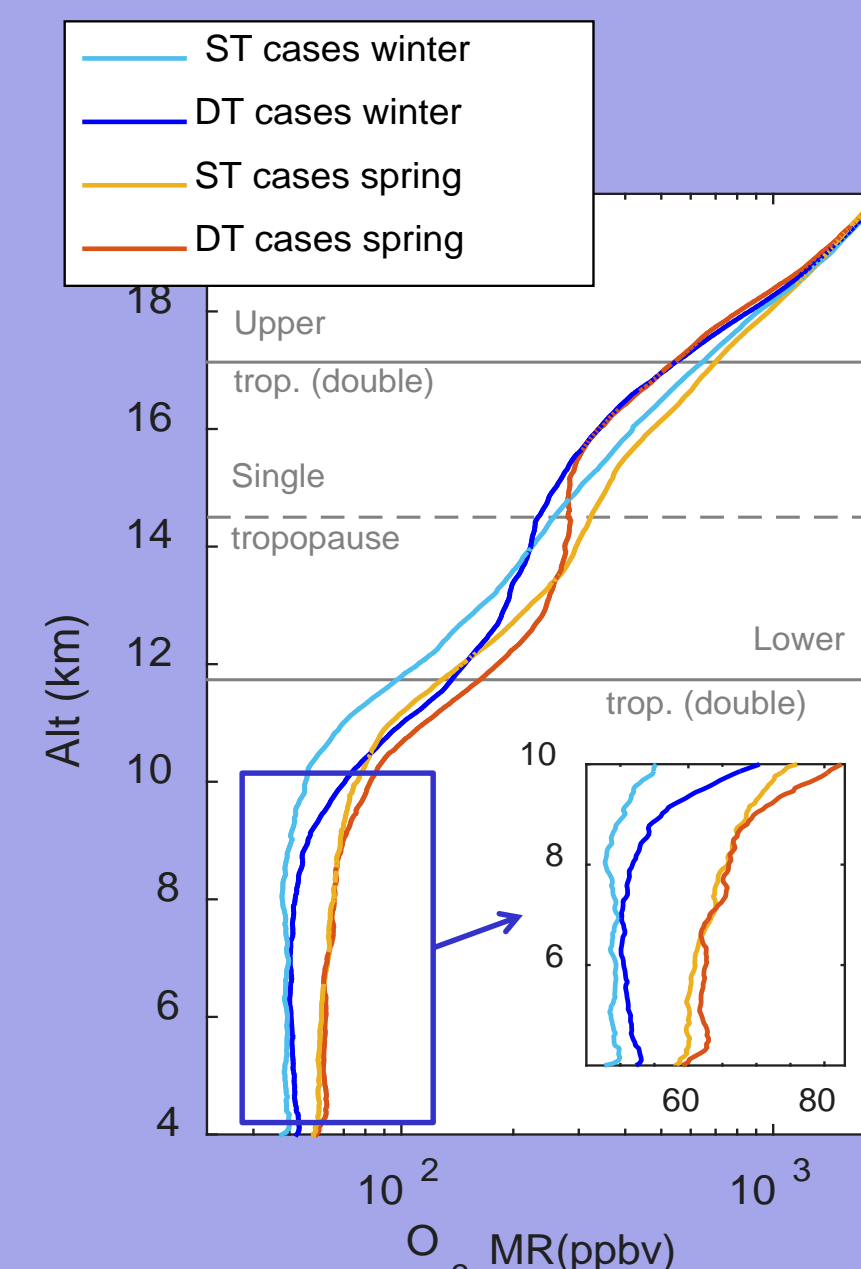
CONCLUSIONS

- Surface O_3 values and annual and diurnal variability at TMF is typical of high elevation remote sites measuring free trop. O_3 with no influence of urban pollution and the PBL cycle.
- Lidar 16-year dataset reveals significant increasing trends in the upper troposphere despite the decreasing emission in the US, probably related to O_3 transport from international sources and the stratosphere.
- Larger O_3 values obtained when air masses come from the stratosphere (mainly in winter and spring) and minimum values from the Pacific.

- Increased O_3 values due to Asian influence observed at TMF, mostly in spring and summer.
- Central America (associated to the monsoon circulation) in summer is an important O_3 source at TMF that has not been previously analyzed in detail in the Western US.
- Analysis of the tropopause folds (27% occurrence) reveals enhanced O_3 in the upper troposphere and decreased O_3 in the lower stratosphere. Increased O3 values (+2 ppbv) also observed near the surface.
- More details in Granados-Muñoz and Leblanc, ACP, 2016.

References:
Cooper et al., 2014 (Elem. Sci. Anth.)
Cooper et al., 2015 (Nature)
Lin et al., 2015 (GRL)
McDermid et al., 2002 (Appl. Opt.)
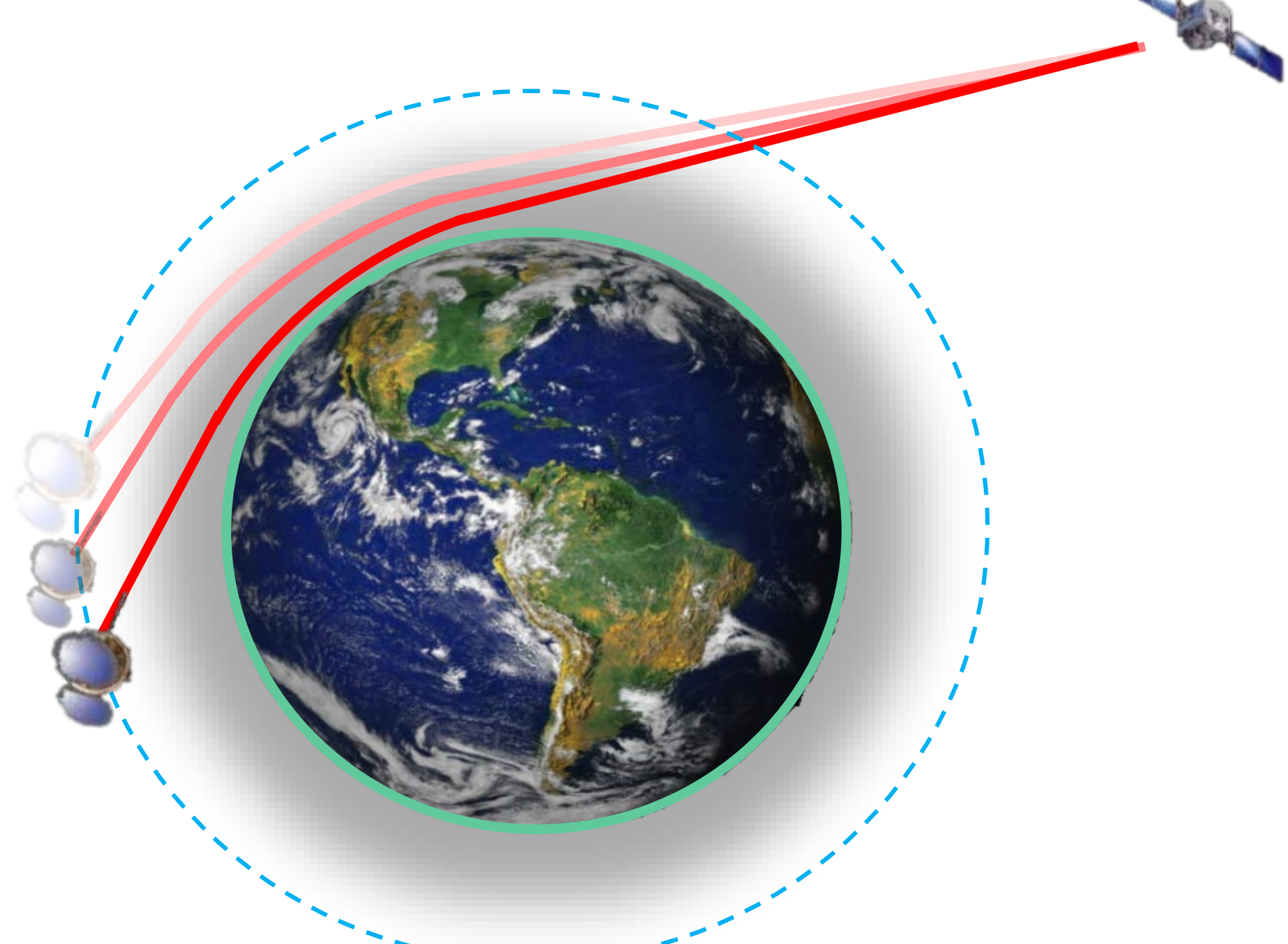Granados-Muñoz et al., 2016, (ACP)

Poster No. EB-11

Contact: mamunoz@jpl.nasa.gov

RO retrieval within the boundary layer with optimal estimation constrained by external measurements

Author: K.-N. Wang(3222), M. de la Torre Juarez(3222), C. O. Ao(335G), F. J. Turk(334H)

GPS Radio Occultation (GPS-RO)

- GPS-RO is an effective technique to profile atmospheric temperatures from accurate **refractivity measurements**.

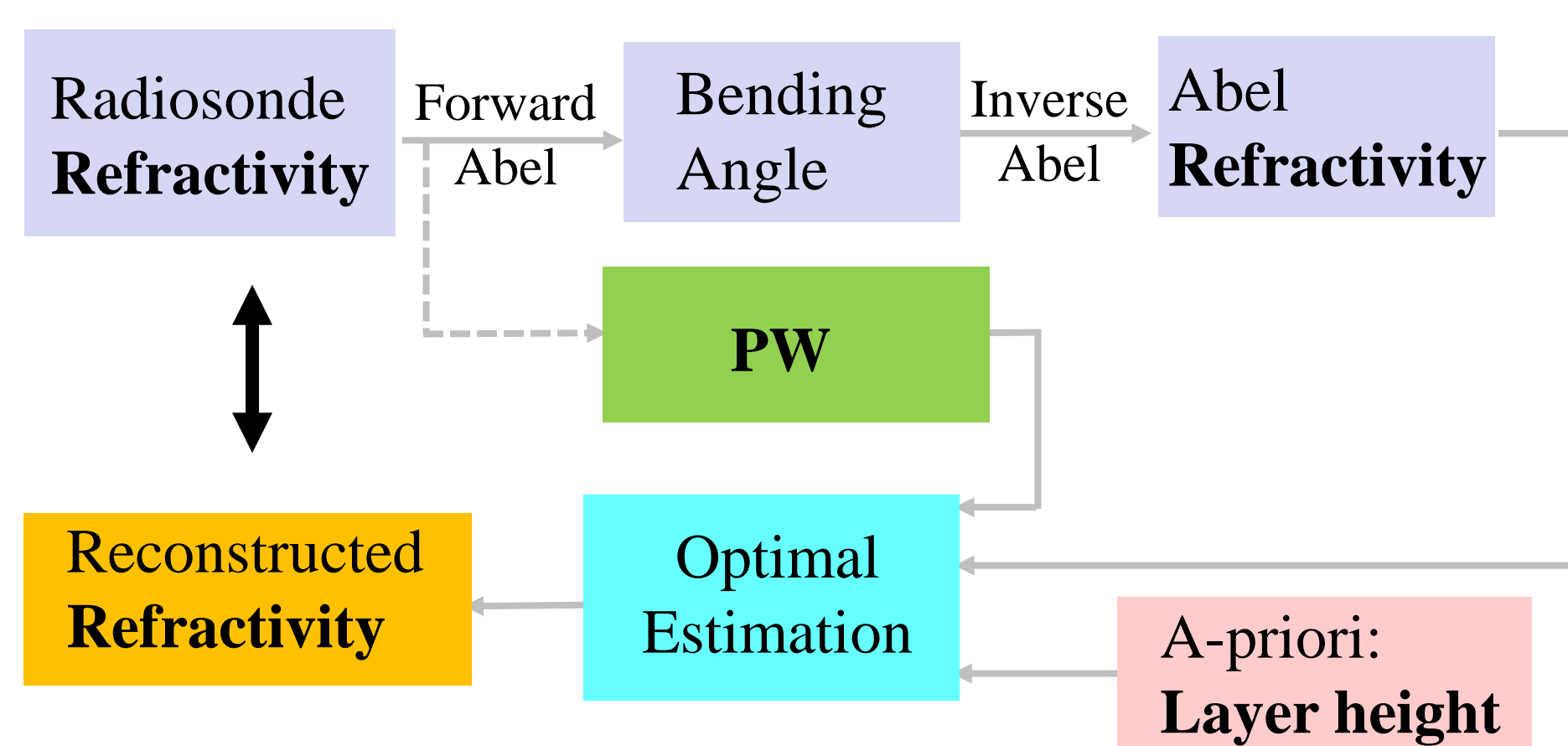## Negative Refractivity Bias (N-bias) caused by Ducting

- **Ducting** – the phenomenon causes the transmitting ray to follow the Earth's curvature due to a large negative refractivity gradient.
- The high resolution RO refractivity measurements will be **negatively biased** under ducting layers at the lower atmosphere.

h = 0.8 [km] in January   h = 0.8 [km] in July
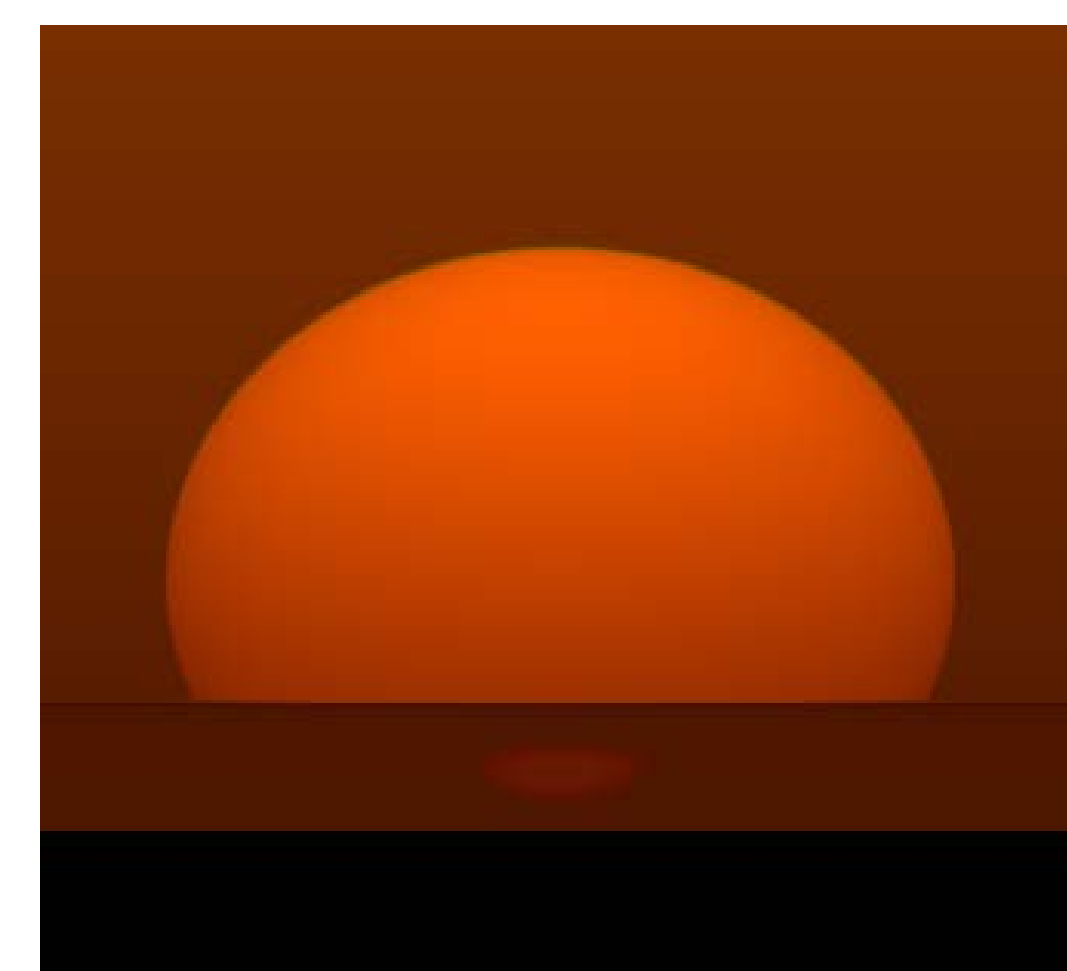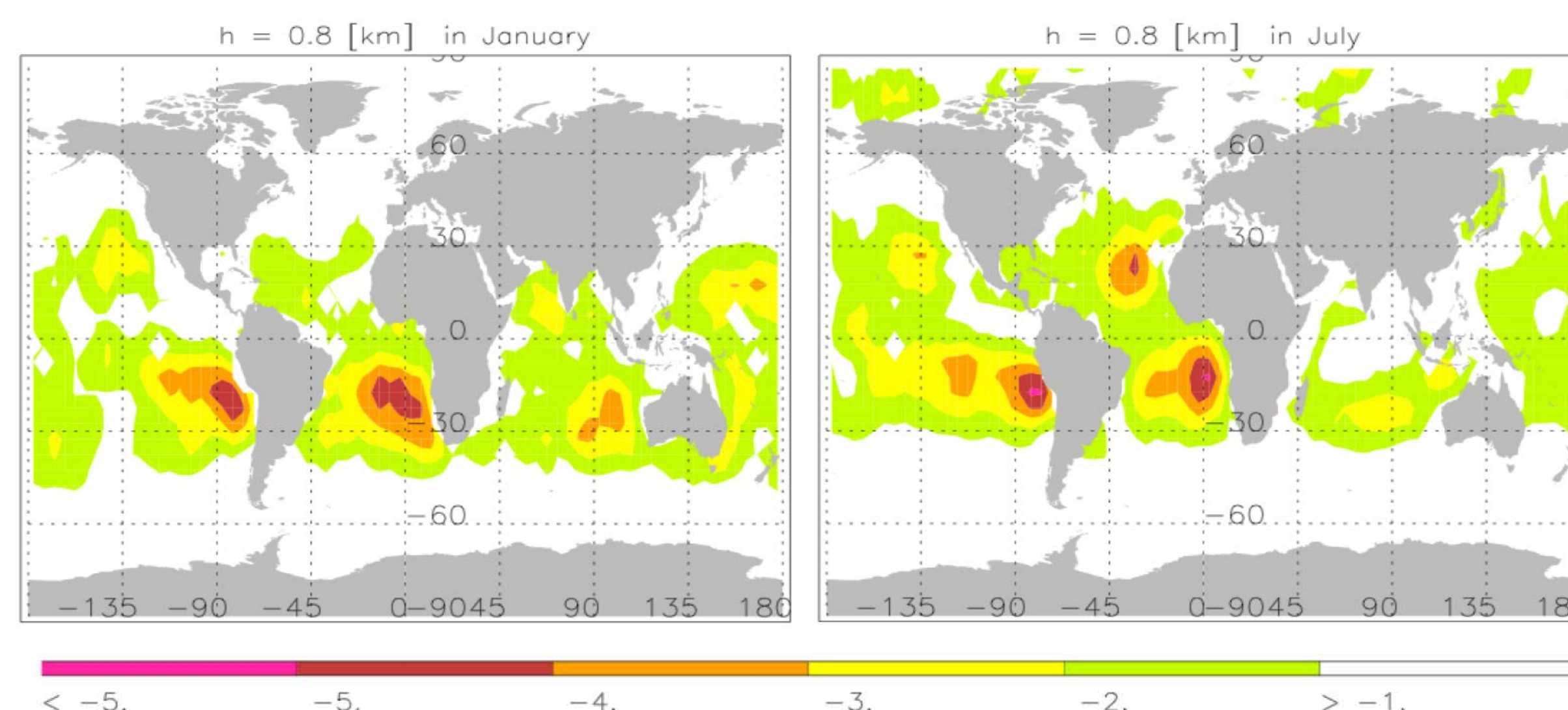
- A negative bias can be observed frequently in most cases **over the tropics and mid-latitudes**.

<F. Xie, 2010>

N-bias Correction Combining Optimal Estimation with AMSR-E Precipitable Water (PW) Measurements

Radiosonde **Refractivity** → Forward Abel → **Bending Angle** → Inverse Abel → Abel **Refractivity**

PW

Reconstructed **Refractivity** ← Optimal Estimation ← A-priori: **Layer height**

- The super-refraction (SR) caused by extreme refractivity gradients at ducting layers violates the uniqueness condition to perform traditional inverse Abel transform.
- A novel approach is shown to incorporate **optimization** into RO retrievals constrained by **precipitable water (PW)** measurements, which can be acquired by NASA remote sensing instruments such as AMSR-E and GPM.
- To choose the correct profile from the continuum of analytical solutions <F. Xie, 2006>, **optimal estimation** is used to select the one whose PW best matches the AMSR-E measurement.
- The cost function is the sum of two contributions: the RO calculated minus AMSR-E observed **PW** plus the difference in **layer height** from each optimization step to the a-priori. PW value can be acquired by integrating water vapor pressure with ECMWF temperature profiles.
- The results strongly suggest that this new approach can reduce the negative refractivity bias under the ducting layer and refine boundary layer height.

4.7 km   4.3 km

2.3 km   431 km

3.8 km   616 km

< https://www.ssec.wisc.edu/datacenter/aqua/ >
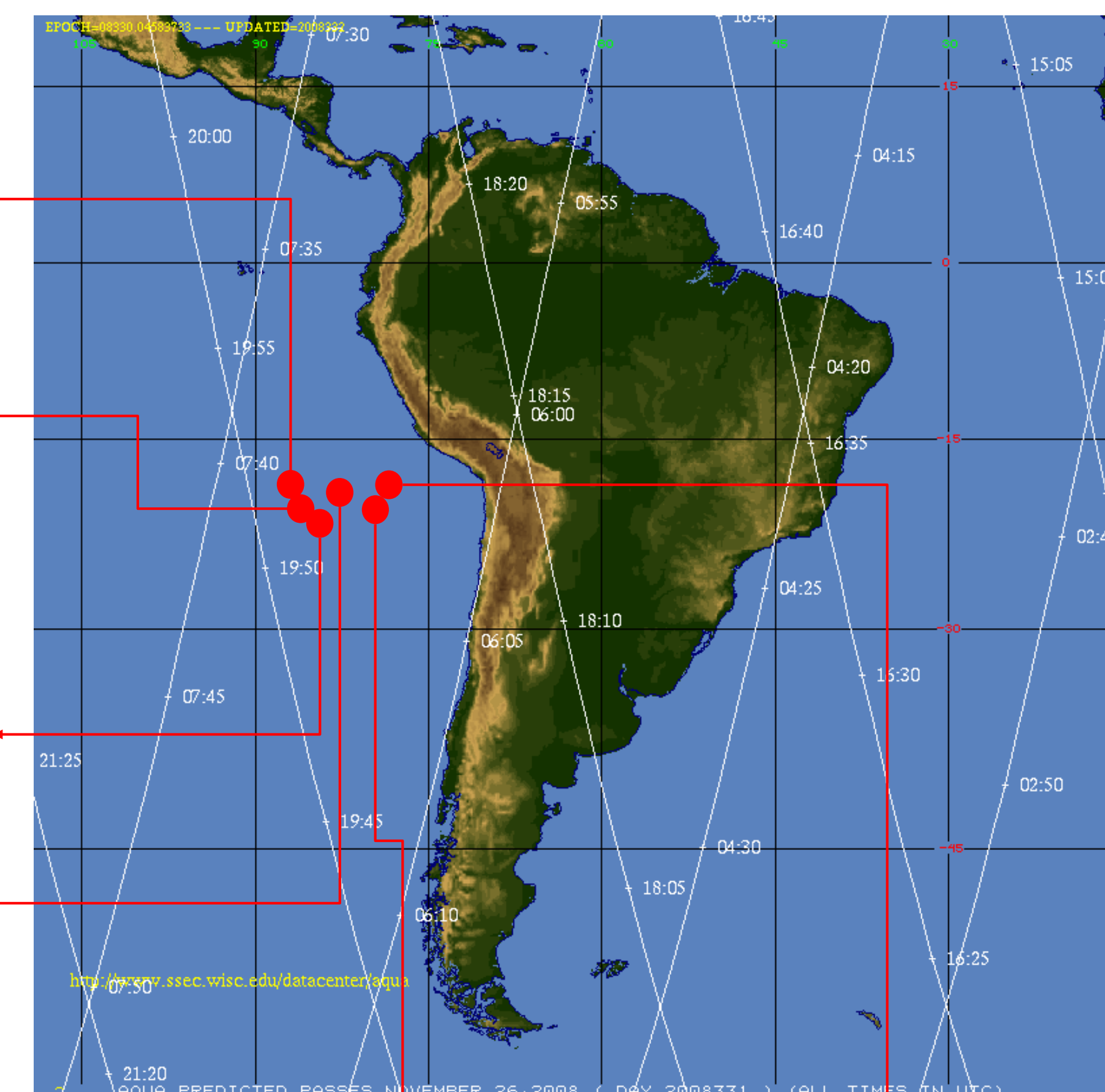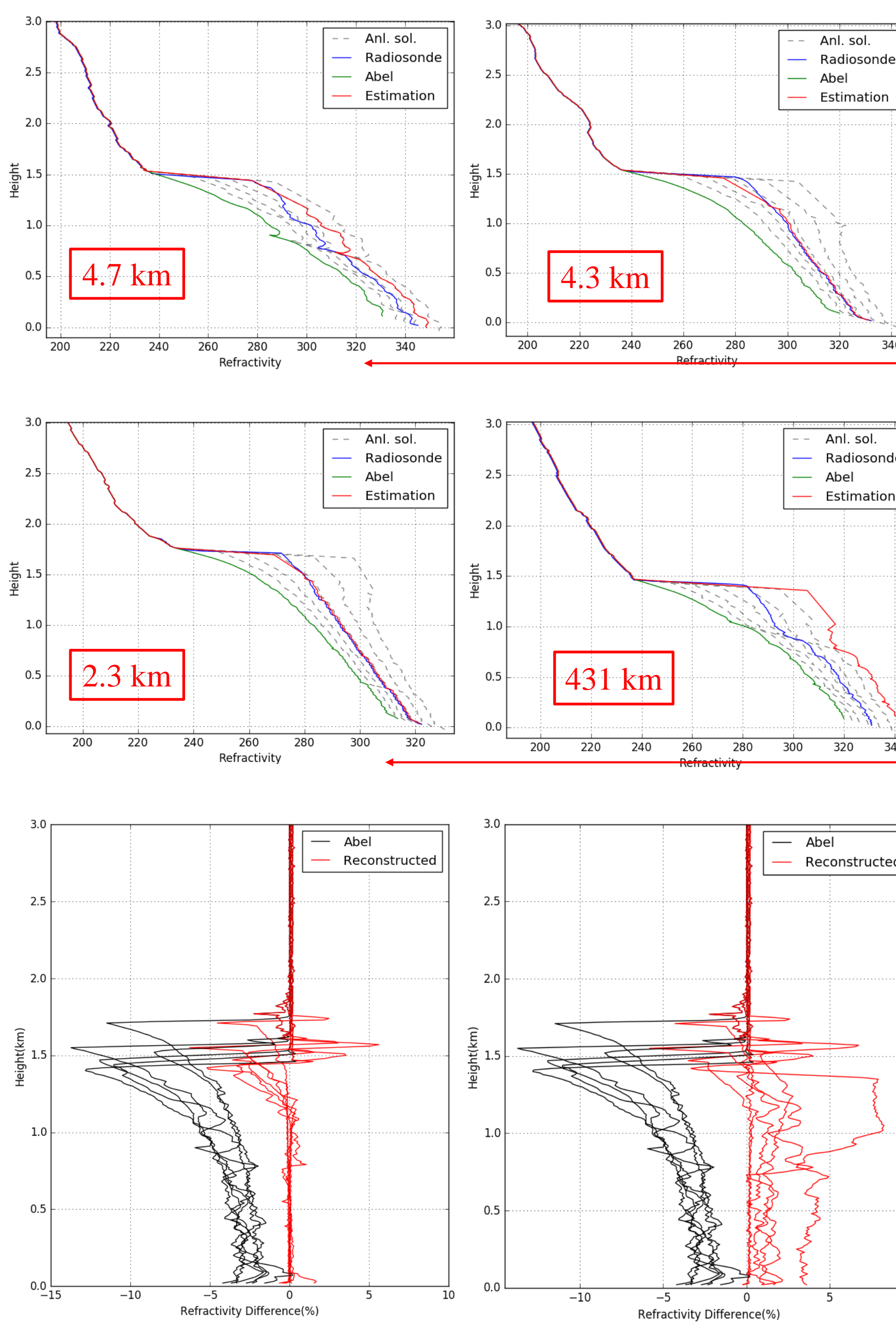
Validation with Real Data & Next Steps
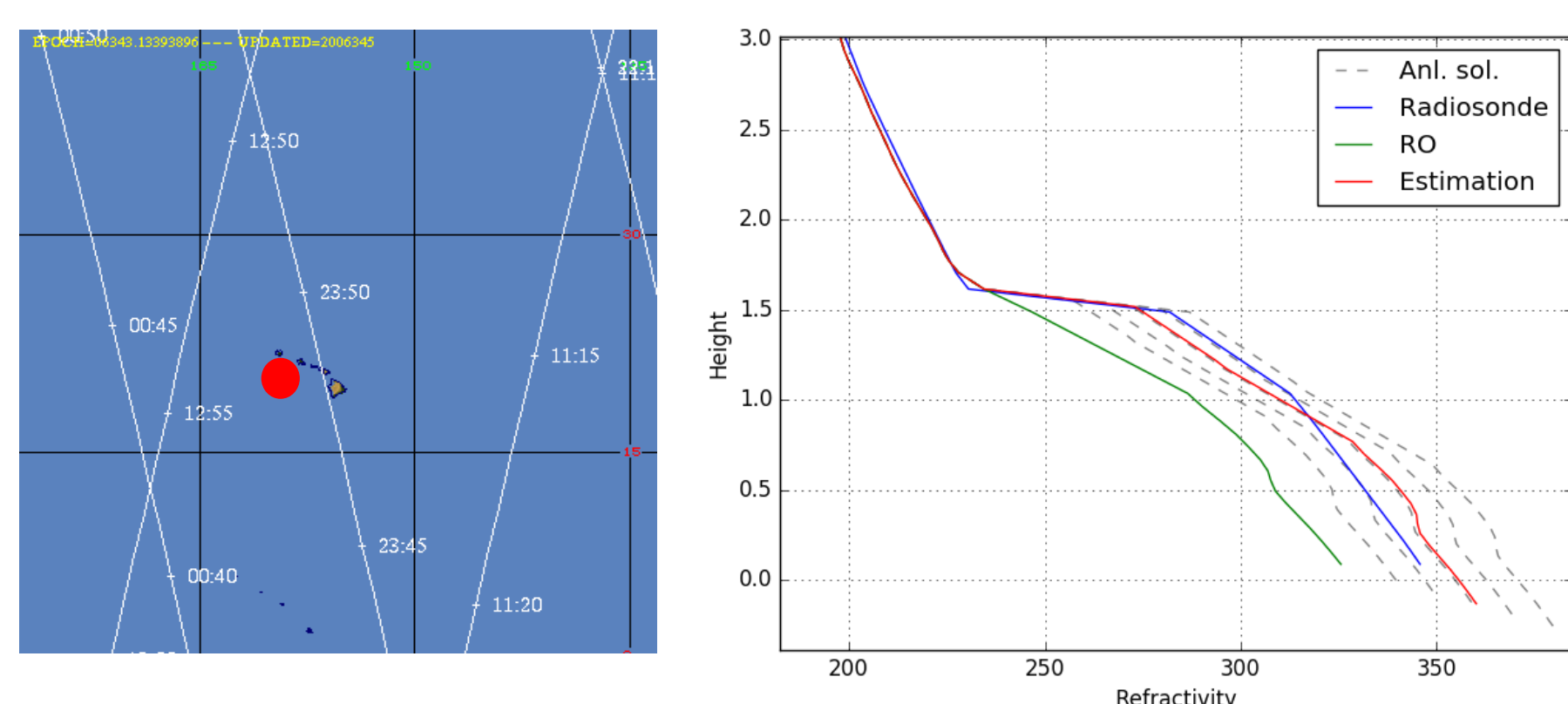
< Hawaii, 12/10/2006 12:11 UTC>

- The reconstruction method can be validated by actual GPS-RO signals and measured PW data from AMSR-E.

- The ECMWF model will be tested as a potential PW source for refractivity profile reconstruction.
- The Time duration of the RO signal amplitude "drop" may contain ducting layer thickness information for **self-correcting** refractivity retrievals.
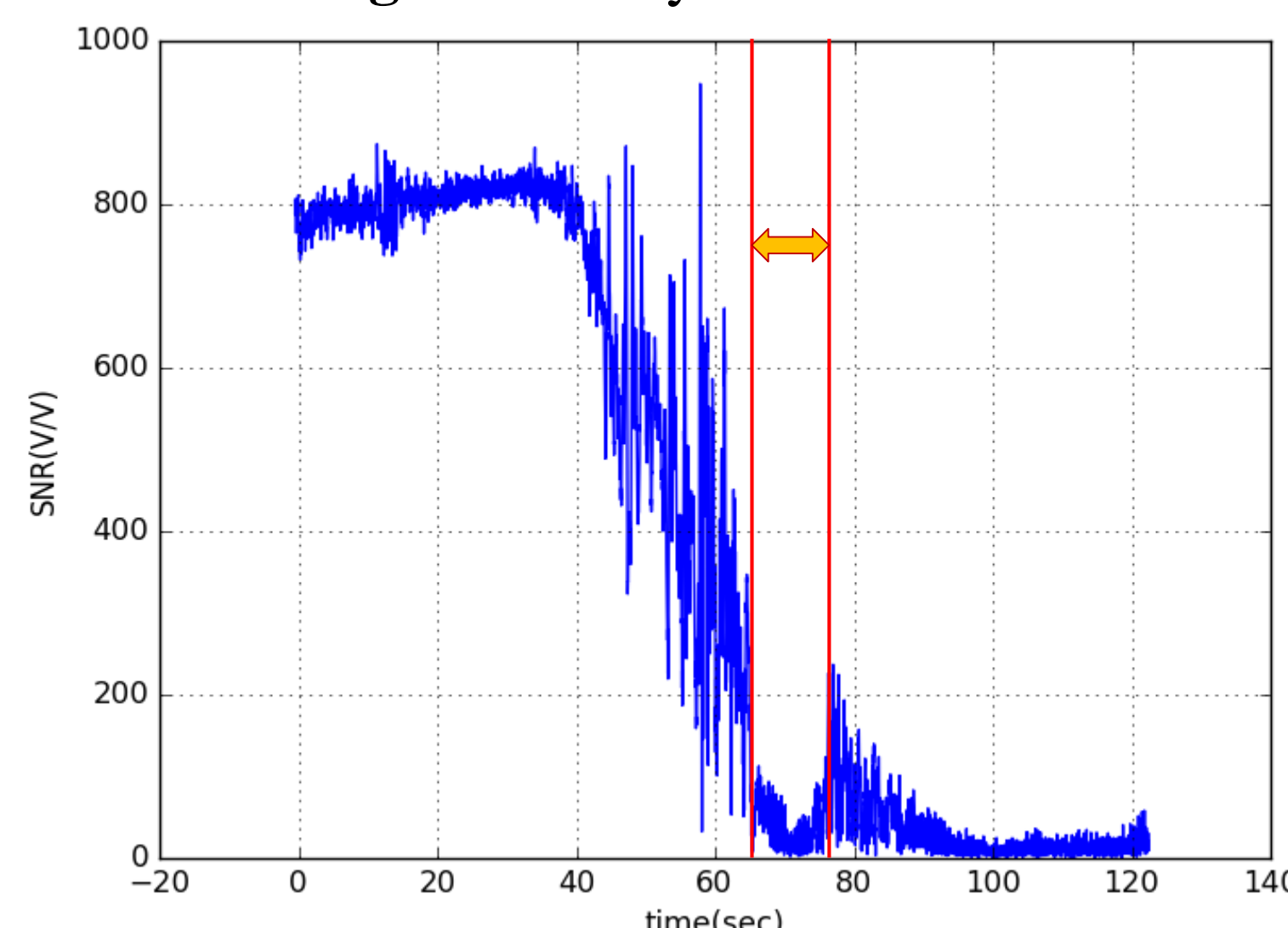
Conclusions

- New retrieval method using optimal estimation constrained by precipitable water measurements effectively decreases the N-bias below ducting layers.
- The new method improves the retrievals by **5%** in average in the 6 test cases using radiosonde profiles with the actual and simulated RO and PW data.
- Future plans: investigate ducting layer information provided by signal amplitude to self-correct the refractivity profile without external assistance, and using the PW method (or ECMWF when AMSR-E is not available) for comparison/validation

Poster No. EB-12

Characteristics of space observations of radio and optical emissions associated with TGFs

Author: Shahab Arabshahi (335D)
Walid Majid (335D)

Introduction

Terrestrial Gamma-ray Flashes, or TGFs, are very strong bursts of gamma-rays (multi-MeV) that are routinely produced inside thunderstorms. They are mainly observed by spacecraft and satellites, and are so bright that can cause significant dead-times on satellite detectors, hundreds of kilometers away.
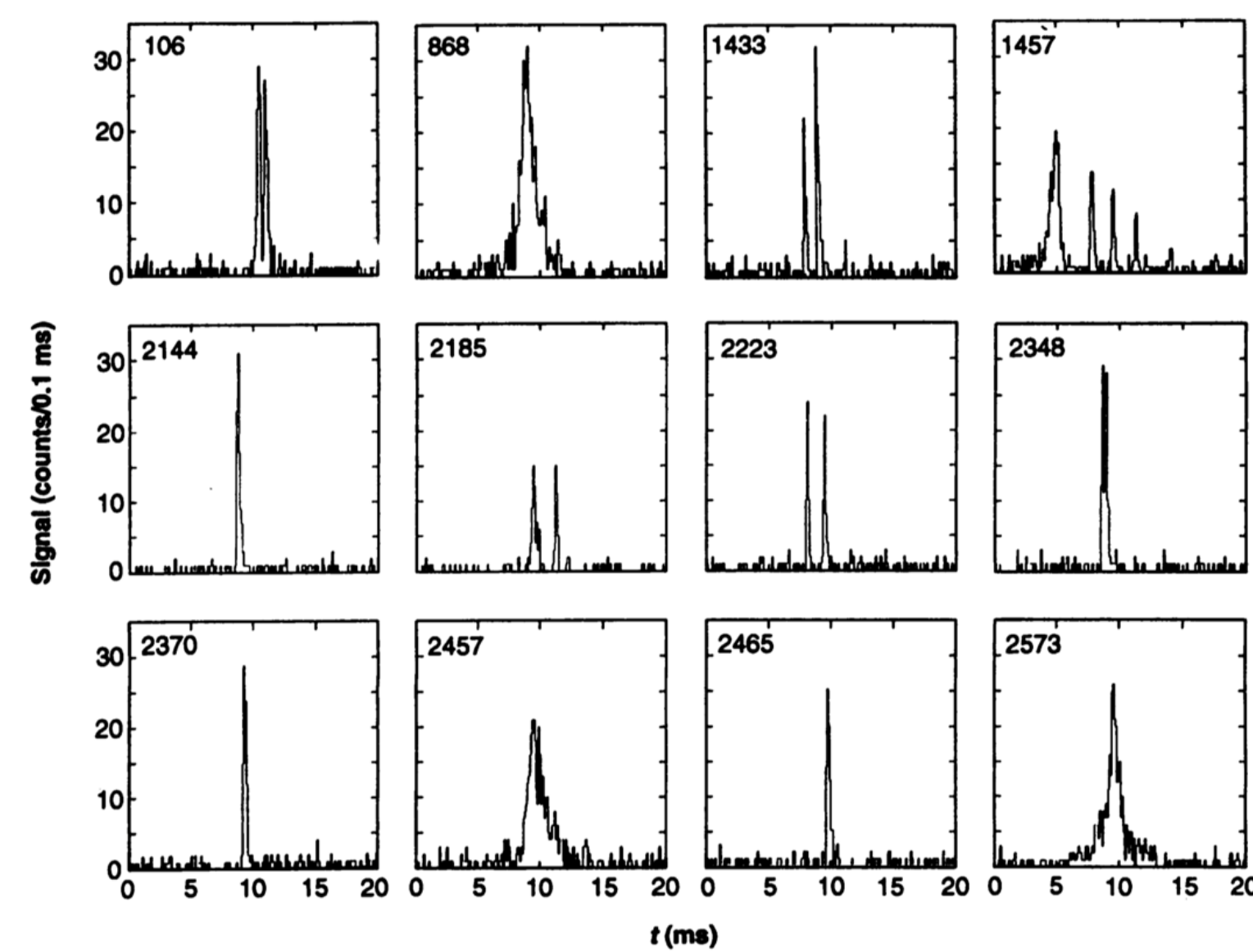

Figure 1 Time profiles of the first twelve events discovered by the Burst and Transient Source Experiment (BATSE) on the Compton Gamma Ray Observatory (CGRO). The time resolution of the plots is 0.1 ms per bin.

Objective

Calculating the radio and optical emissions associated with TGFs and their propagation to Low Earth Orbit (LEO) altitudes. The results would be very beneficial for future planning of space-borne instruments to study TGFs, since they are most suited to be studied using space-borne instruments.

Theory

TGFs are linked to lightning initiation, but the complete details of the source mechanism that produces them and their relations to lightning are still unknown. However, it was suggested, that they are produced by bremsstrahlung scattering of energetic electrons, called "runaway electrons", from air molecules and atoms.

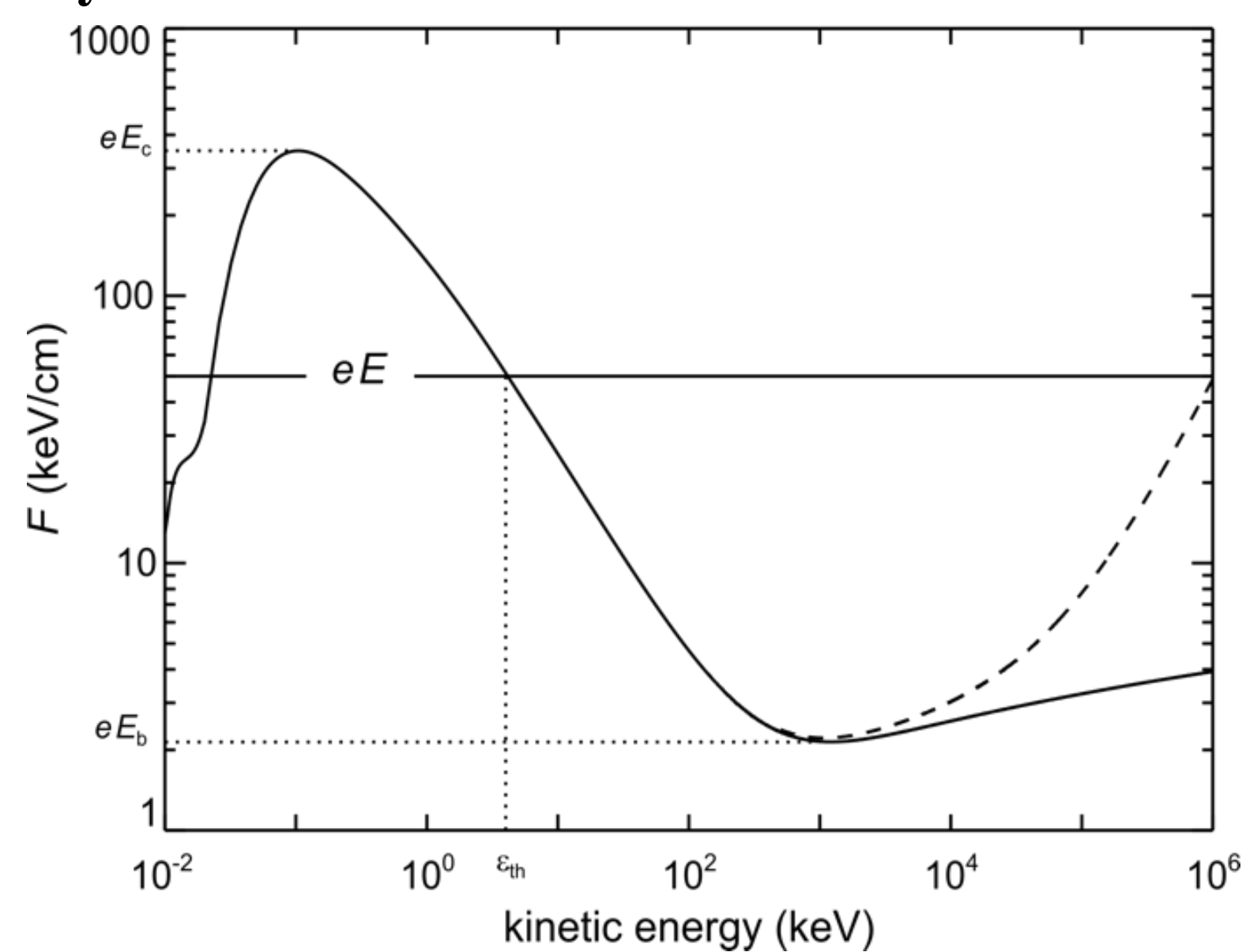### Relativistic Runaway Electron Avalanche:

Figure 2 The effective frictional force and electric force experienced by an energetic electron moving through air at STP as a function of kinetic energy.
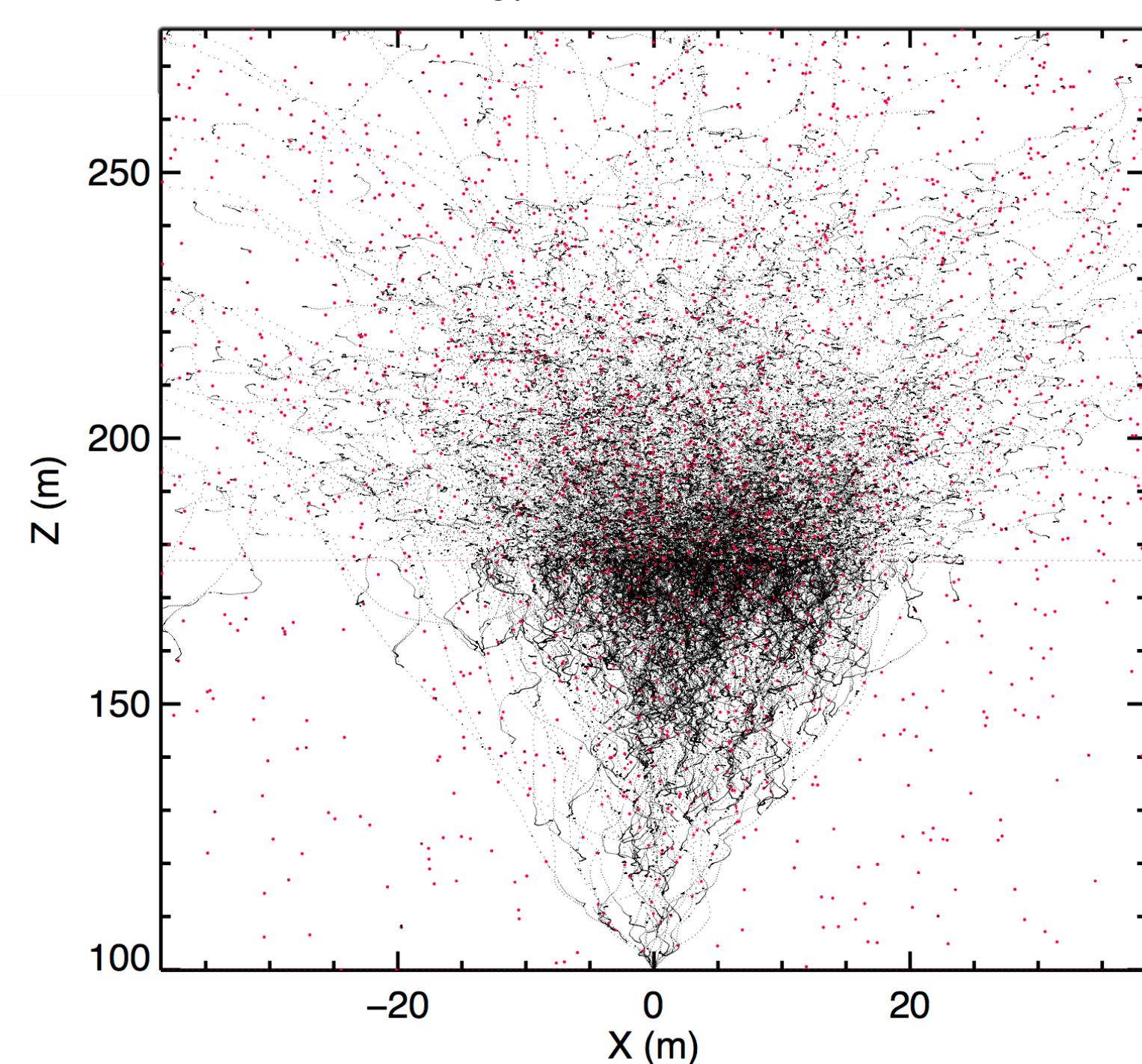

Figure 3 Monte Carlo simulation of Relativistic Runaway Electron Avalanche initiated at 100 m altitude by a mono-energetic beam of 10 seed electrons with 1MeV kinetic energy. The red dotted line shows the end of the avalanche region with includes a uniform electric field at 300kV/m.

Radio Frequency Emissions

Electromagnetic radiation produced by acceleration of runaway and low energy electrons.

$$F_{rad} = 2c^3 \varepsilon_0 \left(\frac{ek \sin\theta}{4\pi\varepsilon_0 c^2 R_0} \right)^2 \left[\frac{\omega^2}{c^2} \right] N_{TGF}^2 \times \exp\left(-\omega^2 \left[\sigma_S^2 + \left(\frac{k^2(1-\beta\cos\theta)^2}{v^2} \right) \right] \right) \left(2\pi \tilde{f}_{TGF}^2 + \frac{1}{N_p} \right) \times \left\{ \left(1 + \right. \right.$$
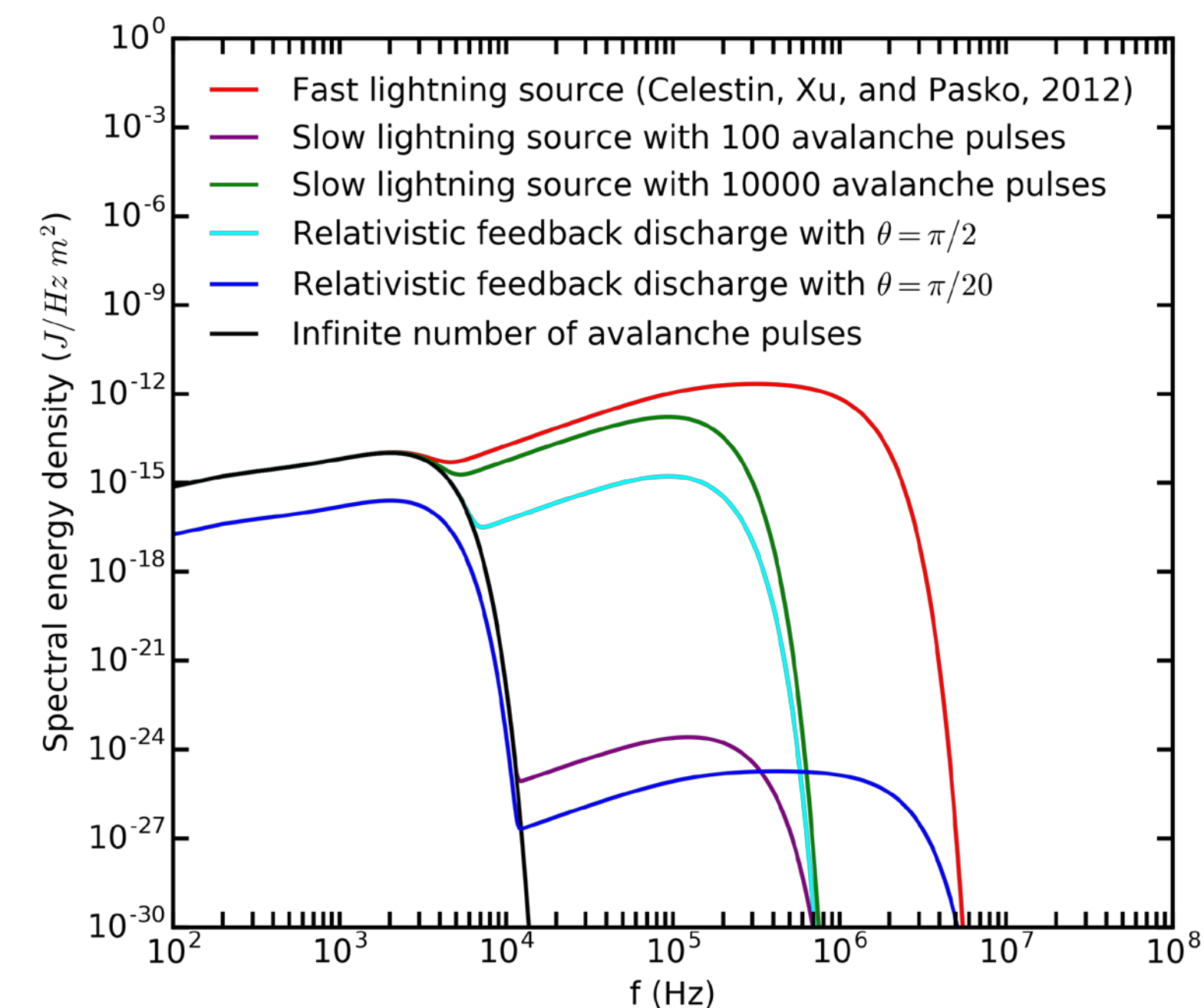

Figure 4 Comparison of RF emission spectral energies produced by different models proposed for the production of TGFs, including the Relativistic Feedback Discharge (RFD) mechanism. Results are shown for observations 400 km away from the end of the avalanche region.
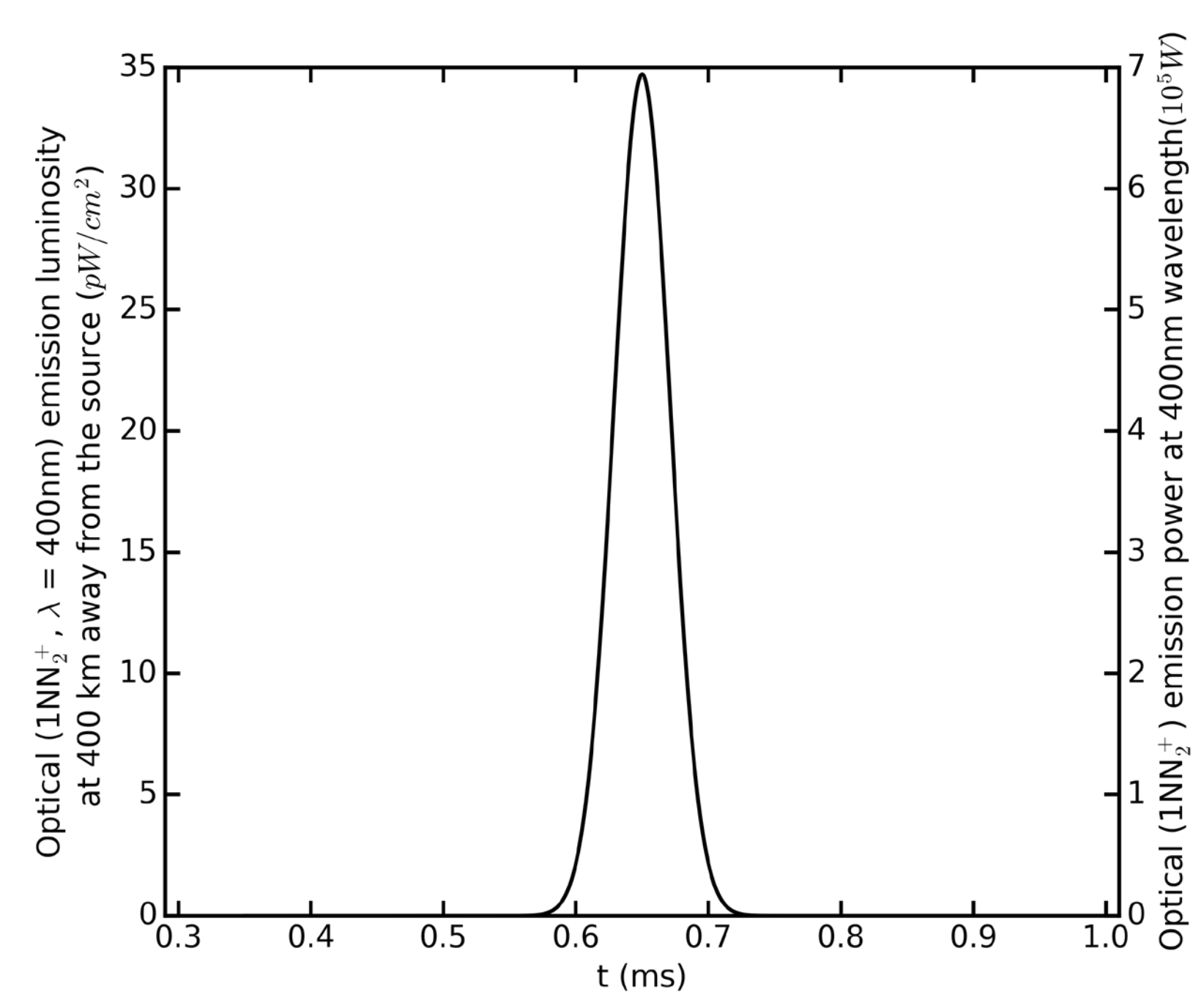

Figure 5 Luminosity of optical emissions produced by the brightest fluorescents band, $1NN_2^+$ band, at 400 km distance from the source.